Pulse generation from mode locked VECSELS AT 1.55 um

Zhuang Zhao

THESE DE DOCTORAT

SPECIALITE: *PHYSIQUE*

Ecole Doctorale " Sciences et Technologies de l'Information des Télécommunications et des Systèmes "

Présentée pour obtenir

LE GRADE DE DOCTEUR EN SCIENCES

DE L'UNIVERSITÉ PARIS-SUD XI

par

Zhuang ZHAO

Pulse generation from Mode-Locked VECSELs at 1.55 µm

Soutenue le 4 octobre 2012, devant la commission d'examen composée de :

M. Alain LE-CORRE	INSA de Rennes UMR 6082	Rapporteur
M. Patrick GEORGES	LCF, Institut d'Optique	Rapporteur
M. Jean-Michel LOURTIOZ	IEF, Université Paris-Sud XI	Examinateur
M. Eric TOURNIE	IES, Université Montpellier 2	Examinateur
M. Stéphane CALVEZ	LAAS-CNRS UMR 8001	Examinateur
Mme Anne C. TROPPER	University of Southampton	Membre invité
Mme Sophie BOUCHOULE	LPN-CNRS UPR 20	Directeur de thèse
M. Jean-Louis OUDAR	LPN-CNRS UPR 20	Codirecteur de thèse

Thèse préparée au Laboratoire de Photonique et de Nanostructures UPR 20

Table of Contents

Chapter 1 INTRODUCTION

An important milestone of optics is the demonstration of the first laser emission in 1960 by T. Maiman at the Hughes Research Laboratory in California [1]. Subsequently, several types of lasers have been developed, such as solid-state, semiconductor, gas and dye lasers. Today, the progress in laser is being driven by the explosion of wide-range applications in communication, industry, medicine, military operations, and scientific research. Each of these applications needs its laser system with suitable properties. For example, optical fiber communication [2], a major application that enables modern Internet, commonly requires lasers with emission wavelengths in the 1.55 μm low-loss band of glass fibers and with single-transverse mode output beams for coupling into single-mode optical fibers.

Lasers generating short pulses have also enabled many applications in science and technology. Numerous laboratory experiments have confirmed that short laser pulses can significantly improve existing applications, for example increase telecommunication data rates [3] and improve computer interconnects [4], or the optical clocking of microprocessors [5-6]. Today, telecommunication systems rely on directly modulated continuous-wave semiconductor lasers. With the combination of wavelength division multiplexing (WDM) technology, transmission rates of more than 1Tbit/s have been demonstrated. Ultrafast lasers can be used as pulse sources in the telecommunication system, rather than shaping the pulses by modulator. The short pulse durations, high peak power, wide spectral bandwidth and low timing jitter translate into simplified synchronization and improved receiver sensitivity [7-8]. Optical analog-to-digital conversion is another application of short optical pulses. Short pulses perform the sampling of an optical signal in a non-linear medium to avoid requiring a very fast photodetector [9]. Another type of sampling that requires short pulses is pump-probe measurements where a medium's response to an optical excitation is probed by another pulse.

In this thesis, we discuss an approach for generating short pulses from a passively mode-locked optically-pumped vertical external-cavity surface-emitting laser (VECSEL). This chapter firstly describes the configuration of optically-pumped VECSELs and their key advantageous properties, such as power scaling, beam quality, and wavelength versatility. Through an overview of the approaches to generate short pulses in telecommunication window (1.3μm-1.55μm), the motivation for this thesis is established. Finally, the structure of the thesis is outlined.

1.1 WHAT IS AN OP-VECSEL

An OP-VECSEL is a type of laser which may be considered as a hybrid system between semiconductor laser and solid state laser. It allows to combine the respective advantages of both laser families: high power operation with a good beam quality, and wavelength versatility. Fig. 1.1 shows the basic configuration of an OP-VECSEL presented by M. Kuznetsov in his book [10]. The laser cavity consists of the back mirror of a semiconductor chip and an external spherical mirror, which defines the laser transverse mode and also serves as the output coupler. The semiconductor chip, which contains a multilayer high-reflectivity mirror, the active region, and an additional top phase layer, is mounted on a heatsink and is excited by an incident pump beam.

Looking at the configuration sketched in Fig. 1.1, an OP-VECSEL can be thought of as a solid state laser, where the semiconductor gain medium replaces the traditional active ions in a transparent host material. Thus the most important benefit of VECSEL is its wavelength versatility in contrast to other solid state lasers. Compound semiconductor materials indeed have different bandgap energies, and thus different photon emission wavelengths for different material compositions.

2
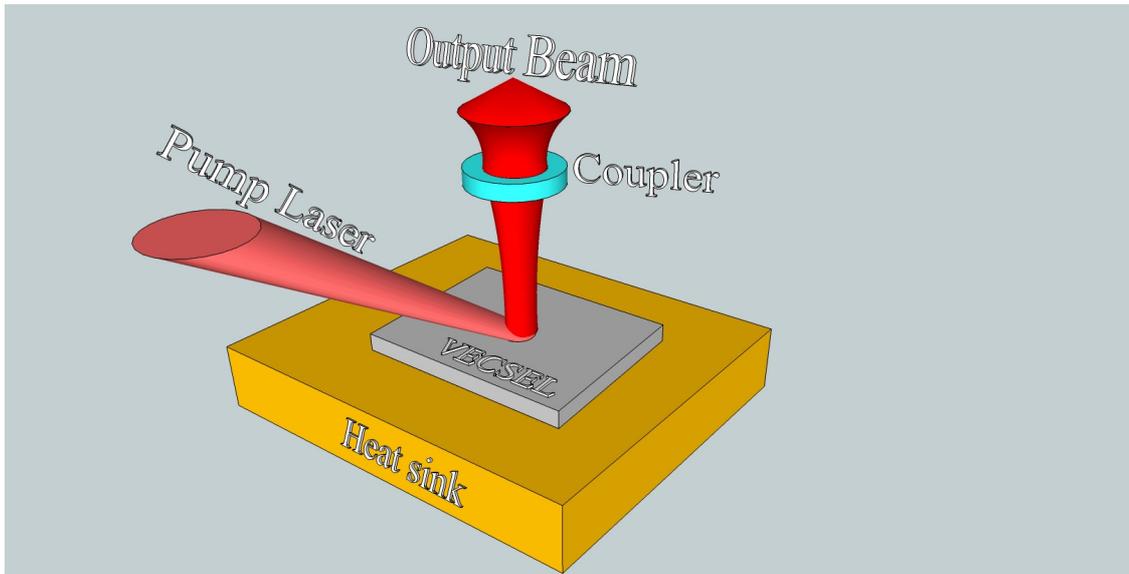
Figure 1.1 Optically pumped semiconductor vertical-external-cavity surface-emitting laser (OP-VECSEL).

Fine bandgap engineering is moreover possible from quantum wells (QWs) photon-emitting layers (by controlling the QW thickness or QW strain, …), which also allows for controlling the emission wavelength. The expitaxial growth of ternary, quaternary, and even quinary semiconductor alloys has been developed by Molecular beam epitaxy (MBE) or Metalorganic vapour phase epitaxy (MOVPE). Direct bandgap semiconductor materials offer today a wide range of emission wavelength, which extend from ~400 nm to ~2.5 µm [11], as shown in Fig. 1.2. Direct bandgap semiconductor material systems are generally formed from elements of the groups Ⅲ and Ⅴ of the periodic table and cover the near infrared wavelength range (NIR) from 800 nm up to 1.65 µm. Starting from a GaAs substrate the short wavelength range of the NIR spectrum can be covered by using different GaAs based semiconductor components: AlGaAs (800 to 870 nm)[12], InGaAs (870 to about 1150 nm)[13-16], GaInNAs (1.1 to 1.3 µm, with some demonstration up to 1.5 µm) [17]. InP-based material system using quaternary alloys (InGaAsP, InGaAlAs) allows the lasers to access the 1300–1650 nm optical fiber communication wavelength region [18-20]. More recently, surface emitting semiconductor lasers emitting in the UV (~ 400 nm) using GaN-based material [21], and

in the mid-infrared (~2.5 μm) using GaInAsSb-based materials have been demonstrated [22]. Furthermore, group IV–VI semiconductor PbTe/PbEuTe and PbSe/PbEuTe-based material systems have been used in the recent years to demonstrate VECSELs in the 4.5–5 μm wavelength range [23-24].
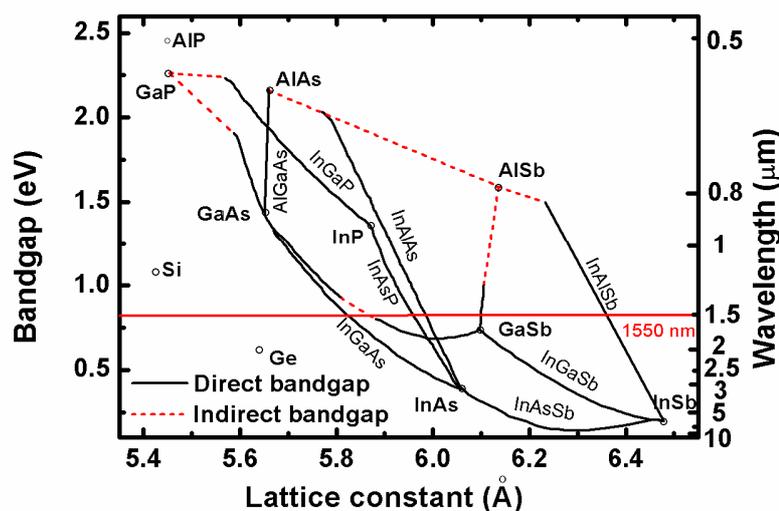
Figure 1.2 Bandgap energy as a function of lattice constant for different III-V semiconductor alloys at room temperature. The solid lines indicate a direct bandgap, whereas the dashed lines indicate an indirect bandgap (Si and Ge are also added to the figure).

Having a look at the state of the art of semiconductor lasers, it appears that obtaining simultaneously high output power (beyond hundred(s) of milliwats) and good beam quality (single transverse mode, nearly circular symmetric beam) is quite difficult. Since the output power of semiconductor lasers is typically limited by heat dissipation, and by optical intensity induced damage, power scaling with semiconductor lasers requires increasing the beam diameter in order to distribute the heat and the optical power over large area. Edge emitting lasers confine the light to the plane of the semiconductor chip with a waveguide and emit light from the edge of the chip. Single-transverse mode operation requires that the waveguide dimension is not larger than one by several microns depending on the emission wavelength. This configuration results in an asymmetric laser beam with strong angular divergence, while the output power is limited by the small

dimension. If the waveguide is enlarged up to tens to hundreds of micrometers, the laser can emit tens of watts of output power, but the waveguide is then highly multimode, and the output beam is significantly elongated with a large aspect ratio, ~100:1 [25-26]. While the edge emitting laser cannot easily provide watt-level output power with circular output beam, in contrast, vertical-cavity surface-emitting laser (VCSEL) with circular cross section, keep the output beam symmetrical and with a smaller divergence. Monolithic VCSEL (forming a short plane-plane optical cavity) can emit near circular single transverse mode beam with output powers up to several milliwatts, and with beam waist of several microns [10, 27-28]. To scale up the output power, a larger active region is required, but the laser beam quickly becomes multimode for output diameters greater than ~ 10 μm. In order to maintain a good beam quality with single transverse mode operation, a strong transverse mode control should be provided by the optical cavity. For this purpose, additional elements have to be added (external to the monolithic semiconductor chip), that will ensure that the size of the stable fundamental transverse mode of the optical resonator correctly matches the size of the gain region. Thus, the vertical-external-cavity surface-emitting laser (VECSEL) was invented: an external spherical mirror was used to stabilize the transverse mode of surface-emitting laser [10].

For typical VECSEL beam diameter beyond tens of microns, injecting carriers uniformly across such a wide gain area is difficult in the traditional diode current injection scheme [27]. The highly-doped semiconductor spreading layer, generally added in the diode structure in order to favor homogeneous injection, will degrade laser threshold and laser efficiency because of significant free carrier absorption. In contrast, optical pumping can allow for injecting and exciting carriers uniformly across a wide area without using doped regions leading to intra-cavity loss. Moreover, compact, low-cost, multimode, high-power semiconductor diode lasers have been developed at many wavelengths and are now commercially available to be used as optical pump.

In short, optically-pumped VECSELs can convert the high pump power of fairly low-cost, low-beam-quality, compact laser diode bars, with a good efficiency, into a near-

diffraction-limited output beam with in wavelength regions which are not covered by established solid-state laser gain materials. The first OP-VECSEL, consisting of strain-compensated InGaAs-GaAsP-GaAs multi quantum-well (MQW), and operating continuous-wave (CW) near 1004 nm with output 0.52 W in a TEM00 mode, was reported by M. Kuznetsov *et al.* in 1997 [29]. After this pioneering work, OP-VECSELs have been demonstrated with output power ranging from 20 mW to 20 W in a fundamental transverse mode, which is substantially higher than from any other type of semiconductor laser. Moreover, additional elements can be inserted in the external intra-cavity such as non-linear optical elements to realize special functions. In particular, the combination of the high intra-cavity power with non-linear elements allows for realizing optical functions such as frequency conversion [30], or passive mode-locking for ultra-short pulse generation [31].

For passive mode-locking, a fast saturable absorber has to be inserted in the cavity. The main breakthrough in the field was the invention of the semiconductor saturable absorber mirror (SESAM) by U. Keller when she was at Bell lab in 1992 [32]. SESAM is a very important part of passively mode-locked VECSEL, and will be further described in chapter 3. The first mode-locked VECSEL was demonstrated in the 0.8-1 μm range, from a GaAs-based gain chip, and a GaAs-based SESAM. Today, the performance of such pulse sources in terms of peak power, pulse duration and spectral bandwidth, open the route towards application such as frequency comb generation for metrology applications [33] and bio-imaging with the mode-locked VECSEL replacing the bulk and costly Titanium:Sapphire laser [34].

Following the very good performances obtained from GaAs-based VECSELs, the mode-locked VECSEL concept has been extended to other material systems and other wavelengths. The PHOTEL group was involved in the development of optical short-pulse source around 1.55 μm, and an overview of the state of the art is given in the next section.

1.2 SHORT PULSE GENERATION FROM MODE-LOCKED OP-VECSELS

Laser sources emitting short pulses are now widely employed in many scientific applications such as waveform measurement, time-resolved spectroscopy, frequency combs, optical interconnection and ultra-high capacity telecommunication systems.

Telecom transmission systems at 40 GHz, 80 GHz and beyond, have been the main driving force for the development of short pulse sources at 1.55 μm in the past years. As an example for optical time-division multiplexing (OTDM) system, the key requirement for the pulse source inside the transmitter is to generate sufficiently short pulses, so they can be interleaved with little overlap. From the view of modulation formats, short pulses are referred to as return-to-zero (RZ) formats. Compared to non-return-to-zero (NRZ) modulation format, the RZ format was introduced because it was found to be more tolerant to dispersion and nonlinearities in fiber and was therefore advantageous for high speed and long range systems [35]. When optical pulses are used to transmit information in a telecommunication system, the strain of optical data is formed by the concatenation of a number of optical pulses, each pulse representing one data bit. Data transmission in RZ format at bit rate exceeding 100 Gbit/s can be performed, if short pulses (<1 ps for 100 Gbit/s) can be generated from the transmitter.

Another application of short pulse optical source at 1.55 μm is optical sampling and optical gating. Optical clocks are required for time de-multiplexing of OTDM signal in the optical domain, or for analog-to-digital conversion in the optical domain.

Fast optical gates are also required to analyze high-bit-rate optical signals. Conventional measurement systems detect the optical signal with a photodetector and measure the temporal variation of the detected photocurrent using an oscilloscope. The temporal response time of the photodetector and the bandwidth of the oscilloscope limit the pulse width that can be measured using this technique. Using an electrical sampling oscilloscope and the fastest photodetectors available today, the overall bandwidth of such measurement system is about 65-70 GHz [36-37]. This bandwidth allows for measuring optical data signals with optical pulses down to a pulse width of few ps. The

characterization bottleneck appears when shorter pulses are used in a transmission system at higher bit rate. Optical sampling is a promising approach to overcome this limit by moving the actual sampling process from the electrical to the optical domain. In an optical sampling system, the optical signal is sampled in the optical domain by an optical sampling gate and afterwards the resulting samples are converted to an electrical signal and detected. One main advantages brought by optics is to avoid the need for very high bandwidth electronics. Moreover, the optical bandwidth of the measurement instrument is only limited by the optical sampling gate used.

Several options are possible for the generation of short pulses in the telecom window (1.3 μm-1.55 μm). They show different advantages in terms of pulse energy, timing jitter, repetition rate, and tunability of the repetition rate. To date, multi-gigahertz pulse sources have involved an edge-emitting semiconductor laser, which is usually either actively or hybridly mode-locked. Typically, the same epitaxial layer forms both the gain (with a forward-biased section) and the saturable absorber (with a reverse-biased section) in ultrafast edge-emitting semiconductor lasers. Such mode-locked edge emitting lasers are attractive because they are compact and potentially integratable with other photonic devices on a single chip. The first monolithic mode-locked edge emitting laser used quantum wells in the active region. Very stable pulse trains at 40 GHz to 80 GHz repetition frequency, and the pulse width of 1 ps to 2 ps have been demonstrated, for example by HHI (Germany) from MQW multi-section edge emitting lasers [38]. More recently, it has been shown that quantum dots (QD) are promising candidates for the fabrication of self-pulsing and mode-locked edge emitting lasers at 1.55 µm. As an example, the PHOTEL group at LPN demonstrated pulse generation at this wavelength from a two sections laser at a very high repetition frequency (346 GHz), based on passive mode-locking mechanism [39]. Unfortunately, it appears difficult to achieve high average power from such lasers, while keeping good passive mode-locking performances. The typical average output power from mode-locked QD edge emitting lasers at 1.55µm is in the µW range. In addition, owing to the geometry of such edge emitting lasers, the profile

of the emitted beam is strongly asymmetric, as discussed earlier. It is also quite challenging to fabricate a monolithic edge-emitting laser with a very precise pulse repetition rate, because a very precise control of cavity length is difficult.

Diode-pumped fiber pulse lasers have been developed and offer excellent performance. Actively mode-locked erbium doped fiber lasers with long, dispersion-compensated cavity have produced harmonically mode-locked pulses used in 1.28 Tbit/s ODTM systems [40]. However, multi-gigahertz fiber lasers require sophisticated means to obtain stable harmonic mode-locking because they have many pulses in the long fiber cavity. Additionally, individual pulses generated by harmonic mode-locking do not necessarily exhibit a fixed phase relation. This excludes promising and important modulation formats such as return-to-zero differential phase shift keying [41-42].

Two other interesting kinds of pulse lasers are based on passive mode-locking mechanism: passively mode-locked solid state laser and passively mode-locked VECSEL. Passive mode-locking means that the pulses are generated without using any expensive multi-gigahertz electronics. In addition, in contrast to fiber-based laser mentioned above, the pulses may originate from fundamental mode-locking even at multi-GHz rate. Thus, every output pulse is a copy of the same single pulse, which travels back and forth in the cavity. Therefore, pulse-to-pulse variations are minimized and the phase of the pulses is constant. As for the repetition frequency tunability, the external cavity laser allows for tuning the repetition rate of pulses mechanically by adjusting the cavity length. Monolithic lasers and fiber based laser have a more limited tuning range because the change in cavity length is induced by a change of refractive index. In the telecom wavelength ranges, where only a few solid-state gain media are available, it was not initially possible to demonstrate multi-GHz pulse repetition rates. However with improved SESAM designs, full C-band tuning [43] and pulse repetition rates up to 100 GHz [44] have been demonstrated with a diode-pumped laser built on Er:Yb:glass crystal. At 1.3 μm, both Nd:YLF [45] and Nd:YVO4 [46] have been passively mode-locked at GHz repetition rates. Passively mode-locked OP-VECSEL have a number of

compelling advantages compared to ultrafast solid state laser: the lasing wavelength can be engineered over a broad range by choosing the right material composition. Since VECSELs are semiconductor lasers, the integration of a semiconductor saturable absorber with the gain structure in a single chip to develop more compact cavity design is in principle possible. Indeed, such a monolithic gain-absorber chip called MIXSEL, has been demonstrated in the GaAs material system by the group of U. Keller at ETH-Zürich [47]. Optical pumping was used in the first experiment, but electrical pumping is compatible with the MIXSEL concept.

The first passively mode-locked OP-VECSEL was demonstrated in 2000 [48], by S. Hoogland et al. in Anne Tropper's group at University of Southampton. They obtained 21.6 mW average output power and 22-ps pulses with a repetition rate of 4 GHz. The VECSEL was grown on GaAs and emitted at 1030 nm. In the following years, large progress in output power and pulse duration has been made. To date, ultrafast VECSELs have been successfully reported with average output powers of up to 6.4 W [49], pulse repetition rates of up to 50 GHz [50] and pulse durations down to 60 fs [51]. All these lasers had diffraction-limited, circular output beams. Repetition rate tuning from 1 GHz to 26 GHz has also been demonstrated [52]. Most of these results have been obtained in the 1 μm spectral region, with a GaAs-based material. Progress towards ultrashort pulse generation at longer wavelength (up to the 1.55 μm window) was more difficult because of the lack of fast SESAMs at this wavelength, and also because of the low power performance of the gain chip mainly due to the bad thermal behaviors of quaternary InP-based semiconductor compounds. The first report on 1.55 μm mode-locked VECSEL was published by H. Lindberg in 2005, the temperature of operation was lower than -20 °C [53].

1.3 CONTENTS

When this PhD work started in November 2009, a first mode-locked VECSEL at 1.55μm had been demonstrated at LPN, generating ~ 2 ps pulses at a repetition frequency of 2 GHz [54].

Starting from this achievement, the main objective of the present PhD work was to optimize the mode-locked VECSEL for shorter (<1 ps) pulse generation, which requires efficient heat dissipation in the OP-VECSEL on one hand, and a fast SESAM on the other hand.

In the first part of this thesis, I will focus on the thermal management of the VECSEL chip including design, fabrication and characterization. A downward heat dissipation approach was employed in this thesis to avoid unwanted etalon effect of intracavity heatspreader. CoMsoL simulations have been carried out to investigate the downward heat dissipation scheme, and to estimate the temperature rise in the active region as a function of pump power. It is concluded that the thermal impedance of the bottom mirror and substrate are of paramount importance in the downward heat sinking approach. A hybrid metal-Bragg GaAs/AlAs mirror has been chosen as the bottom reflector in the VECSEL chip. In order to integrate such a mirror with the InP-based semiconductor active region emitting at 1.55 μm, both the metamorphic growth and the wafer fusion approaches have been used. Chemical Vapour Deposition (CVD)-diamond substrate has the best thermal performance due to its thermal conductivity up to 2000 W/(K*m) and was firstly selected as a bottom substrate in our devices. However CVD diamond substrate is costly and is not easily processed (dicing or thinning is difficult), which presents some limitations for future electrically-pumped version of VECSEL chips or for chip packaging. An alternative cost-effective and more flexible solution for the device substrate has therefore been investigated. VECSELs based on metallic host substrates have been fabricated, and the thermal performances of VECSELs with different substrates have been compared experimentally. We have demonstrated that copper electro-plating may be a good solution to replace CVD-diamond substrate for the

fabrication of 1.55 µm VECSELs. In order to maximize the output power and to enhance the laser external efficiency, the external cavity design has been optimized, mainly by a good matching between the pump spot and the cavity mode, and by an adequate selection of the output coupler mirror.

The second part of this thesis is focused on dispersion control in the SESAM with the goal of achieving sub-picosecond short pulses in passive mode-locking regime. The SESAM structure is based on GaAs and comprises InGaAsNSb QWs surrounded by GaAsN planes for fast absorption recovery time [55]. In order to tune the dispersion of the SESAM microcavity, we have grown specific SESAM structures with top phase layers of GaAs and $Al_{0.7}Ga_{0.3}As$ grown alternatively on top of the absorbing region. The phase layers could be etched selectively, so that the group delay dispersion (GDD) introduced by the SESAM could be tuned step by step. The influence of the overall intracavity GDD on the mode-locked pulse width has been experimentally explored in this way. Using a pump-probe setup, we were able to perform a systematic analysis of the nonlinear reflectivity and carrier recovery time of the different fabricated SESAMs. The first proof-of-principle experiment showed that the concept of GDD management is working, and that the pulse width can be reduced from several picoseconds to less than 1 ps when the resonance and GDD of the SESAM microcavity is correctly adapted.

The thesis is organized as follows: in this introduction chapter 1, passively mode-locked OP-VCSEL device development has been motivated and an overview of different short pulses sources and applications has been presented. Chapter 2 focuses on the design, fabrication and characterization of optically-pumped VECSELs, with a particular emphasis on the thermal management. Chapter 3 discusses our development of dispersion managed SESAMs for mode-locking. In Chapter 4, we present the mode-locking experiments with the thermally-optimized VECSEL chip assembled with the different dispersion-managed SESAMs. Finally, Chapter 5 contains the conclusions and a brief outlook.

1.4 REFERENCE

[1] T. H. Maiman, "Stimulated Optical Radiation in Ruby, " Nature, vol. 187, pp. 493-494,1960.

[2] G.P. Agarwal, Fiber-Optic Communication Systems, 3rd edn, Wiley–Interscience, 2002.

[3] L. F. Mollenauer, P. V. Mamyshev, J. Gripp, M. J. Neubelt, N. Mamysheva, L. Grüner-Nielsen, and T. Veng, "Demonstration of massive wavelength-division multiplexing over transoceanic distances by use of dispersion-managed solitons," Opt. Lett., vol. 25,pp. 704-706, 2000.

[4] D. A. B. Miller, "Rationale and challenges for optical interconnects to electronic chips," Proceedings of the IEEE, vol. 88, pp. 728-749, 2000.

[5] E. Cassan, D. Marris, M. Rouviere, L. Vivien, and S. Laval, "Comparison between electrical and optical global clock distributions for CMOS integrated circuits," Opt. Engin., vol. 44, pp.105402-10, 2005.

[6] A. V. Mule, E. N. Glytsis, T. K. Gaylord, and J. D. Meindl, "Electrical and optical clock distribution networks for gigascale microprocessors," Very Large Scale Integration (VLSI) Systems, IEEE Transactions, vol. 10, pp. 582-594, 2002.

[7] Sang-Gyu Park, A.H. Gnauck, J.M. Wiesenfeld, and L.D. Garrett. "40-Gb/s transmission over multiple 120-km spans of conventional singlemode fiber using highly dispersed pulses," IEEE Photon. Tech. Lett., vol.12, pp. 1085–1087, 2000.

[8] G. A. Keeler, B. E. Nelson, D. Agarwal, C. Debaes, N. C. Helman, A. Bhatnagar, and D. A. B. Miller, "The benefits of ultrashort optical pulses in optically interconnected systems," IEEE J. Sel. Top. Quantum. Electron. , vol. 9, pp. 477-485, 2003.

[9] P. W. Juodawlkis, J. C. Twichell, G. E. Betts, J. J. Hargreaves, R. D. Younger, J. L. Wasserman, F. J. O'Donnell, K. G. Ray, and R. C. Williamson, "Optically sampled analog-to-digital converters," IEEE Trans. Micro. Theo. Tech., vol. 49, pp.1840–1853, 2001.

[10] M. Kuznetsov, VECSEL Semiconductor Lasers: A Path to High-Power, Quality Beam, and UV to IR Wavelength by Design, Wiley-VCH, 2010.

[11] U. Keller and A. C. Tropper, "Passively modelocked surface-emitting semiconductor lasers," Physics Reports, vol. 429, pp. 67-120, 2006.

[12] J. E. Hastie, J. M. Hopkins, S. Calvez, C. W. Jeon, D. Burns, R. Abram, E. Riis, A. I. Ferguson, and M. D. Dawson, "0.5-W single transverse-mode operation of an 850-nm diode- pumped surface-emitting semiconductor laser," IEEE Photon. Technol. Lett., vol. 15, pp. 894-896, 2003.

[13] R. Häring, R. Paschotta, A. Aschwanden, E. Gini, F. Morier-Genoud, and U. Keller, "Highpower passively mode-locked semiconductor lasers," IEEE J. Quant. Electr., vol. 38, pp. 1268- 1275, 2002.

[14] A. Garnache, S. Hoogland, A. C. Tropper, I. Sagnes, G. Saint-Girons, and J. S. Roberts, "Sub- 500-fs soliton-like pulse in a passively mode-locked broadband surface-emitting laser with 100 mW average power," Appl. Phys. Lett., vol. 80, pp. 3892-3894, 2002.

[15] W. J. Alford, T. D. Raymond, and A. A. Allerman, "High power and good beam quality at 980 nm from a vertical external-cavity surface-emitting laser," J. Opt. Soc. Am. B, vol. 19, pp. 663-666, 2002.

[16] J. E. Hastie, J. M. Hopkins, C. W. Jeon, S. Calvez, D. Burns, M. D. Dawson, R. Abram, E. Riis, A. I. Ferguson, W. J. Alford, T. D. Raymond, and A. A. Allerman, "Microchip vertical external cavity surface emitting lasers," Electron. Lett. , vol. 39, pp. 1324-1326, 2003.

[17] J. M. Hopkins, S. A. Smith, C. W. Jeon, H. D. Sun, D. Burns, S. Calvez, M. D. Dawson, T. Jouhti, and M. Pessa, "0.6 W CW GaInNAs vertical external-cavity surface emitting laser operating at 1.32 μm," Electron. Lett. Vol. 40, pp. 30-31, 2004.

[18] M. El Kurdi, S. Bouchoule, A. Bousseksou, I. Sagnes, A. Plais, M. Strassner, C. Symonds, A. Garnache, and J. Jacquet, "Room temperature continuous-wave laser

operation of an Electrically-Pumped 1.55 μm VECSEL," Electron. Lett., vol. 40, pp. 671-672, 2004.

[19] A. Bousseksou, M. El Kurdi, M. D. Salik, I. Sagnes, and S. Bouchoule, "Wavelength tunable InP-based EP-VECSEL operating at room temperature and in CW at 1.55 μm," Electron. Lett., vol. 40, pp. 1490- 1491, 2004.

[20] H. Lindberg, M. Strassner, E. Gerster, and A. Larsson, "0.8 W optically pumped vertical external cavity surface emitting laser operating CW at 1550 nm," Electron. Lett., vol. 40, pp. 601- 602, 2004.

[21] S. H. Park, J. Kim, H. Jeon, T. Sakong, S. N. Lee, S. Chae, Y. Park, C. H. Jeong, G. Y. Yeom, and Y. H. Cho, "Room-temperature GaN vertical-cavity surface-emitting laser operation in an extended cavity scheme, " Appl. Phys. Lett., vol. 83, pp. 2121–2123, 2003.

[22] A. Ouvrard, A. Garnache, L. Cerutti, F. Genty, and D. Romanini, "10 GHz passively mode-locked external-cavity semiconductor laser with 1.4 W average output power, " IEEE Photon. Technol. Lett., vol. 17, pp.2020–2022, 2005.

[23] M. Rahim, M. Arnold, F. Felder, K. Behfar, and H. Zogg, "Midinfrared lead–chalcogenide vertical external cavity surface emitting laser with 5 μm wavelength." Appl. Phys. Lett.,vol. 91, pp.151102-04, 2007.

[24] M. Rahim, A. Khiar, F. Felder, M. Fill, and H. Zogg, "4.5 μm wavelength vertical external cavity surface emitting laser operating above room temperature." Appl. Phys. Lett., vol.94, pp.201112-14, 2009.

[25] E. Kapon, Semiconductor Lasers II: Materials and Structures, Academic Press.1999.

[26] R. Diehl, High Power Diode Lasers, Springer, 2000.

[27] C. W. Wilmsen, H. Temkin, and L. A. Coldren, Vertical-Cavity Surface-Emitting Lasers: Design, Fabrication, Characterization, and Applications, Cambridge University Press, 1999.

[28] H. Li, and K. Iga, Vertical-Cavity Surface-Emitting Laser Devices, Springer, 2002.

[29] M. Kuznetsov, F. Hakimi, R. Sprague, and A. Mooradian, "High-power (>0.5-W CW) diode-pumped vertical external- cavity surface-emitting semiconductor lasers with circular TEM00 beams. " IEEE Photon. Technol. Lett., vol. 9, pp. 1063–1065, 1997.

[30] M. A. Hadley, G. C. Wilson, K. Y. Lau, and J. S. Smith, "High single transverse-mode output from external cavity surface-emitting laser diodes. " Appl. Phys. Lett., vol. 63, pp. 1607–1609, 1993.

[31] P. J. Delfyett, H. Shi, S. Gee, C. P. J. Barty, G. Alphones, and J. Connolly, "Intracavity spectral shaping in external cavity mode-locked semiconductor diode lasers." IEEE J. Sel. Top. Quantum Electron., vol. 4, pp. 216–223, 1998.

[32] U. Keller, D. A. B. Miller, G. D. Boyd, T. H. Chiu, J. F. Ferguson, and M. T. Asom, "Solid-state low-loss intracavity saturable absorber for Nd:YLF lasers: an antiresonant semiconductor Fabry - Perot saturable absorber, " Opt. Lett., vol. 17, pp. 505-507, 1992.

[33] H. R. Telle, G. Steinmeyer, A. E. Dunlop, J. Stenger, D. H. Sutter, and U. Keller, "Carrier-envelope offset phase control: A novel concept for absolute optical frequency measurement and ultrashort pulse generation, " Appl. Phys. B 69(4), 327–332 (1999).

[34] P. Loza-Alvarez, R. Aviles-Espinosa, D. Artigas-García, C. Hamilton, G. Malcolm, "Multiphoton imaging with compact semiconductor disk lasers," Proc. SPIE 8242, 824223 ,2012.

[35] D. Breuer and K. Petermann., "Comparison of NRZ- and RZ-modulation format for 40-Gb/s TDM standard-fiber systems," IEEE Photon. Technol. Lett., vol. 9, pp.398–400, 1997.

[36] N. Yamada, S. Nogiwa, and H. Ohta, ''Measuring eye diagram of 640 Gbis OTDM signal with optical sampling system by using wavelength tunable soliton pulse,'' in Pro. 29th Eur. Conf on Opt. COmm. (ECOC'03), Rimini (Italy), September 21-25 2003, paper Mo4.6.5.

[37] M. Shirane, Y. Hashimoto, H. Kurita, H. Yamada, and H. Yokoyama, "Optical sampling measurement with all-optical clock recovery using mode-locked diode lasers, " Optical Fiber Commm. Conf.. Technical Digest, Postconference Edition, 2001, p. MG2.

[38] L. Hou, M. Haji, R. Dylewicz, J. Akbar, B. Qiu, and A. C. Bryce, "Low divergence angle and low jitter 40 GHz AlGaInAs/InP 1.55 μm mode-locked lasers," Opt. Lett., vol. 36, pp.966-968, 2011.

[39] K. Merghem, A. Akrout, A. Martinez, F. Lelarge, G.-H. Duan, G. Aubin, A. Ramdane, "Pulse generation at 346 GHz using a passively mode locked quantum-dash-based laser at 1.55 μm," Appl. Phys. Lett. , vol.94, pp.021107-09, 2009.

[40] M. Nakazawa, T. Yamamoto, and K. R. Tamura., "1.28Tbit/s-70km OTDM transmission using third- and fourth-order simultaneous dispersion compensation with a phase modulator," Electron. Lett., vol. 36, pp. 2027–2029, 2000.

[41] J. Leibrich, C. Wree,W. Rosenkranz, "CF-RZ-DPSK for suppression of XPM on dispersion-managed long-haul optical WDM transmission on standard single-mode fiber," IEEE Photon Technol. Lett. Vol.14 ,pp.155- 157,2002.

[42] C. Xu, X. Liu, L.F. Mollenauer, X.Wei, "Comparison of return-to-zero differential phase-shift keying and ON-OFF keying in long-haul dispersion managed transmission," IEEE Photon Technol. Lett., vol. 15, pp.617-619,2003.

[43] G. J. Spühler, P. S. Golding, L. Krainer, I. J. Kilburn, P. A. Crosby, M. Brownell, K. J. Weingarten, R. Paschotta, M. Haiml, R. Grange, and U. Keller, "Multi-wavelength source with 25 GHz channel spacing tunable over C-band," Electron. Lett., vol. 39, pp.778-780, 2003.

[44] A. E. H. Oehler, S. C. Zeller, T. Südmeyer, U. Keller, and K. J. Weingarten, "Moving towards 100 GHz from a passively mode-locked Er:Yb:glass laser at 1.5 μm," Lasers and Electro-Optics and the International Quantum Electronics Conference. 2007.

[45] V. Liverini, S. Schön, R. Grange, M. Haiml, S. C. Zeller, and U. Keller, "Low-loss GaInNAs saturable absorber mode locking a 1.3-μm solid-state laser," Appl. Phys. Lett. , vol.84, pp.4002-4004, 2004.

[46] G. J. Spuhler, G. J. Spuhler, L. Krainer, V. Liverini, R. Grange, M. Haiml, S. Pawlik, B. Schmidt, S. Schon, and U. Keller, "Passively mode-locked 1.3-μm multi-GHz Nd:YVO4 lasers with low timing jitter," IEEE Photon Technol. Lett., vol.17 , pp.1319-1321, 2005.

[47] D. J. H. C. Maas, A. R. Bellancourt, B. Rudin, M. Golling, H. J. Unold, T. Südmeyer, and U.Keller, "Vertical integration of ultrafast semiconductor lasers," Appl. Phys. B, vol. 88, pp. 493-497, 2007.

[48] S. Hoogland, S. Dhanjal, A. C. Tropper, J. S. Roberts, R. Haring, R. Paschotta, F. Morier- Genoud, and U. Keller, "Passively mode-locked diode-pumped surface-emitting semiconductor laser," IEEE Photon. Technol. Lett., vol. 12, pp. 1135-1137, 2000.

[49] B. Rudin, V. J. Wittwer, D. J. H. C. Maas, M. Hoffmann, O. D. Sieber, Y. Barbarin, M. Golling, T. Südmeyer, and U. Keller "High-power MIXSEL: an integrated ultrafast semiconductor laser with 6.4 W average power," Opt. Express, vol. 18, pp. 27582 ,2010.

[50] D. Lorenser, D. J. H. C. Maas, H. J. Unold, A.-R. Bellancourt, B. Rudin, E. Gini, D. Ebling, and U. Keller, "50-GHz passively mode-locked surface-emitting semiconductor laser with 100 mW average output power," IEEE J. Quantum Electron. Vol. 42, pp. 838 ,2006.

[51] A. H. Quarterman, K. G. Wilcox, V. Apostolopoulos, Z. Mihoubi, S. P.Elsmere, I. Farrer, D. A. Ritchie, and A. C. Tropper, "A passively mode-locked external-cavity semiconductor laser emitting 60-fs pulses," Nat. Photonics, vol. 3, pp.729-732, 2009.

[52] O. D. Sieber, V. J. Wittwer, M. Mangold, M. Hoffmann, M. Golling, T. Südmeyer, U. Keller "Femtosecond VECSEL with tunable multi-Gigahertz repetition rate," Opt. Expre., vol. 19, pp. 23538-23543, 2011.

[53] H. Lindberg, M. Sadeghi, M. Westlund, S. Wang, A. Larsson, M. Strassner, and S. Marcinkevicius, "Mode locking a 1550 nm semiconductor disk laser by using a GaInNAs saturable absorber," Opt. Lett., vol. 30, pp. 2793-2795, 2005.

[54] A. Khadour, S. Bouchoule, G. Aubin, J. C. Harmand, J. Decobert, and J. L. Oudar, "Ultrashort pulse generation from 1.56 μm mode-locked VECSEL at room temperature," Opt. Express, vol. 18, pp.19902-19909, 2010.

[55] M. Le Dû, J. C. Harmand, O. Mauguin, L. Largeau, L. Travers, and J. L. Oudar, "Quantum-well saturable absorber at 1.55 μm on GaAs substrate with a fast recombination rate," Appl. Phys. Lett., vol. 88, pp. 201110-3, 2006.

Chapter 2 OPTICALLY-PUMPED VECSEL

Optically pumped Vertical-external-cavity surface-emitting lasers (VECSELs) were developed in the mid-1990s [1, 2] to overcome a key problem with conventional semiconductor lasers: how to generate watt-level and higher optical powers with fundamental transverse mode circular optical beam quality. Researchers at ETH have demonstrated an optically pumped VECSEL generating more than 20 W of continuous wave (CW) output power in a fundamental transverse mode with spatial quality parameter M_2 of 1.1 (a single-transverse mode diffraction-limited beam has M_2=1) at 960 nm [3]. Moreover, the external cavity gives tremendous versatility to VECSEL device configurations and functions, allowing for the insertion of intracavity optical elements in order to realize specific functions such as passive mode-locking or frequency doubling.

In section 2.1, we present the VECSEL principle and some optical modeling. In section 2.2, we show the VECSEL structures and we discuss the design of each part. In section 2.3, we present an analytical model and simulation for the temperature elevation, and we discuss the impact of the bottom Distributed Bragg Reflector (DBR) and the host substrate. The VECSEL device fabrication is described in section 2.4. We give an introduction to the different characterization methods in section 2.5. Finally, we show the plane-concave cavity design in section 2.6, and the characterization results of our VECSELs in the cavity are given in section 2.7.

2.1 OPTICAL MODELING

A VECSEL chip is formed by a stack of semiconductor thin layers. The semiconductor chip consists of two sections: a highly reflecting mirror, and the active region. The basic operating principles of VECSEL lasers are illustrated in Fig. 2.1. It shows the conduction and valence band energy levels across the semiconductor layers and explains the functions of the various layers.

The highly-reflecting (HR) mirror incorporates a periodic quarter-wave stack of layers of alternating high and low refractive index. Such a distributed Bragg mirror (DBR) acts as a HR plane cavity mirror. In front of the DBR is the active region, which is typically a few half wavelengths in thickness, and contains quantum wells. When a pump laser is focused on the surface, the semiconductor chip absorbs the pump light and converts it into desired laser light.

The optical wave of the laser mode, back-reflecting from the DBR, sets up a standing wave inside the chip due to the microcavity effect. Quantum wells (QWs) have to be placed near the antinodes of this standing wave in order to provide efficient gain to the laser. Typically, the gain region spreads over several periods of this standing wave.

The properties of a VECSEL are determined both by the design of the semiconductor quantum wells, and by the design of the microcavity in which they are embedded. In this thesis, we use a well known transfer matrix algorithm to analyze the electrical field inside and outside of the multilayer structures. The algorithm resulted in a flexible program used to design, analyze and characterize VECSEL multilayer structures.
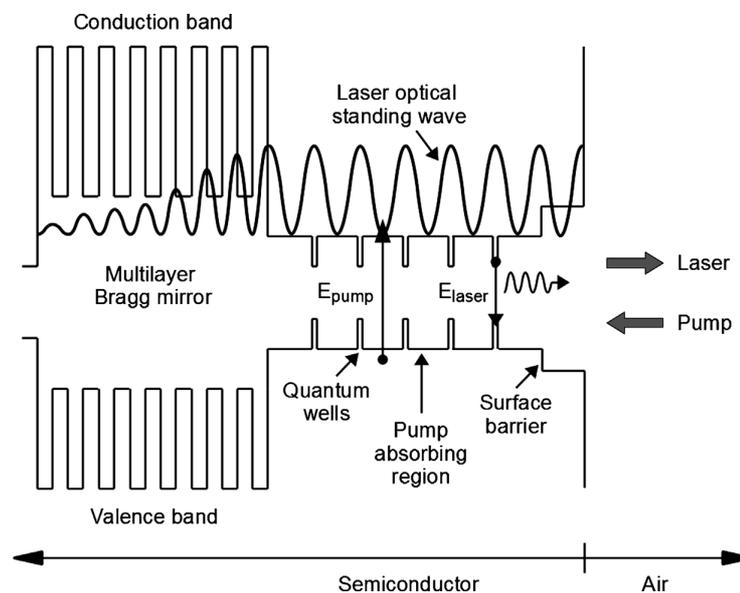
Figure 2.1 operation principle of optically pumped VECSEL[4]

21

2.1.1 Matrix algorithm for dielectric multilayers structures
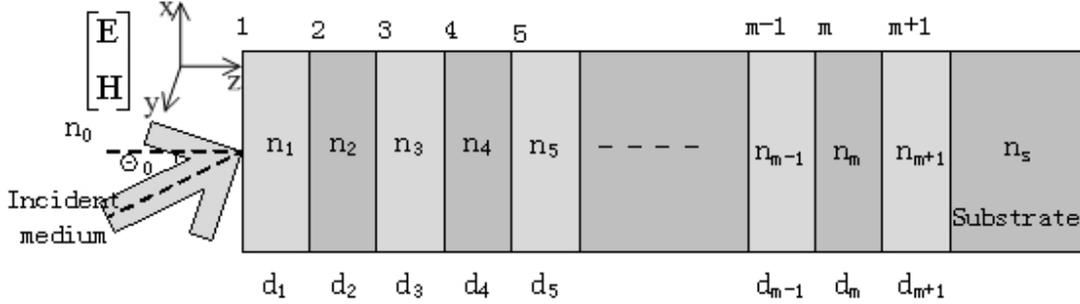
Figure2.2 Configuration of multilayer structure

The multilayer structure (in our case the VECSEL structure) contains N layers with refractive indices n_j and thicknesses d_j. The incident medium on top is air, with refractive index n_0. The bottom layer is the substrate with refractive index n_s and is considered as the emergent medium in the calculation. Let's suppose that the light beam is incident from incident medium to the VECSEL surface with an angle of incidence θ_0. The interface between incident medium and VECSEL is interface 1, and the following interface in the VECSEL chip are 2, 3, 4…m-1, m, m+1,….

If the input light beam is (E, H), according to Maxwell equation, one can get the relation between electric filed and magnetic field:

$$\nabla \times \vec{E} = -\mu \frac{\partial \vec{H}}{\partial t} \tag{2.1}$$

where μ is the permeability of the medium.

When we consider the electromagnetic field wave having angular frequency ω propagating in the z-axis , the electric and magnetic fields can be expressed as

$$E_x(z) = E_x \exp[i(\omega t - \bar{\gamma} z)] \tag{2.2}$$

$$H_x(z) = H_x \exp[i(\omega t - \bar{\gamma} z)] \tag{2.3}$$

where $\bar{\gamma}$ is the complex propagation constant, x denotes the axis in the plane perpendicular to the z-axis. Substituting Equation (2.2) and (2.3) into Equation (2.1), we can get the magnetic field along the z-axis:

$$H_y(z) = \frac{\bar{\gamma}}{\omega\mu} \cdot E_x(z) = \frac{1}{\eta} E_x(z) \tag{2.4}$$

We note $Y = \frac{1}{\eta}$ as the optical admittance of the medium. In a non-magnetic medium, $Y = \bar{N} = n - ik$, where n is the refractive index and k is the extinction coefficient.
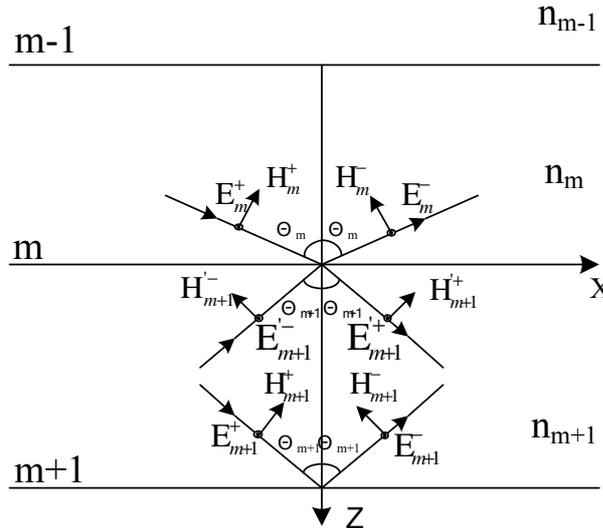
Figure 2.3 TE mode light transfer in VECSEL

Two different linear polarizations of a plane wave incident to the VECSEL surface can be considered. Electric field perpendicular to incident plane is S-polarization (TE mode), and the other one is P-Polarization with magnetic field perpendicular to incident plane (TM mode).

Fig. 2.3 shows the incident, reflected and transmitted electrical field at the (m+1)-th interface between m-th and (m+1)-th layer, for the case of a TE polarized incident plane

23

wave. θ_m and θ_{m+1} are the angles of incidence at the (m+1)-th and (m+2)-th interface respectively. At the (m+1)-th interface we can write the boundary conditions:

$$E_m^+ + E_m^- = E_{m+1}^{'+} + E_{m+1}^{'-}$$ (2.5)

$$(H_m^+ + H_m^-) \cdot \cos\theta_m = (H_m^{'+} + H_m^{'-})\cos\theta_{m+1}$$ (2.6)

Combining Equation (2.4) and Equation (2.6), we obtain:

$$Y_m \cdot \cos\theta_m \cdot (E_m^+ - E_m^-) = Y_{m+1} \cdot \cos\theta_{m+1} \cdot (E_{m+1}^{'+} - E_{m+1}^{'-})$$ (2.7)

Combining Equation (2.5) and Equation (2.7), and writing them into a matrix form, the boundary conditions are expressed as:

$$\begin{bmatrix} 1 & 1 \\ Y_m\cos\theta_m & -Y_m\cos\theta_m \end{bmatrix} \cdot \begin{bmatrix} E_m^+ \\ E_m^- \end{bmatrix} = \begin{bmatrix} 1 & 1 \\ Y_{m+1}\cos\theta_{m+1} & -Y_{m+1}\cos\theta_{m+1} \end{bmatrix} \cdot \begin{bmatrix} E_{m+1}^{'+} \\ E_{m+1}^{'-} \end{bmatrix}$$ (2.8)

Similar to the TE mode, we can express the boundary conditions for the TM mode at the (m+1)-th interface as follows:

$$\begin{bmatrix} \cos\theta_m & \cos\theta_m \\ Y_m & -Y_m \end{bmatrix} \cdot \begin{bmatrix} E_m^+ \\ E_m^- \end{bmatrix} = \begin{bmatrix} \cos\theta_{m+1} & \cos\theta_{m+1} \\ Y_{m+1} & -Y_{m+1} \end{bmatrix} \cdot \begin{bmatrix} E_{m+1}^{'+} \\ E_{m+1}^{'-} \end{bmatrix}$$ (2.9)

The field amplitudes (E_m^+ and E_m^-) on one side at (m+1)-th interface are related to the corresponding field amplitudes on the other-hand ($E_{m+1}^{'+}$ and $E_{m+1}^{'-}$), written as:

$$\begin{bmatrix} E_m^+ \\ E_m^- \end{bmatrix} = V_m^{-1}V_{m+1} \cdot \begin{bmatrix} E_{m+1}^{'+} \\ E_{m+1}^{'-} \end{bmatrix}$$ (2.10)

where V_m is called dynamical matrix [5]. For TE mode and TM mode, V_m is given in different expressions:

$$\text{For TE mode} \quad V_m = \begin{bmatrix} 1 & 1 \\ Y_m\cos\theta_m & -Y_m\cos\theta_m \end{bmatrix}$$ (2.11)

$$\text{For TM mode} \quad V_m = \begin{bmatrix} \cos\theta_m & \cos\theta_m \\ Y_m & -Y_m \end{bmatrix}$$ (2.12)

From Equation (2.5) to (2.10), we get the electric field transform at the interface of two adjacent layers.

The time-independent part of the electrical field introduced in Equation (2.2) can be expressed in the (m+1)-th layer at (m+1)-th interface as:

$$E_{m+1}^{'+} = E_0 \exp(-i \bar{\gamma} z_{m+1}) \tag{2.13}$$

$$E_{m+1}^{'-} = E_0 \exp(i \bar{\gamma} z_{m+1}) \quad , \tag{2.14}$$

while the electric field in the (m+1)-th layer at the (m+2)-th interface is written as:

$$E_{m+1}^{+} = E_0 \exp(-i \bar{\gamma} z_{m+1}) = E_0 \exp[-i \bar{\gamma}(z_{m+1} + d_{m+1})] \tag{2.15}$$

$$E_{m+1}^{-} = E_0 \exp(i \bar{\gamma} z_{m+1}) = E_0 \exp[i \bar{\gamma}(z_{m+1} + d_{m+1})] \quad . \tag{2.16}$$

So we can get the electric field transform in the (m+1) layer:

$$E_{m+1}^{+} = E_{m+1}^{'+} \exp[-i \bar{\gamma} d_{m+1}] \tag{2.17}$$

$$E_{m+1}^{-} = E_{m+1}^{'-} \exp[i \bar{\gamma} d_{m+1}] \tag{2.18}$$

The complex transmission coefficient $\bar{\gamma}$ in the (m+1)-th layer can be written as $\bar{\gamma}_{m+1} = \beta_{m+1} - i\alpha_{m+1}/2$, $\beta_{m+1} = \dfrac{2\pi n_{m+1}}{\lambda}$ is the real propagation constant; $\alpha_{m+1} = \dfrac{4\pi k_{m+1}}{\lambda}$ is the absorption coefficient of (m+1)-th layer material. If $\alpha_{m+1} > 0$, the medium is an absorber, while if $\alpha_{m+1} < 0$ there is gain in the medium, for example in a QW medium. In the following, we assume $\alpha_{m+1} = 0$, and $\bar{\gamma}_{m+1} d_{m+1} = \beta_{m+1} d_{m+1} = \dfrac{2\pi n_{m+1} d_{m+1}}{\lambda \cos\theta_{m+1}} = \phi_{m+1}$. The Equations (2.17) and (2.18) can be expressed as:

$$E_{m+1}^{+} = E_{m+1}^{'+} \exp[-i\phi_{m+1}] \tag{2.19}$$

$$E_{m+1}^{-} = E_{m+1}^{'-} \exp[i\phi_{m+1}] \tag{2.20}$$

where ϕ_{m+1} is the phase change in (m+1)-th layer, λ is the wavelength of incident light, θ_{m+1} is the angle of incidence in the (m+1)-th layer.

We write Equations (2.19) and (2.20) in to a matrix form:

$$\begin{bmatrix} E_{m+1}^{'+} \\ E_{m+1}^{'-} \end{bmatrix} = \begin{bmatrix} \exp(i\phi_{m+1}) & 0 \\ 0 & \exp(-i\phi_{m+1}) \end{bmatrix} \cdot \begin{bmatrix} E_{m+1}^{+} \\ E_{m+1}^{-} \end{bmatrix} \tag{2.21}$$

The phase matrix of (m+1)-th layer is

$$U_{m+1} = \begin{bmatrix} \exp(i\phi_{m+1}) & 0 \\ 0 & \exp(-i\phi_{m+1}) \end{bmatrix} \tag{2.22}$$

Combining Equations (2.10) and (2.22), we can obtain the relation between E_m and E_{m+1},

$$\begin{bmatrix} E_m^{+} \\ E_m^{-} \end{bmatrix} = V_m^{-1} V_{m+1} U_{m+1} \cdot \begin{bmatrix} E_{m+1}^{+} \\ E_{m-1}^{-} \end{bmatrix} \tag{2.23}$$

Combine Equations (2.12) and (2.23), we can finally obtain the relation between the incident light and the emergent light of a stack of (m+2) layers:

$$\begin{bmatrix} E_0^{+} \\ E_0^{-} \end{bmatrix} = V_0^{-1} V_1 U_1 V_1^{-1} V_2 U_2 V_2^{-1} \cdots V_m^{-1} V_{m+1} U_{m+1} V_{m+1}^{-1} V_{m+2} U_{m+2} V_{m+2}^{-1} V_{sub} \begin{bmatrix} E_{sub}^{+} \\ E_{sub}^{-} \end{bmatrix} \tag{2.24}$$

This is the most widely used method for the mathematical study of wave transmission in one-dimensional structures [5-7], it allows the calculation of reflectivity and transmission spectra, guided modes and the optical intensity distribution in VECSEL structure. In this thesis, we used the commercial software package Essential Macleod which is an implementation of the transfer matrix algorithm (thin film center. Inc., USA) to model our multilayer devices.

2.1.2 Reflectivity

Since there is only an incident light in the substrate assumed to have an infinite length, we employ $E_{sub}^{-} = 0$ in Equation (2.24). We obtain:

$$\begin{bmatrix} E_0^{+} \\ E_0^{-} \end{bmatrix} = V_0^{-1} V_1 U_1 V_1^{-1} V_2 U_2 V_2^{-1} \cdots V_m^{-1} V_{m+1} U_{m+1} V_{m+1}^{-1} V_{m+2} U_{m+2} V_{m+2}^{-1} V_{sub} \begin{bmatrix} E_{sub}^{+} \\ 0 \end{bmatrix} \tag{2.25}$$

Thus, we can compute the electromagnetic anywhere within the structure.

The complex reflectivity coefficient for the electrical field, r is calculated as:

$$r = \frac{E_0^+}{E_0^-} \qquad (2.26)$$

From r we obtain the intensity reflectivity $R = |r|^2$ and the phase change of the reflected wave $\varphi = \arg(r)$.

In Fig. 2.4 (a), we show a typical intensity reflectivity spectrum. Considering a VECSEL structure shown in Fig. 2.1, a high reflectivity is achieved from the bottom DBR, and a microcavity resonance at the design wavelength of 1550 nm.
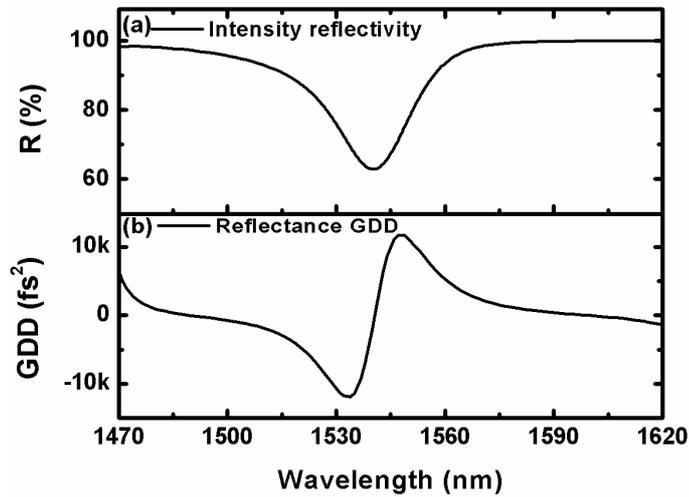
Figure 2.4 (a) Intensity reflectivity R and (b) group delay dispersion (GDD) as a function of wavelength for the resonant cavity shown in Figure 2.8.

2.1.3 Group Delay Dispersion (GDD)

The gain structure is basically a Gires-Tournois interferometer (GTI) formed by the bottom mirror and the residual reflection from the top layers. The dispersion of this microcavity depends on the microcavity optical thickness and therefore on the thickness of top layers. The general expression of GDD coefficient (in fs^2)[8] is:

$$D(\omega) = \frac{d^2\varphi(\omega)}{d\omega^2} \qquad (2.27)$$

where $\varphi(\omega)$ is the optical phase, which can be computed with the transfer-matrix algorithm described in the last section 2.1.1. In Fig. 2.4 (b), we show the calculated GDD corresponding to a resonant VECSEL structure with the intensity reflectivity shown in Fig. 2.4 (a).

For a passively mode-locked VECSEL, M. Hoffmann at ETH-Zürich (ETHZ) experimentally demonstrated that a slightly positive total cavity GDD should lead to shorter pulses in a soliton-like mode-locking [9]. The main contributions in GDD of the complete cavity arise from the VECSEL chip and the semiconductor saturable absorber mirror (SESAM) chip. Both of them have therefore to be taken into account in the mode-locked pulse formation process. The SESAM chip is also actually a Gires-Tournois interferometer, and its GDD coefficient can be calculated in the same way. This will be furthur detailed in chapter 3.

2.1.4 Longitudinal mode confinement factor

Starting from Equation (2.23) and (2.24), we present here the approach to obtain the optical intensity distribution in the structure. In the active region the electrical field forms a standing wave pattern as shown in Fig. 2.1. In order to improve the performance of VECSELs, the gain structure has to be optimized for maximizing the overlap between the active region and the peaks of the standing wave pattern at the lasing wavelength. In order to study the impact of the QWs positions on the modal gain, we use the longitudinal optical confinement factor Γz, defined as the proportion of the confined optical energy in the QWs relative to the optical energy in the whole structure. Hence, the longitudinal optical confinement factor Γ_z can be given in the form [10-11]:

$$\Gamma_z = \frac{\int\limits_{QW} |E(z,\lambda)|^2 \, dz}{\int\limits_{L} |E(z,\lambda)|^2 \, dz} \tag{2.27}$$

In Equation (2.27), the top integral of the optical field is considered over the width of the QWs in the microcavity and the bottom integral is over the entire gain structure

length L. Equation (2.27) shows that the confinement factor is proportional to the squared amplitude of the electrical field in the quantum wells. We used the reduced longitudinal confinement factor in this thesis, Γ_z' which shows the average energy confined in a quantum well [7]:

$$\Gamma_z' = \frac{1}{N_{QW}} \sum_{i=1}^{N_{QW}} \int_{QW} |E(z,\lambda)|^2 \, dz \tag{2.28}$$

where N_{QW} is the number of QWs in the microcavity. The longitudinal confinement factor controls the performance of the gain chip in several important ways. Firstly, Γ_z' determines the overall "modal" gain of the chip which is proportional to $N_{QW} \times \Gamma_z' \times g$, where g is the material gain (assumed to be constant for all the QWs in the structure). And therefore Γ_z' impacts on the laser threshold. Secondly, Γ_z' is wavelength dependent, and therefore acts as an intra-cavity spectral filter, with important consequences for the performance of the laser.

The longitudinal optical confinement factor is also a very important parameter when designing a SESAM structure. It impacts on the modulation depth (maximum nonlinear change in reflectivity) of the SESAM significantly. In this case, the longitudinal optical confinement factor can also be referred to be as absorption enhancement factor, and this will be discussed in chapter 3.

2.2 VECSEL STRUCTURE DESIGN

Fig. 2.5 shows the typical structure of our VECSEL chip. It consists of five sections: (1) Antireflection (AR) coating, (2) Phase layer, (3) Active region, (4) bottom DBR, and (5) host substrate.

Starting from the host substrate (5), most of the heat generated in the active region dissipates through the host substrate in a bottom-oriented heat dissipation scheme. The heat management requires the host substrate to have a high thermal conductivity, this will

be detailed in section 2.3. The multilayer bottom Bragg mirror (4), serves as one of the mirrors of the laser cavity. It is a critical element of the VECSEL chips (see Fig. 2.1 and 2.5). The DBR reflectivity should be very high, of the order of 99.9%, to keep the laser threshold low and the output differential efficiency high. Since this mirror also forms a thermal barrier between the active region and the heat sink, another requirement is that the mirror thermal impedance should be low, so that the heat generated in the active region is dissipated efficiently, and that the temperature rise in the active region is limited. The active region (3) is the key component of the VECSEL, and it determines the laser characteristics such as the operating wavelength, the threshold, the slope efficiency and its thermal dependence. Multiple quantum wells are placed at the antinodes of the optical field standing wave, with none, one, or several closely spaced wells at each antinodes, see Fig. 1.3. The on-chip DBR and the residual reflectivity at the VECSEL surface forms an etalon or microcavity effect, so the phase layer (2) should be optimized to get a good matching between the gain spectrum and the microcavity mode, to enhance the modal gain. Finally, the AR coating at the pump wavelength (1) is used to reduce the reflectance of the pump, thus increasing the pump absorption efficiency.

In this section, we discuss in more details the design of the different parts of the VECSEL chip (except for the host substrate), according to their functions as introduced above.
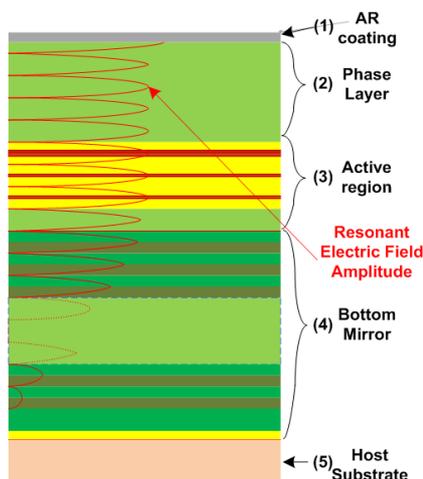
Figure 2.5 Schematic cross-sectional view of the VECSEL structure.

2.2.1 Distributed Bragg Reflector (DBR)

The bottom DBR of the VECSEL chip serves as one of the mirrors of the laser cavity. In order to keep laser threshold low and output differential efficiency high, the bottom mirror reflectivity should be very high. Since this mirror also forms a thermal barrier between the active region and the heat sink, another requirement is that the mirror thermal impedance is low. To produce efficient DBR, multiple quarter-wave layer pairs of semiconductor materials with a high refractive index contrast are required. This yields high reflectivity with fewer layer pairs and thus reduced thickness and lower thermal impedance. It is also important that the materials used in the DBR have a good thermal conductivity. In addition, the DBR materials should be non absorbing at the laser and, possibly, pump wavelengths.

The available semiconductor materials lattice-matched to InP and compatible with a lasing wavelength of 1.55 μm, only provide a small refractive index contrast. For example, the InGaAsP/InP mirrors require ~ 48 quarter-wave pairs to achieve the desired reflectivity of ~ 99.9% [12]. In contrast, high-index-contrast, lattice-matched materials such as GaAs and AlAs, are available in the GaAs material system compatible with a lasing wavelength of ~ 1 μm. A 30-pair GaAs-based mirror has the desired reflectivity of ~ 99.9% with a mirror thickness of about 4.5 μm. Both 48-pair InP/InGaAsP DBR [12]

31

and 35-pair AlAs/GaAs DBR [13] have been used as the bottom mirror for 1.55 μm VECSEL. The calculated reflectivities of the two kinds of DBR mirrors are shown in Fig. 2.6. The InP-based DBR has a lower reflectivity and narrower stopband compared to the AlAs/GaAs DBR with less pairs. As a result, VECSEL at 1.55 μm using InP-based DBR have a higher thermal impedance, and significantly lower demonstrated output powers.

For VECSEL emission wavelength at 1.55 μm, alternatives have been explored for improved mirrors considering the requirement of both reflectivity and thermal performance. In this PhD work, we have used a 17-pair metamorphic GaAs/Al$_{0.97}$Ga$_{0.03}$As semiconductor Bragg mirror whose reflectivity is enhanced thanks to the deposition of a 150 nm-thick Au layer [14-15]. The reflectivity of such a hybrid mirror is calculated to be greater than 99.9% at 1.55 μm, as shown in Fig. 2.6.
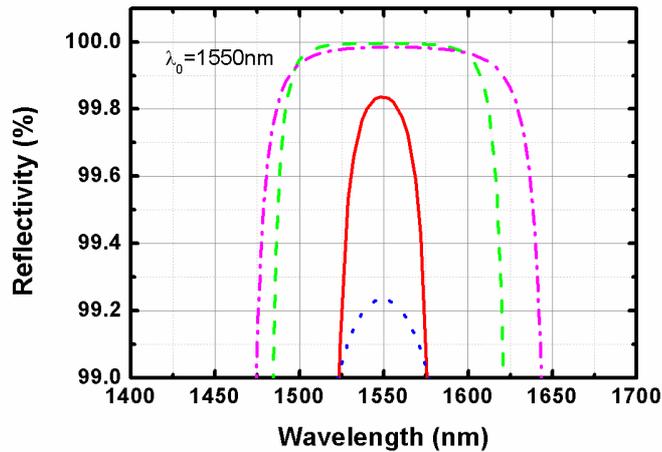
Figure 2.6 Calculated reflectivity of various DBR mirrors at 1550 nm. 48-pair InP/InGaAsP DBR mirror on InP substrate (red solid), 35-pari AlAs/GaAs DBR mirror on GaAs substrate (magnetic dash dot), 17-pair AlAs/GaAs DBR mirror on GaAs substrate (blue dot) and hybrid mirror consisting of 17-pair AlAs/GaAs DBR plus a gold mirror (green dash).

2.2.2 Active region

The function of the active region is the conversion of the pump light into the laser light and laser light amplification. Incident pump photons with higher photon energy are absorbed in separate pump-absorbing layers that also serve as the quantum well barriers.

The excited carriers, electrons and holes, then diffuse to the smaller bandgap quantum wells that provide gain, emitting lasing photons with lower photon energy.

For VECSELs in the telecom wavelength region (1550-1600nm), we can employ the InP-based material system using quaternary alloys (e.g., InGaAsP, InGaAlAs) as the active region. The active region is grown on InP substrate, consisting of 8 compressively strained (~ 1.5%) InGaAlAs quantum wells distributed among three optical standing wave antinode positions in a 4-2-2 distribution [15].

2.2.3 Phase layer and cavity mode adjustment
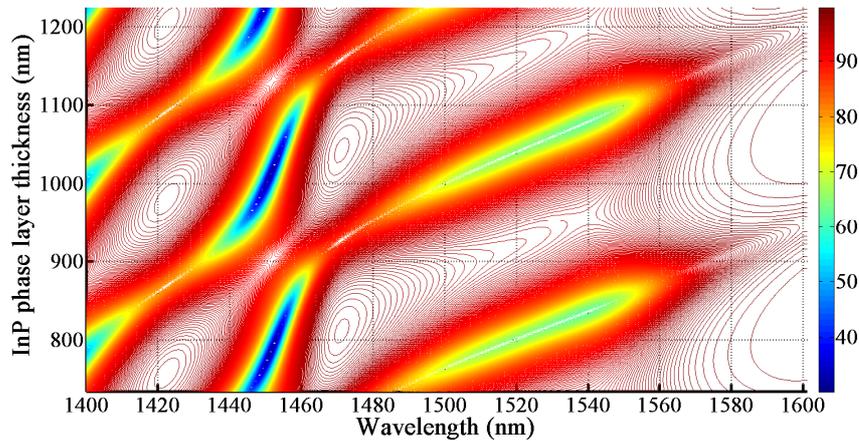
Figure 2.7   Reflectivity spectrum map as a function of the thickness of top phase layer.

As there is a Fresnel reflection at the semiconductor–air interface, this together with the Bragg reflection leads to a microcavity effect (resonance effect). Any thickness variation of the top InP phase layer leads to a microcavity mode shift. We calculated the reflectivity spectrum of our VECSEL as a function of the thickness the top phase layers, as shown in Fig. 2.7. Depending on the optical thickness of phase layer, the VECSEL microcavity can be resonant or anti-resonant at the wavelength of 1.55 μm. In the following, we discuss the properties of the resonant and antiresonant VECSEL structure respectively.
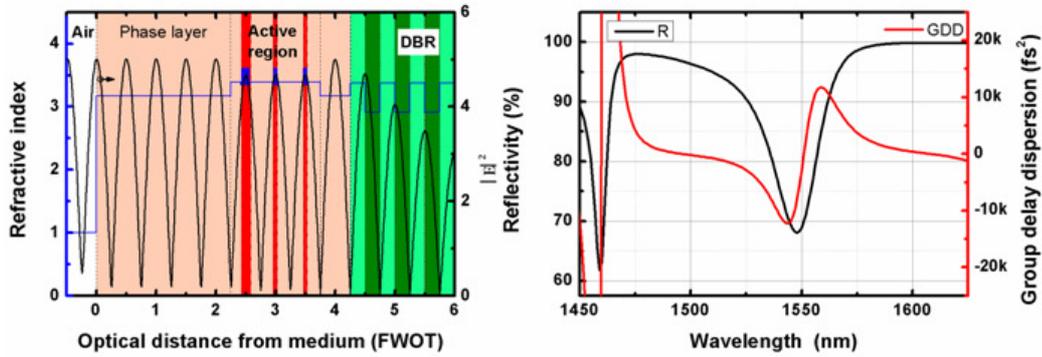
Figure 2.8 (a) Structure of a resonant VECSEL. GaAs is in green, AlGaAs is in light green; the material refractive index profile is in blue, and the normalized field intensity|E²| is plotted (black curve). (b) Intensity reflectivity (black) and group delay dispersion (red) of the resonant VECSEL as a function of the wavelength.
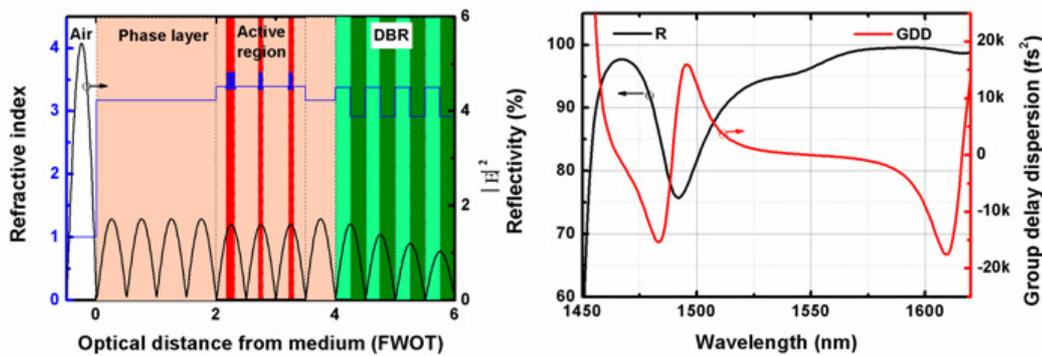

Figure 2.9 (a) Structure of an antiresonant VECSEL. GaAs is in green, AlGaAs is in light green; the material refractive index profile is in blue, and the normalized field intensity|E²| is plotted (black curve). (b) Intensity reflectivity (black) and group delay dispersion (red) of the anti-resonant VECSEL as a function of the wavelength.

The full structure design of a resonant VECSEL is shown in Fig. 2.8 (a). It shows the simulated standing wave pattern (in black) and the refractive index profile (in blue), the QWs (in red) being placed at an antinode of the standing wave. The simulated reflectivity and group delay dispersion (GDD) of this resonant structure as a function of the wavelength are plotted in Fig. 2.8 (b). The reflectivity spectrum has a big contrast at the designed wavelength 1550 nm. A steep slope in the GDD spectrum appears near the designed wavelength.

Starting from Fig. 2.8, we switch to an anti-resonant configuration at the wavelength of 1.55 μm by reducing the optical thickness of the top phase layer by λ/4. The anti-resonant structure and the simulated standing wave pattern are depicted in Fig. 2.9(a). The simulated reflectivity and GDD of this antiresonant VECSEL are plotted as a function of the wavelength in Fig. 2.9 (b).

As can be observed when comparing Fig. 2.8 and Fig. 2.9, there are big variations in reflectivity and GDD spectra when the thickness of the top InP phase layer is varied. This permits us to tune the microcavity mode by etching the top layer.

2.2.4 Antireflection (AR) coating at pump wavelength
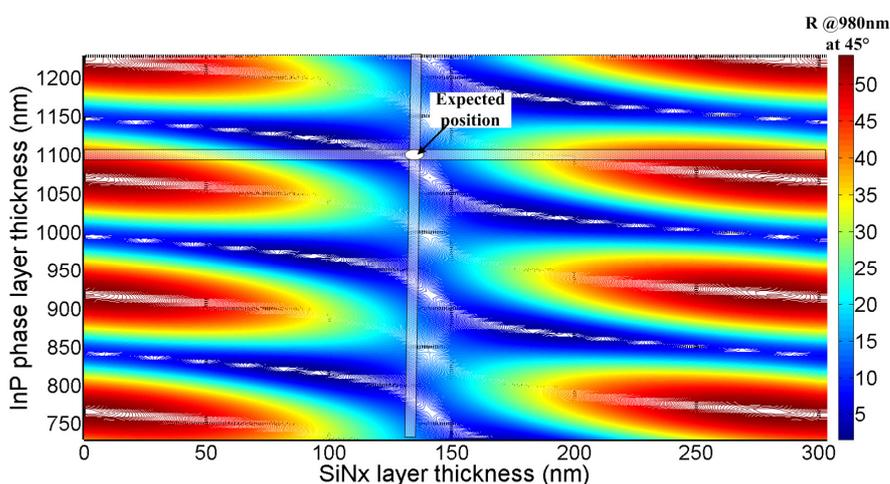
Figure 2.10 Reflectivity at pump wavelength (45°) as a function of the thickness of top phase layer and thickness of AR coating.

The residual reflectivity due to the refractive index difference at the air/InP phase layer interface is ~ 30% at the pump wavelength. In order to enhance the absorption of pump, we have deposited an anti-reflection (AR) coating for the pump laser. The pump wavelength is 980 nm and the pump beam is focused onto the surface with an incident angle of 45°. The AR coating is formed by a λ/4 single layer of silicon nitride (SiN_x). The SiN_x layer is deposited by sputtering and the refractive index of this material has been measured to be n ~ 1.95 at 1.55 μm.

We have calculated the reflectance at the pump wavelength (980nm), at an incident angle of 45°, for different thickness values of both the top phase layer (InP) and the AR coating layer (SiN_x). The SiN_x layer was considered to be perfectly transparent at 1.55 µm (extinction coefficient k=0) in the calculations. The results are shown in the map of Fig. 2.10. As can be seen in this figure, with an optimized AR coating thickness, the pump reflectance can be reduced from ~ 30% to ~ 10%.

2.3 HEAT MANAGEMENT

OP-VECSELs have been demonstrated with Watt to multi-Watt output powers. As an example, J. Lyytikäinen and co-worker at Tampere University of Technology have shown a 1.48 µm OP-VECSEL with output power up to 5 W [16]. However, the high output power critically depends on the thermal management strategy used in this type of laser.

The pump photons have a higher energy than the emitted laser photons, and the difference of the two photon energies is the quantum defect. This quantum defect is one of the major contributors to the overall laser operating efficiency. This pump–laser photon energy difference, together with the contributions from other lasing inefficiencies, has to be dissipated as heat from the device active region.

Good heat dissipation and heat sinking are critical for high-power operation of all semiconductor lasers. Without these, firstly, the temperature of the active region would rise and excited carriers would escape thermally from the quantum wells into the barrier region, thus depleting the laser gain and turning the laser off in a thermal rollover process. The temperature induced shift of the maximum gain wavelength and the refractive index variations detune the longitudinal standing wave pattern from the resonant periodic gain (RPG) of the active QWs. This results in a reduced overlap of the optical mode with the material gain, and in an effective decrease in round-trip modal gain, with an eventual rollover limiting the maximum output power.

In this section, we numerically compare the two heat dissipation techniques that have been successfully deployed to-date: the intracavity "heatspreader" technique where a platelet of high thermal conductivity is directly bonded onto the surface of VECSEL, and the bottom heat dissipation approach where the initial substrate is removed, after integration of a host substrate with high thermal conductivity. In the following, we compare the impact of different types of DBRs in the two heat dissipation techniques, and then we focus on the investigation of the thermal performance of different combinations of DBRs and substrates in the bottom heat dissipation scheme.

2.3.1 FEA Modeling in CoMsol

The finite element software CoMsol has a heat transfer module, which allows for simulating heat transfer in structures made of thin layers. This is particularly relevant to applications such as thermal management in the multilayer VECSEL. In this chapter, we use CoMsol Multiphysics software to simulate the thermal behavior of VCSELs and to evaluate the thermal performance for different heat dissipation schemes.
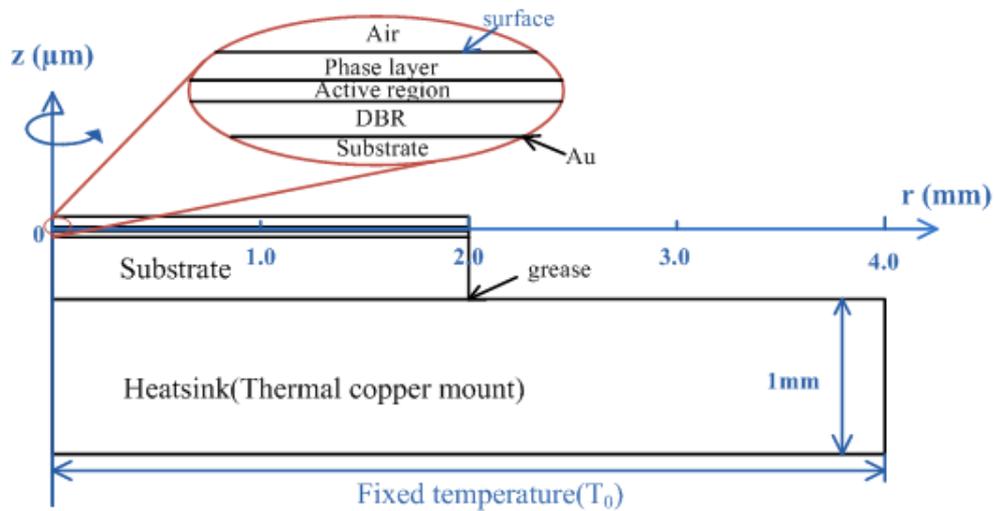

Figure 2.11. Simplified geometry for Multilayer VECSEL structure

The heat conduction equation is solved for a circularly symmetric device according to the pump beam profile, and the semiconductor structure is simplified into four parts: the

37

phase layer, the active region, the bottom DBR and the host substrate as shown in Fig. 2.11.

The three most important physical parameters in the modeling are: the heat source, the thermal conductivity of the different layers, and the heat transfer between the chip and the boundaries.

(1) *Heat source*. Firstly, pump absorption and hence heat loading is assumed to occur in the gain layer and possibly in the DBR mirror. If we assume a pump laser with gaussian profile as the pump source, the heat load in the gain region is taken to be [17-19]:

$$Q_g(r,z) = \frac{2 \cdot \eta_g \cdot P_p}{\pi \cdot \omega_p^2} \cdot \exp(-\frac{2 \cdot r^2}{\omega_p^2}) \cdot \exp(-\alpha_g(z_{g0} - z)) \qquad (2.30)$$

where r and z are the spatial coordinates, η_g is the fraction of the pump power absorbed in the gain region converted to heat; α_g is the effective absorption coefficient; P_p is the pump power reaching the gain region; ω_p is the $1/e^2$ radius of the pump, and z_{g0} is the z-coordinate of the interface between the gain and top layers.

The heat load in the DBR mirror is given by

$$Q_d(r,z) = \frac{2 \cdot \eta_d \cdot P_p}{\pi \cdot \omega_p^2} \cdot \exp(-\frac{2 \cdot r^2}{\omega_p^2}) \cdot \exp(-\alpha_d(z_{d0} - z)) \cdot \exp(-\alpha_g \cdot t_g) \quad (2.31)$$

where η_d is the fraction of the pump power absorbed converted to heat in the DBR; α_d is the effective pump absorption coefficient in the DBR layer; z_{d0} is the z-coordinate of the interface between the active region and DBR layer, and t_g is the thickness of the active region.

The effective pump absorption coefficient of a multi-layer stack consisting of N thin layers is given by:

$$\alpha = \frac{\sum_{n=1}^{N} \alpha_n \cdot d(z,n)}{\sum_{n=1}^{N} d(z,n)} \qquad (2.32)$$

where α_n is the pump absorption of the n-th layer and $d(z,n)$ is its thickness.

The α_g and α_d coefficients used in Equations (2.30) and (2.31) are calculated using the Equation (2.32).

(2) *Effective thermal conductivity.* As described before, the simplified gain layer and DBR layer are composed of many layers consisting of different materials. The typical layer thickness in the vertical direction ranges from ~10 nm (QW) to ~ 200 nm (quarter wavelength thickness in the Bragg mirror), while the typical dimension in the radial direction is several times the pump spot size that is ~100 µm. Owing to the very large scale difference in the vertical and radial directions, the effective thermal conductivity is different in the two directions. In the gain layer, we define the equivalent thermal conductivity of the multilayer in radial and vertical directions as [20]:

$$\kappa_r = \frac{\sum_{n=1}^{N} d(z,n) \cdot \kappa_n}{\sum_{n=1}^{N} d(z,n)} \tag{2.33}$$

$$\kappa_z = \frac{\sum_{n=1}^{N} d(z,n)}{\sum_{n=1}^{N} d(z,n)/\kappa_n} \tag{2.34}$$

In Equation (2.33) and (2.34), κ_r is the equivalent thermal conductivity in radial direction, and κ_z is the equivalent thermal conductivity in vertical direction. $d(z,n)$ and κ_n represent the thickness and the bulk thermal conductivity of the n-th layer, N is the number of layers.

As for the DBR, the quarter wavelength layer distribution is periodic, and we can express the effective thermal conductivity as:

$$\kappa_{r,DBR} = \frac{n_2 \kappa_1 + n_1 \kappa_2}{n_1 + n_2} \tag{2.35}$$

$$\kappa_{z,DBR} = \frac{n_2 + n_1}{n_1/\kappa_2 + n_2/\kappa_1} \tag{2.36}$$

$$\frac{\lambda}{4} = n_1 d_1 = n_2 d_2 \tag{2.37}$$

where n_1 and n_2 are the refractive indices of two adjacent layers, κ_1 and κ_2 are their thermal conductivities respectively. It should be noted that the thermal conductivity calculated by this method is slightly overestimated due to phonon scattering [21], different in the bulk material and in thin film.

In our simulation, diode laser pumping with a gaussian profile at 980nm is assumed. The InP-based part of the VECSEL structure for 1.55 μm laser emitting is kept unchanged for comparison purpose. It includes 8 compressively strained InGaAlAs QWs and is further described in section 2.4. We used different types of DBRs for comparison. The fraction of the pump power absorbed in the active region converted to heat, η_g is 0.37 due to the quantum defect between the pump and laser photon energies. All pump light absorbed in the DBR is assumed to be converted to heat. In the simulation, all the thermal conductivities are kept constant and equal to the values at 300 K and the internal interfaces are assumed perfectly conducting.

(3) *Boundary conditions*. In the vertical direction, the bottom part of the heatsink is kept at a constant temperature as shown in Fig. 2.11, while the top surface of the structure is considered as thermally insulated (air convection is neglected). In the radial direction, symmetric boundary conditions are used at the axis of rotation. The radius of the VECSEL chip is set to 2 mm, which is at least 12 times larger than the pump spot radius in the simulations. In this case, thermal insulation is assumed at the edge of VECSEL chip. The temperature rise in the active region has been calculated for a fixed average pump power density of 10 kW/cm^2.

TABLE 2.1 Thermal conductivity values and layer thickness values used in the thermal simulations.[22-23]

layers	Effective thermal conductivity (W/(K*m))	Layer thickness (μm)
Heatspreader	2000	300
InP phase layer	68	1.1
Quartenary active region	4.5	0.7
48-pair InP/InGaAsP DBR	K_r=38.5 K_z=12.7	11.3
35-pair GaAs/AlGaAs DBR	K_r=74.4 K_z=69.9	9.3
17- pair GaAs/AlGaAs DBR	K_r=74.4 K_z=69.9	4
InP substrate	68	300
GaAs substrate	55	300
CVD diamond	2000	300
Copper	400	varied
Au	300	150
AuIn$_2$	162	0.4
Grease	0.9	30
In	81	50
Cu Heatsink	400	1000

2.3.2 Intracavity heat dissipation scheme

To date, many reports have demonstrated that intracavity diamond heatspreader bonded to the VECSEL surface is the most effective heat dissipation approach [13, 16, 24-26]. Therefore VECSELs associated to a 300-µm thick intracavity diamond heatspreader have first been considered in the simulation as a thermal reference. VECSELs with the same InP-based active region but with different bottom Bragg mirrors and substrates have been considered: a 48-pair InP/InGaAsP Bragg mirror on InP substrate, a 35-pair GaAs/Al$_{0.97}$GaAs Bragg mirror on GaAs substrate, and the limit case with no Bragg mirror nor substrate. These two types of Bragg mirror have been used for a 1.55 µm VECSEL [12-13], both of them have a reflectivity beyond 99.9%. Fig. 2.12

shows the geometry used in the modeling. The yellow dashed line in the right-hand side indicates the thermal short-cut (made of copper) between the bottom and top heatsinks, and the position of the top heatsink is shown. Results in Fig. 2.12 reveal that the heat dissipation mostly occurs through the top-mounted natural diamond when it is used as intra-cavity heat spreader. The thermal impedance of the bottom Bragg mirror and of the substrate in the VECSEL chip has a negligible impact on the temperature increase in the active layer in this case. A temperature rise lower than 10 K is systematically calculated (10 kW/cm^2 pump power density) for a pump spot radius up to 150 µm.
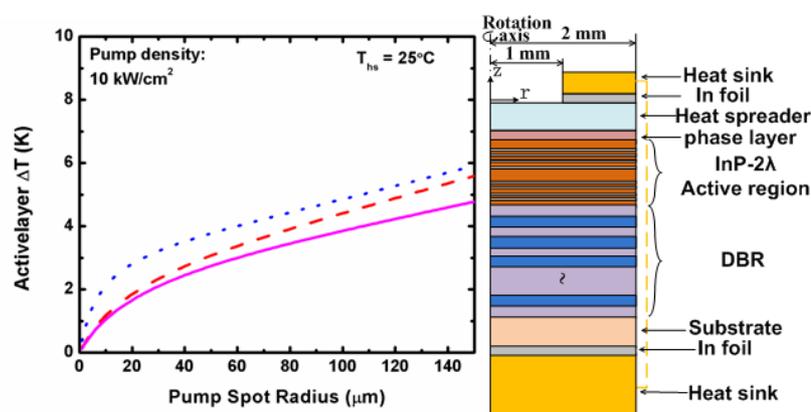

Figure 2.12: Temperature rise in active layer calculated versus pump spot radius for a 300-µm thick diamond heat spreader and with different DBRs and substrates: 35-pair GaAs/AlGaAs DBR mirror on GaAs substrate (red dash), and 48-pair InP/InGaAsP DBR mirror on InP substrate (blue dot). The limit case of the active region directly bonded onto the same heat spreader is a reference (magenta line).

2.3.3 Bottom heat dissipation

The above described result demonstrates that the heatspreader has a good thermal behaviour. However the heatspreader on a VECSEL in a mode-locking cavity may introduce an unwanted spectral selection effect [27]. Moreover it is not easily compatible with electrical pumping of the VECSEL chip. An alternative approach to the intracavity heatspreader is the downward heat dissipation scheme. In the downward heat sinking approach, the thermal impedance of the bottom mirror and substrate becomes of paramount importance.

2.3.3.1 Influence of the DBR structure
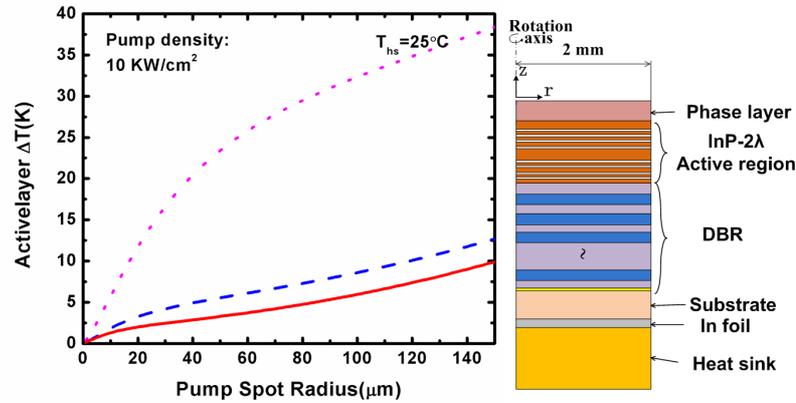
Figure 2.13: Temperature rise in the active region calculated versus pump spot radius for different DBR mirrors with 300-µm thick CVD diamond substrates: 17-pair GaAs/AlGaAs –Au hybrid mirror (red solid), 35-pair GaAs/AlGaAs DBR mirror (blue dash), 48-pair InP/InGaAsP DBR mirror (magenta dot).

We have already demonstrated that the thermal impedance of the bottom Bragg mirror and of the substrate in the VECSEL chip generally has a negligible impact on the temperature increase in the active region in the heatspreader approach. This is not the case in the downward heat dissipation scheme. First, we highlight the influence of the thermal impedance of the Bragg mirror on the temperature rise in the active region. The substrate is a 300-µm thick CVD diamond. Three different mirrors are considered, a 48-pair InP/InGaAsP Bragg mirror, a 35-pair GaAs/AlGaAs Bragg mirror, and a 17-pair GaAs/AlAs – Au hybrid mirror, they all present similar reflectivity. In this simulation, the same active region is used as for the calculations of Fig. 2.12. Results in Fig. 2.13 reveal that the thermal impedance of the bottom Bragg mirror in the VECSEL chip has a significant impact on the temperature increase in the active layer. A temperature rise difference higher than 25 K is systematically calculated (10 kW/cm^2 pump power density) for a pump spot radius up to 150 µm between the InP-based DBR and the GaAs-based DBR mirror. The results from Fig. 2.13 indicate that a hybrid mirror has a better thermal behavior than a monolithic 35-pair GaAs/AlAs Bragg mirror in the bottom heat dissipation scheme.

2.3.3.2 Influence of substrate

We have highlighted the advantage of a hybrid metal (Au) – metamorphic GaAs/AlGaAs mirror. Let's consider the impact of the host substrate on the temperature rise in the active region. The same active region as for the calculations of Fig. 2.12 and Fig. 2.13 is considered, it is combined with a 17-pair GaAs/Al$_{97\%}$GaAs – Au hybrid mirror. The structure is associated to a CVD diamond host substrate via metallic bonding, or to a Cu substrate. As we know, CVD diamond has thermal conductivity up to 2000 W/(K*m), and both simulation and experiment results show its good thermal behavior. However, considering the high cost of diamond and its incompatibility with easy dicing or current injection, we tried to use copper instead in the bottom dissipation approach. Copper has the highest thermal conductivity among metals and its cost is quite low.

We investigated the thermal impendence of different substrates in VECSEL chips by calculating the temperature rise in the active region versus pump spot radius, the results are shown in Fig. 2.14. For pump spot radius larger than 20 µm, the CVD diamond substrate leads to superior performances with a significant reduction of the temperature rise in the active region. Moreover a quasi one-dimensional heat flow can be observed with this substrate for large pump diameters, of particular interest for power scaling. However the results of Fig. 2.14 indicate that a cost-effective version consisting in the use of a Cu host substrate, will also lead to a low temperature increase for VECSELs with a pump radius in the range of 20 µm-40 µm. $\Delta T \leq 20$ K is obtained even for a pump radius up to 100 µm. It was shown experimentally in the PHOTEL group at LPN that the thermal roll-over effect occurs typically for a temperature rise of ~30 K in the L-I curve for electrically-pumped 1.55 µm VECSELs with similar active region. Considering this earlier result, we can set $\Delta T \approx 30$ K as the upper authorized limit for the temperature rise in the active region.
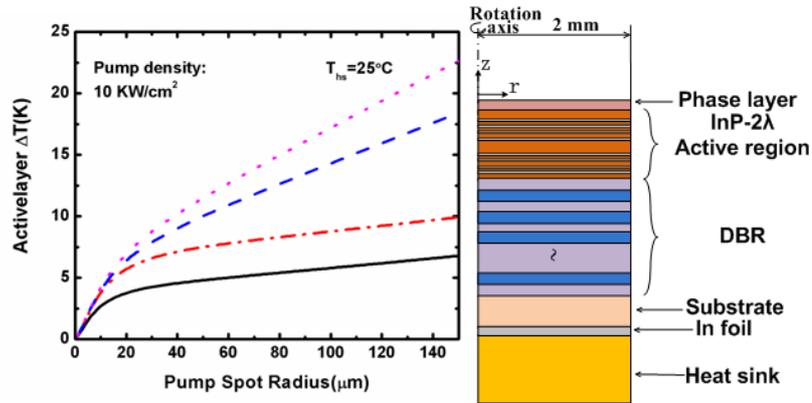
Figure 2.14. Temperature rise in active region calculated versus pump spot radius for a hybrid GaAs/AlGaAs-gold mirror with different host substrates: 300-µm thick CVD diamond (red dash dot), 150-µm thick copper (blue dash), and 150-µm thick gold (magenta dot). The limit case of the active region directly bonded onto 300 µm diamond host substrate with no bottom mirror nor substrate is also reported as a reference (black line).
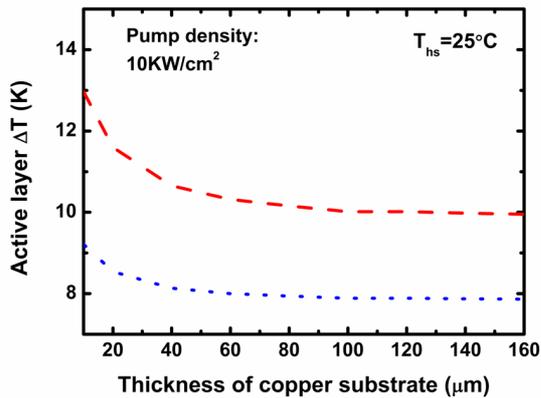
Figure 2.15. Temperature rise in the active region versus electro-deposited copper substrate thickness for a pump spot with radius of 30 µm (blue dot) and 50 µm (red dash). The thermal conductivity of electroplated copper is fixed to κ_{Cu} =400 W/m*K.

In the calculations of Fig. 2.14, the thickness of the metallic substrate was fixed to 150 µm. In order to optimize the thickness of the copper substrate, the temperature rise in the active region ΔT is calculated versus copper thickness for different pump spot radii, and the calculated curves are displayed in Fig. 2.15. Simulation results reported in Fig 2.15 show that the copper thickness should be larger than ~ 80 µm for efficient heat dissipation for pump spot radius in the 30 µm- 50 µm range.

45

2.4 VECSEL FABRICATION

The 1.55 μm VECSELs have been grown on InP semiconductor wafers using metal-organic vapor-phase epitaxy (MOVPE) techniques at 3-5 Lab. The VECSEL fabrication processes are shown in Fig. 2.16.

In Fig. 2.16-(1), the InP-based 2λ-thick active region, grown on an InP substrate, includes eight strained InGaAlAs quantum wells distributed among three optical standing-wave antinode positions. Etch-stop layers grown on top of the InP substrate enable the removal of the InP substrate, resulting in an active region directly in contact with the host substrate.
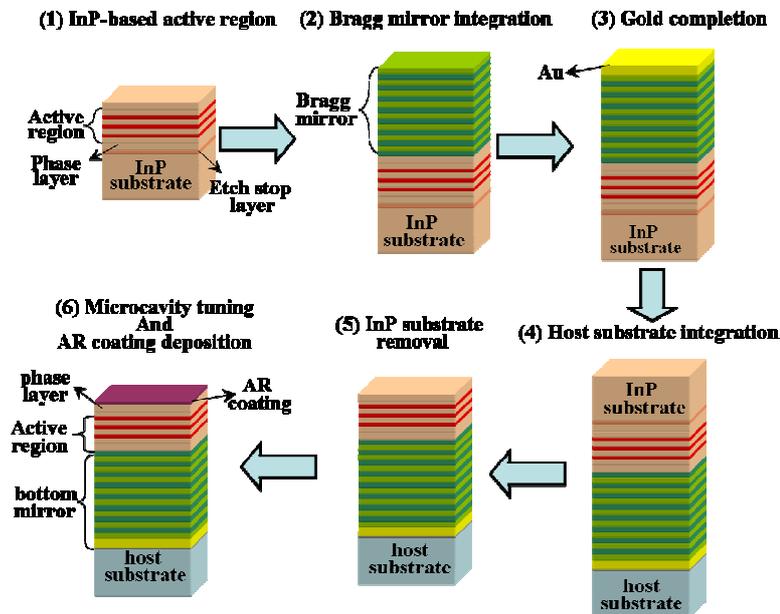
Figure 2.16 Fabrication process of our VECSEL chips

In step (2), the 17-pair GaAs/Al$_{0.97}$Ga$_{0.03}$As semiconductor Bragg mirror is integrated to the active region by both metamorphic [15] and wafer fusion [28-29]. We will introduce these two methods in section 2.4.1. Then, an additional 150 nm-thick Au layer is deposited on the surface of the Bragg mirror to enhance reflectivity of bottom mirror (step (3)). The semiconductor chip with deposited gold is then integrated to a host substrate in step (4), two different approaches are employed and discussed in section 2.4.2. In step (5), the InP substrate is removed by both mechanical polishing and wet

46

selective etching at room temperature. Finally in step (6), the InP phase layer is etched and the AR coating at 980 nm is deposited, so that the position of the resonant half-cavity mode of the VECSEL chip is close to the gain maximum after AR layer deposition.

2.4.1 Integration of the GaAs/AlGaAs DBR

From temperature calculation in the active region of 1.55um VECSELs, we have shown that the InP-based quaternary alloys (InGaAsP or InAlGaAs) that form the DBR is hampered by the very low thermal conductivity of these materials, resulting in high thermal impedance. One solution to this problem consists in replacing the as-grown InP-based DBR with an GaAs/AlGaAs DBR with better thermal conductivity.

Practically, two different techniques may be used. (1) metamorphic epitaxy. The GaAs/AlGaAs Bragg is re-grown on the InP based active region, using molecular beam epitaxy (MBE) epitaxy [15]. (2) Wafer fusion. The GaAs/AlGaAs Bragg mirror is firstly grown separately on a GaAs substrate and is subsequently assembled with the InP-based active region by wafer fusion. Finally, the GaAs substrate is etched away [28-29].

Both techniques were investigated in this PhD work, and have led to similar results. The metamorphic regrowth was performed at LPN (Marcoussis), while the wafer fusion was performed in collaboration with A. Sirbu and A. Mereuta at EPFL (Lausanne). The epitaxial structures were prepared at LPN, while the wafer fusion and GaAs substrate removal steps were undertaken at EPFL. The group in EPFL indeed pioneered this approach in the 1990's for the fabrication of monolithic VCSELs.

A dramatically improved thermal performance of 1.55 um VECSELs was demonstrated using GaAs/AlAs-based mirror with InP-based gain structure by the two techniques.

2.4.2 Host substrate assembly

2.4.2.1 Metallic bonding (AuIn$_2$)

VECSEL structures in this thesis have been bonded onto different host substrates on the Bragg mirror side by eutectic bonding with AuIn$_2$ [30].
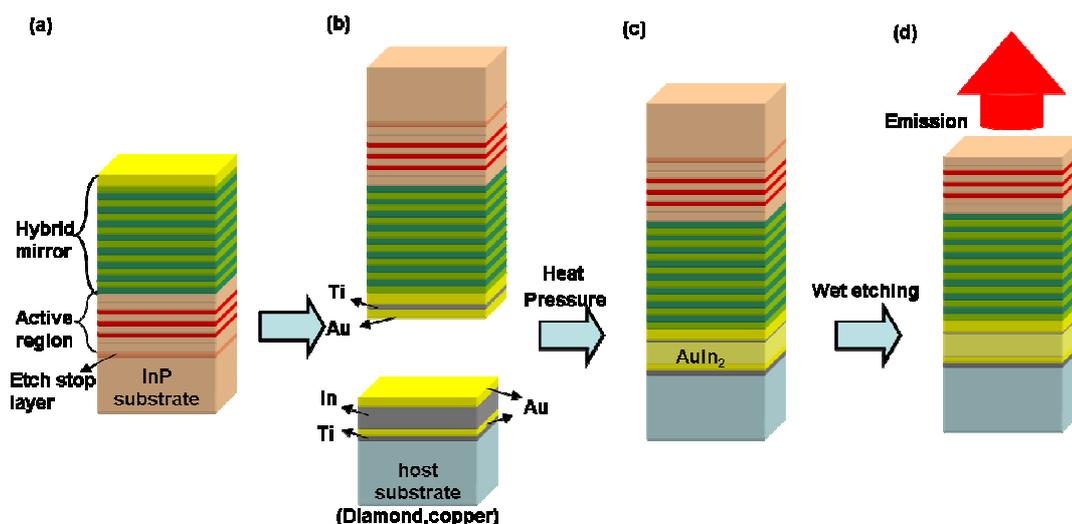

Fig 2.17 Description of the eutectic AuIn2 bonding process of the VECSEL structure onto a host substrate

On the VECSEL side, a 150 nm thick Au layer was first evaporated to enhance the reflectivity of the back mirror. Then a 30 nm Ti layer was evaporated on both the VECSEL and the host substrate to improve adhesion and to prevent diffusion. Next, a 150 nm –thick Au layer was deposited on the VECSEL sample. On top of the host substrate, Au (150 nm) and In (2000 nm) layers were evaporated, then a 20 nm-thick Au layer was evaporated to prevent the oxidation of the Indium layer prior to bonding. The two samples were assembled and pressed with a force of about 250 kg / cm² to provide a good surface contact of the two wafers while the temperature was ramped to 250° C and maintained at this temperature for two hours. The bonding temperature is a trade-off between the diffusion speed and the strain introduced by the bonding process due to the different thermal expansion coefficients of the materials. The pressure was kept constant during the cooling-down process. Fig. 2.17 illustrates the metallic bonding process. This

technique was used to assemble the CVD diamond substrate, but also for the assembly of a Cu plate used as a host substrate.

2.4.2.2 Electroplated metallic substrate

The electrodeposition process is well suited to make films of metals such as copper, gold and nickel. The films can be made in any thickness from ~1 µm to >100 µm [31-32]. The electrodeposition process requires applying an external electrical potential, which requires electrical contact to the substrate when immersed in the liquid bath. In any case, the surface of the sample must have an electrically conducting coating before that the electrodeposition can be done. The deposition configuration is shown in Fig. 2.18.

In the case of electrodeposited substrates, the main challenges in the electro-deposition technology are to deposit a dense material with low strain and a good homogeneity with reduced edge effects. As for deposition uniformity, the technology should meet three key requirements: the solution composition must remain constant over time, the potential on the wafer surface must be uniform, and the mass transport conditions must be uniform [33].

We used home made copper electro deposition bath with commercial additive from ROHM to produce stable thick copper deposits and accelerate the rate of copper deposition. A 150 μm thick copper layer was electroplated on the 7×7 mm^2 VECSEL chip in electrolytes containing (g.cm^{-3}): $CuSO_4 \cdot 5\ H_2O$ – 0.075, H_2SO_4 – 0.196 at a electrical current density of 60 mA.cm^{-2} at 20 °C. For gold electroplating, we used the Gold-SF commercial product from METAKEM to get 120 μm thick gold substrate at electrical current density of ~ 30 mA.cm^{-2} at 45 °C. The motive force of turbulent fluid flow directed the particles to the cathode surface and prevented them from sedimentation in the bulk of electrolyte. After electrodeposition, the deposited copper is polished to a fixed thickness of ~150 µm, in order to eliminate edge effects and to obtain a flat bottom surface for a good contact with the submount. The InP substrate is removed after this polishing step.
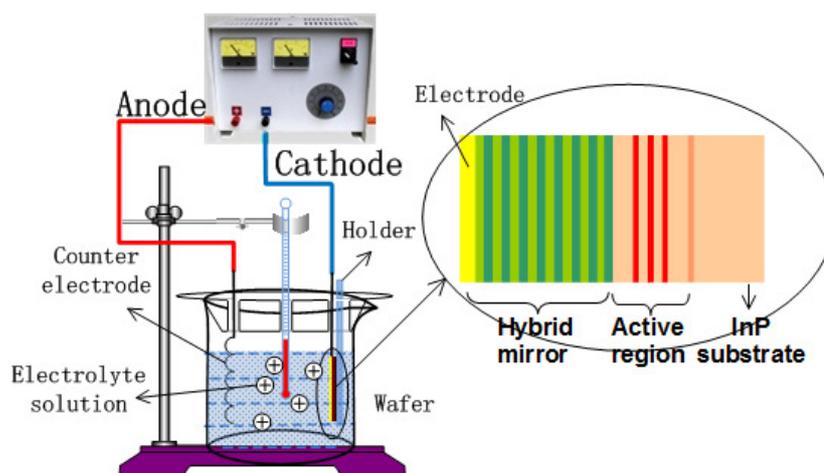
Fig 2.18 Electrodeposition set-up the integration of copper or gold substrate to be the VECSEL structure

2.5 OPTICAL CHARACTERIZATION

In this section, we report on the photoluminescence (PL) spectrum of the as grown active region in Fig. 2.16-(1) and of a fully processed VECSEL structure (without AR coating) in Fig. 2.16-(5). We also introduce a method to evaluate the thermal resistance of the VECSEL chip from the PL spectrum shift.

2.5.1 Photoluminescence (PL) of active region

Photoluminescence is often used in the context of semiconductor devices. Here, photoluminescence is excited by illumination of the device with light which has a photon energy above the bandgap energy. Photoluminescence then occurs for wavelengths around the bandgap wavelength. The optical spectrum of the photoluminescence (PL spectrum) and also the dependence of its intensity on the irradiation intensity and on the device temperature can deliver important information about the device. In particular, PL spectra give access to the bandgap energy of QWs and to the wavelength of maximum gain [34].
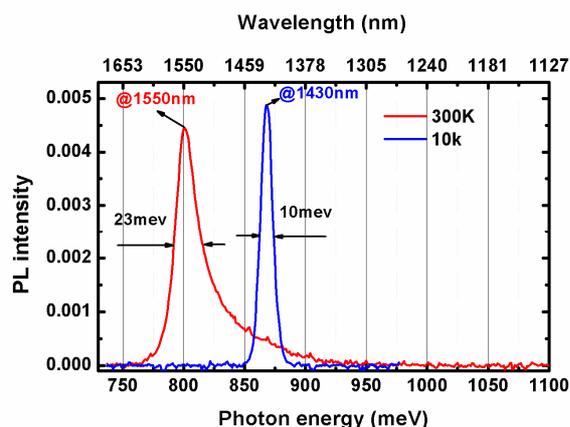
Figure 2.19 Measured photoluminescence signal of the strained InGaAlAs QWs at 10 K and 300 K excited by a 470 nm pump laser

We investigated the photoluminescence of the QWs in the as-grown InP-based active region, corresponding to step (1) in Fig. 2.16. A pump laser ($\lambda \sim$ 470 nm) was focused on the surface of the as-grown structure. In Fig. 2.19, at the low temperature of 10 K, the PL spectrum peak is at 1430 nm and its FWHM is 10 mev. There is a red shift (~0.4 nm/K) in the peak positions and a spectral broadening with increasing temperature due to thermal expansion. At room temperature the PL spectrum peaks at 1550 nm as we expected.

2.5.2 Surface PL of VECSEL

In the previous section, we have presented the PL spectrum of the quantum wells from the structure without strong microcavity effect. A direct comparison between the pure material PL and the PL measured from the surface of VECSEL chip gives valuable information about microcavity effect. In structures with strong cavity effects such as VECSELs, the PL is strongly modified on its way from the quantum wells to the surface by reflections at the various interfaces and subsequent interferences. This can be seen from the measured QW PL in Fig. 2.19 and VECSEL surface PL in Fig. 2.20(b). In Fig. 2.20, the cavity resonance is close to the gain maximum, and the microcavity effect on the PL spectrum is obvious.

51
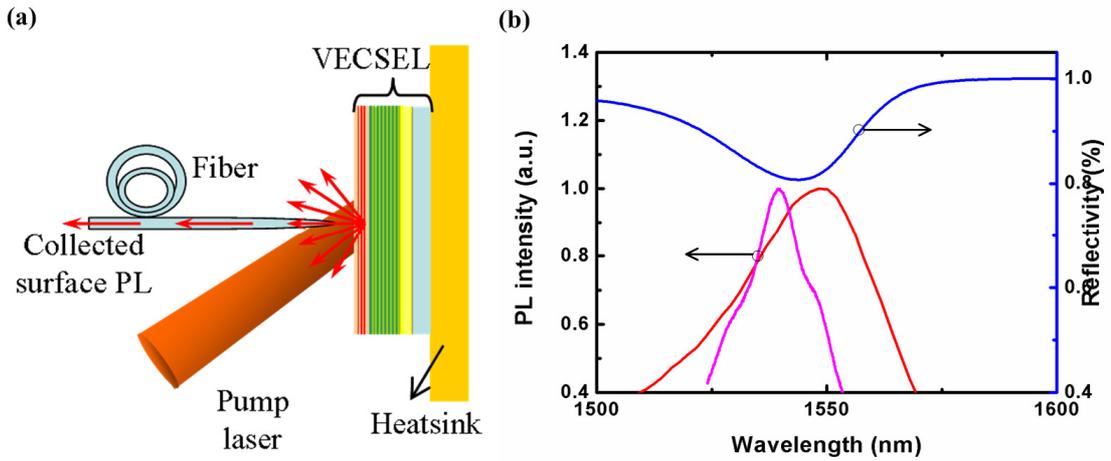
Fig 2.20 (a) Simplified experimental setup for collecting the surface PL signal from the VECSEL chip excited by a 980 nm pump laser. (b) Normalized QW PL (red line) and surface PL of VECSEL chip (magenta line) at room temperature. The cavity mode (reflectivity spectrum, blue line) indicates the strong cavity effect of VECSEL chip.

On the other hand, in a VECSEL structure where material PL and cavity resonance are fairly detuned, the lineshape of the surface-PL is more complicated, showing multiple-peak structure. Neither peak is exactly at the position of the maximum of the material PL or the cavity resonance.
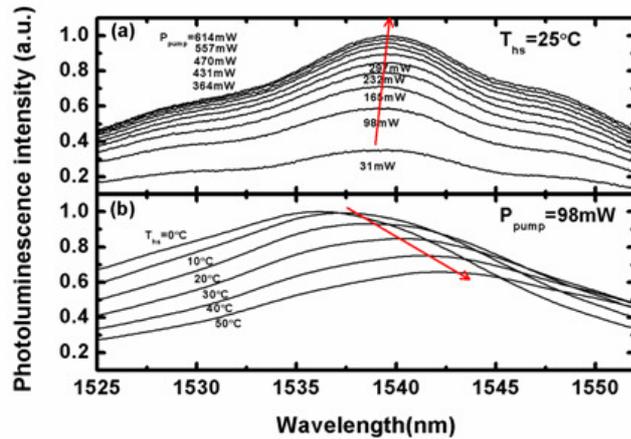
Figure 2.21 Surface PL spectrum shift measured (a) as a function of absorbed pump power at constant heatsink temperature of 25   , and (b) as a function of heatsink temperature at low pump power.

The PL spectrum of the VECSEL will shift when the pump power is varied, or when the heatsink temperature is modified. An example of the PL shift, along with the heatsink temperature and absorbed pump power, is shown in Fig. 2.21. This PL shift will allow us

to estimate the thermal resistance of the VECSEL chip, as will be detailed later in the thermal management section.

2.6 VECSEL CAVITY DESIGN
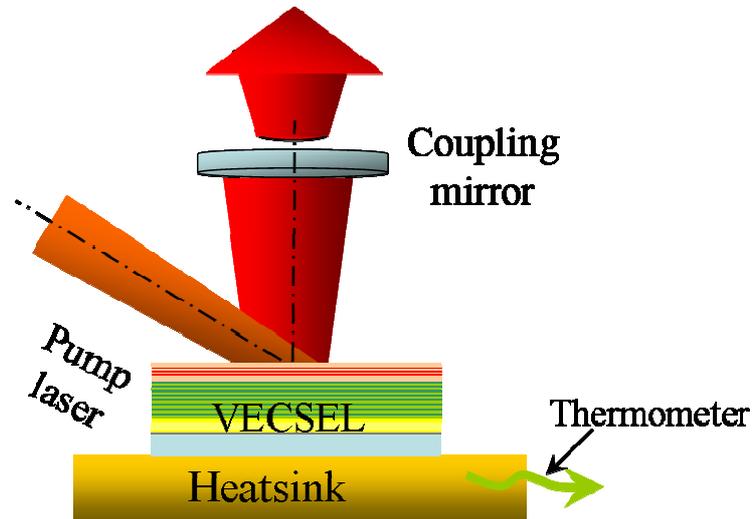
Figure 2.22 VECSEL plane-concave cavity setup. The VECSEL chip is attached to a copper mount with heat conductive paste. The temperature of the copper plate is measured with a 10-kΩ thermistor. The copper plate temperature is regulated with a peltier element, which is fixed to a heatsink. The heat is dissipated from the heatsink with a van or with water cooling system.

In this section, we describe the plane-concave cavity used to test the VECSELs. Except for the on-chip bottom mirror, the other optical elements forming the laser cavity are external to the VECSEL chip. The optical cavity allows to control the laser fundamental transverse mode operation as well as to insert various intracavity elements: optical filters for laser wavelength selection and tuning, saturable absorbers for laser passive mode locking, nonlinear optical crystals for intracavity second harmonic generation, and so on.

In the following, we firstly discuss the plane-concave cavity set-up as shown in Fig. 2.22. Then, we introduce two types of pump systems employed. Finally, we present the different coupling mirrors, and the methods used to control the VECSEL temperature.

2.6.1 Cavity design

In a two-mirror, plane–concave optical cavity of length L_c and with concave mirror radius of curvature (ROC) R_{oc} (see in Fig. 2.23(a)), the $TE_{0,0}$ stable fundamental mode is a Gaussian beam with $(1/e^2)$ radius ω_{VECSEL} on the planar semiconductor chip and ω_{oc} on the output coupler mirror given by [4]:

$$\omega_{VECSEL}^2 = \frac{\lambda_{laser}L_c}{\pi}\sqrt{(R_{oc}-L_c)/L_c} \qquad (2.38)$$

$$\omega_{oc}^2 = \frac{\lambda_{laser}R_{oc}}{\pi}\sqrt{L_c/(R_{oc}-L_c)} \qquad (2.39)$$
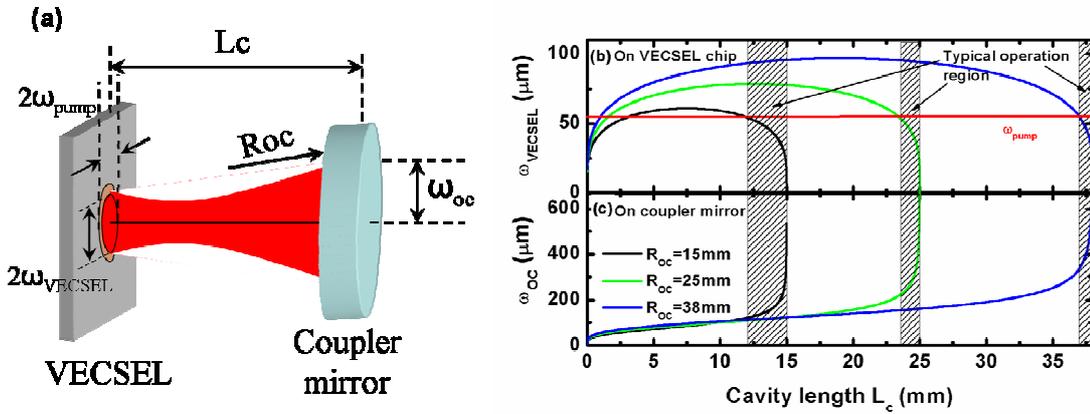
Fig. 2.23 (a) schematics of a laser cavity with the laser beam in red and focused pump spot in orange. (b) calculated value of the cavity mode radius ω_{VECSEL} on the surface of the VECSEL chip as a function of cavity length L_c, for two different concave output mirror (R_{oc}=15 mm, R_{oc}=25 mm, and R_{oc}=38 mm). (c) calculated values of the mode radius on the surface of the concave mirror as a function of cavity length Lc, for radius of curvature R_{oc}=15 mm, R_{oc}=25 mm, and R_{oc}=38 mm. The wavelength is 1550 nm.

Fig. 2.23 (b) and (c) illustrate the variation of the cavity mode radius on the two cavity mirrors, as a function of the cavity length, for a given concave mirror. Mode diameters (diameter is $2\cdot\omega$) on the VECSEL chip can be varied easily by adjusting the cavity lengths, the typical operation region for coupler mirrors with radius of curve (R_{oc}=15 mm, R_{oc}=25 mm, and R_{oc}=38 mm) are shown in Fig.2.23 (b). The pump spot size should be of the order of the laser mode size on the chip to provide efficient gain aperture for fundamental transverse mode selection.

It should be mentioned that the two-mirror cavity VECSELs have also been been operated in an unstable resonator regime with cavity lengths longer than the mirror radius of curvature. In this case, the laser transverse mode is stabilized by a gain aperture effect, with strong optical loss outside the pumped spot on the chip.

2.6.2 Pump system

In analogy with diode-pumped solid state lasers, an optical pumping scheme is also used with VECSELs. Optical pumping provides a uniform transverse carrier excitation across a very wide range of VECSEL emission apertures from 50 to 1000 μm in diameter. Also, no carrier transport to the active region from remote doped layers is required from the surfaces through the multiple quantum wells across the device thickness, as the pump light propagates throughout the device thickness to deliver the excitation. The OP-VECSEL structures are undoped, which is easier to grow and avoid free-carrier absorption; also, no complicated wafer processing is required.

In this thesis, two kinds of pump laser have been used. (1) A single transverse mode pump laser which allows to easily obtain a small pump spot (<100 μm), leading to low pump power at lasing threshold and high lasing efficiency. (2) A multimode pump laser which has a larger pump spot and a higher output power, favorable for power scaling, especially in a passively mode-locked system. In the configuration shown in Fig. 2.24, the pump laser was injected to the VECSEL chip with an incident angle of $45°$ and the elliptical pump spot size was measured by an InGaAs camera. The scale of the CCD camera image was calibrated using a specific sample with calibrated geometrical patterns. Using this procedure, the pump spot size can be estimated with a typical spatial resolution of ~ 10 μm.The typical pump spot diameter on VECSEL is 60μm*80μm for the single mode pump laser, and 100μm*120μm for the multimode pump laser, as shown in Fig. 2.24.
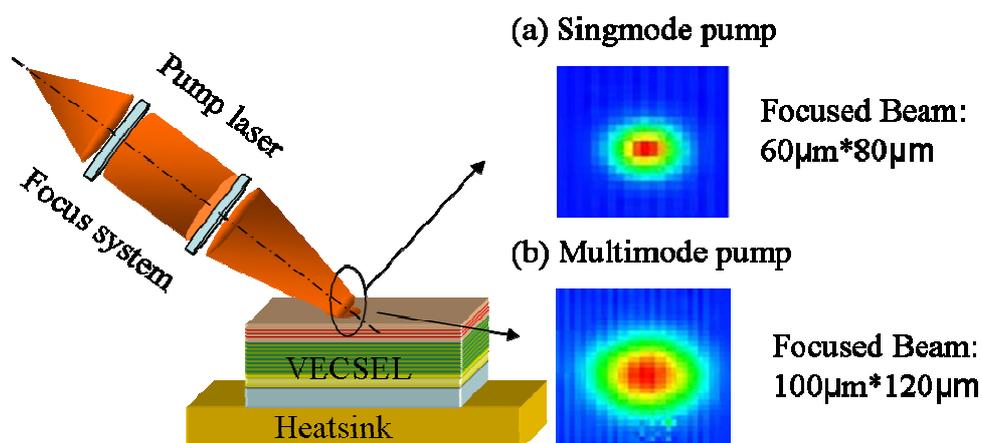
Fig 2.24 Configuration of the pump laser focus system and two kinds of pump laser with the focused pump spot images on the surface of the VECSEL chip for the single mode pump laser (a), and for the multimode pump laser (b).

2.6.3 Other controllable parameters
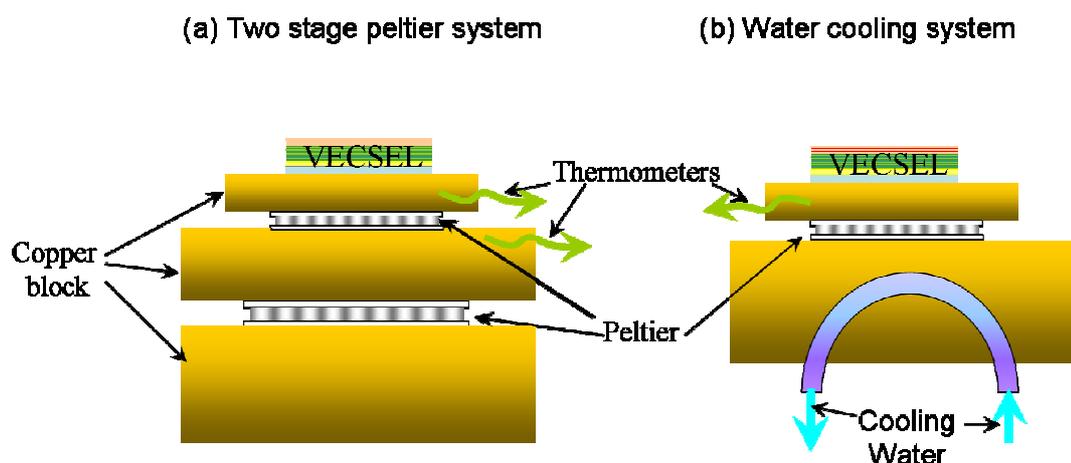
Figure 2.25 Two types cooling system employed in this thesis.

In the testbed, we can investigate the effect of the temperature of the VECSEL chip on the lasing performance. We used two different types of cooling systems depending on the employed pump laser. For the single mode pump laser whose maximum power is below 615 mW, we used a two stage Peltier mount and a radiator to control the heatsink temperature ranging from 0℃ to 50℃, as illustrated in Fig. 2.25(a). The heat can be dissipated from the radiator by forced air convection using a van. For the multimode pump laser whose maximum power can reach ~8W, the last cooling system is not

powerful enough to keep the heatsink temperature at a constant and low level. Water cooling system is more efficient and is used in this case as illustrated in Fig. 2.25 (b). In this chapter, we have mainly used the high power multimode pump in order to check the maximum achievable output power, which is very interesting for mode-locking.

Besides the temperature of the VECSEL chip, a factor that affects the lasing performance in the pump power limited regime is the coupling mirror. In this thesis, we have used concave mirrors with ROC of 15 mm, 25 mm, 38mm and reflectivities of 99% and 99.5 %. We used them to optimize the output power under the single mode laser pumping. This will be detailed in section 2.7.2.

2.7 CONTINUOUS-WAVE (CW) CHARACTERIZATION

In this section, the thermal performance of VECSELs with different host substrates are evaluated experimentally. The lasing performance of VECSELs based on CVD diamond, electroplated copper substrate and electroplated gold substrates are compared in section 2.7.1. In section 2.7.2, we optimize the lasing performance of the VECSEL with electrodeposited copper substrate by changing the operation temperature and the coupling mirror transmission. In section 2.7.3, we compare the thermal characteristics and the lasing performances of VECSELs with electroplated and bulk copper substrates, in order to check if the electrodeposited copper has a similar thermal impendence as that of bulk copper.

2.7.1 Evaluation of electroplated copper substrate

The VECSEL is tested in a simple plane-concave cavity configuration as it is presented in Fig. 2.22. The chip is mounted onto a copper heatsink to control the temperature of the device with a water cooling system, see in Fig. 2.24 (b). The chip is pumped with a continuous wave (CW) fiber-coupled 980 nm multimode laser diode delivering up to 8 W focused on approximately a ~100 μm diameter spot with incidence angle of 45°. The high power multimode pump is used to evaluate the ultimate

performance of the VECSELs. The external cavity is formed by the VECSEL chip and a concave dielectric mirror with reflectivity of 99 % at 1550 nm and curvature radius of 25 mm. The overall cavity length is around 25 mm.
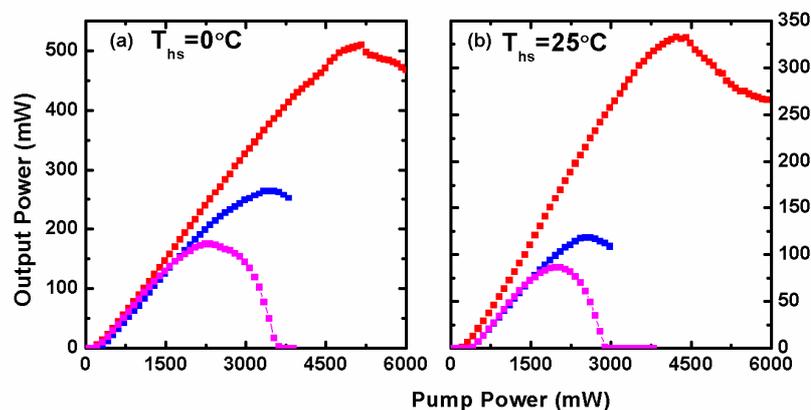
Figure 2.26 Continuous-wave emitted power of VECSELs with different host substrates. CVD diamond (red square), electroplated copper (blue square) and electroplated gold (magenta square) versus incident pump power at different temperatures.(a) Heatsink temperature is fixed at 0 °C. (b) Heatsink temperature is fixed at 25 °C.

Fig. 2.26 compares the lasing performance of VECSELs with CVD diamond, electroplated copper, and electroplated gold substrates. Continuous-wave lasing operation at 1.55 μm has been achieved. Fig 2.26(a) shows the output power of the OP- VECSELs versus focused pump power (L-P curves) at a fixed heatsink temperature of 0 °C with the water cooling system. Output power up to 510 mW is achieved from the VECSEL with CVD diamond based VECSEL before thermal roll-over occurs, while gold-based VECSEL has the lowest maximum output power (~170 mW). Intermediate output power around 260 mW is obtained from the copper-based VECSEL. The highest output power obtained from the electroplated-Cu VECSEL is of 120 mW at T= 25 °C as shown in Fig 2.26(b). The intermediate lasing performance of VECSEL with copper substrate is consistent with the conclusions from thermal modeling in Fig. 2.12.

For electroplated-Cu VECSEL, the central wavelength at CW lasing operation is obtained around 1.56 μm with a red shift ~ 0.3 nm.K^{-1} when the heatsink temperature is varied from 0°C to 25°C, see in Fig. 2.27 (a). For a constant heatsink temperature and

increasing pump power like in Fig. 4(b), the observed red shift of the center wavelength can be estimated to be ~ 0.35 nm.W^{-1}. These values demonstrate that this electroplated-Cu VECSEL can operate over a wide temperature range.
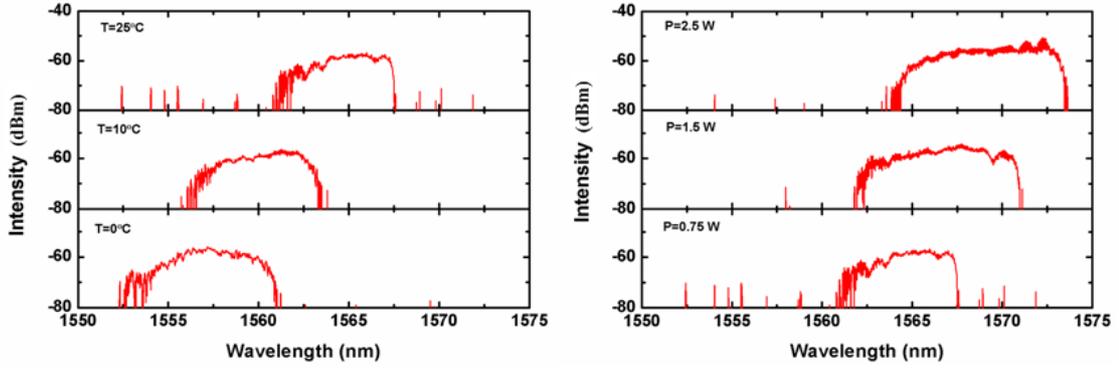
Figure 2.27 Lasing spectrum of electroplated-Cu VECSEL. (a) Optical spectra observed at different heat-sink temperatures. Pump power at 980 nm is kept at the value of 0.75 W for all measurements. (b) Optical spectra observed at different pump powers. Heat-sink temperature is fixed to 25°C for all measurements.

2.7.2 Lasing performance optimization

In this section, a single mode pump at 980 nm (615 mW output power) was used. The VECSEL chip with electroplated copper is mounted on the heatsink with thermal grease, and the two stages peltier cooling system is used to control the temperature.

2.7.2.1 Operating temperature

The output power achieved in CW operation for different heatsink temperatures are plotted in Fig. 2.28. The slope efficiency defined as $\eta = \dfrac{\Delta P_{laser}}{\Delta P_{pump}}$ is found to be of 27.6%, 24.3%, and 18.1% for a temperature of the heatsink 0 10 and 25 respectively. The slope efficiency is reduced by a factor of 9% when the heatsink temperature is changed from 0 to 25 . The slight reduction in the slope efficiency is consistent with the increased carrier leakage out of the QWs and the increased nonradiative recombination. We noticed that the rollover point (where output power started to decay) is reached for

59

the three temperatures, and this limit the maximum output power of the laser. Operating the laser as cool as possible is preferred in order to increase the output power.
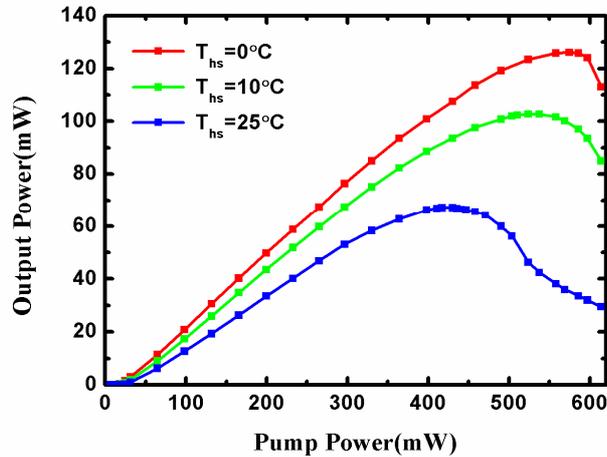
Figure 2.28 CW L-P curves of VECSEL with electroplated copper substrate versus focused pump power for heatsink temperature of 0°C(red), 10°C (green) and 25 °C (blue) in the plane concave cavity with a 99% reflectivity concave mirror (and ROC=15 mm).

2.7.2.2 Coupling mirror
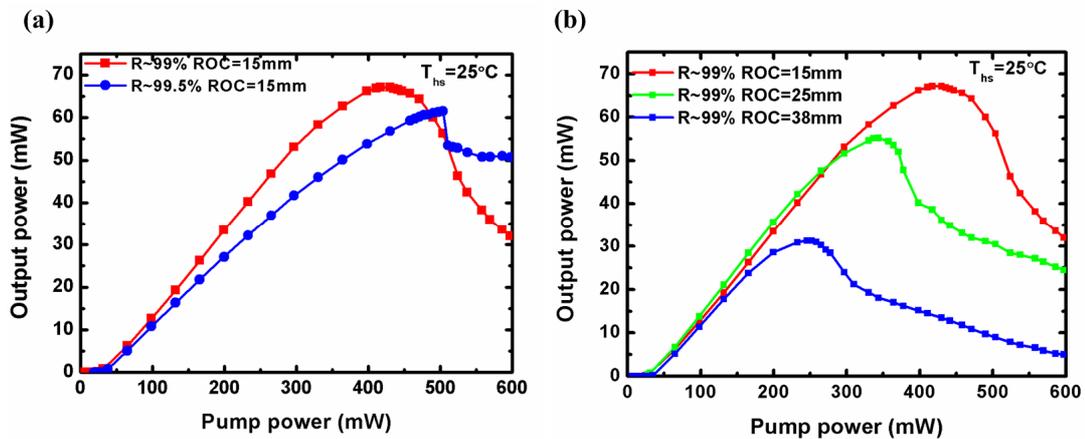
Figure 2.29 CW L-P curve of VECSELs with electroplated copper substrates versus pump power for heatsink temperature of 25°C in the plane concave cavity with (a) different reflectivity: 99% (red square) and 99.5 % (blue sircles) of a concave mirror with ROC=15 mm;(b) 99% reflectivity concave mirror of ROC=15mm (red), 25mm (green) and 38mm(blue).

Besides the operating temperature of the VECSEL chip, the characteristics of the output coupling mirror also affect the laser performance.

60

The first parameter impacting on the VECSEL output power is the mirror reflection (transmission) coefficient. Two different output coupler mirrors with reflection coefficient of 99% and 99.5% were tested, and the slope efficiency, rollover position and maximum output power were measured as shown in Fig. 2.28(a). The curves show that the slope efficiency is related to the output coupler transmission. The higher cavity loss due to the higher output coupler transmission requires a higher gain, which in turn requires a higher carrier density in the QWs and, as a side effect, higher pump power is required. The highest output power was obtained with a 99% output coupler reflection, so this was used in the next experiments.

A second parameter impacting on the L-P curve is the radius of curvature (R_{oc}) of the coupling mirror. The optimum overlap between pump spot and laser mode can be changed by using the coupler mirrors with different R_{oc}, and therefore the thermal loading in OP-VECSEL is modified. When using coupler mirror with R_{oc} of ~ 15mm, the thermal rollover position of laser was postponed and maximum output power was obtained, as shown in Figure 2.28(b).

2.7.3 Comparison between electroplated copper and bulk copper plate

2.7.3.1 Thermal resistance

The thermal conductivity of electroplated metals may vary depending on the porosity or grain size in the electrodeposited layer, and it may differ from the bulk value. In order to further evaluate the thermal performance of the electroplated copper substrate, we compared the thermal and lasing performances of VECSEL with electroplated copper substrate to the ones of VECSEL with a bonded (via $AuIn_2$) bulk copper plate. First, the thermal resistance of the VECSEL chip has been estimated following the method used for electrically-pumped or optically-pumped VECSELs [35].

A fiber-coupled single-mode 980-nm laser diode is used as the optical pump source. It is preferred to the multimode pump because of its better stability and controllability of

the pump spot size. The average pump radius is estimated to be 30±5 µm. A typical value of 65% of the focused power is estimated to be absorbed in the structure in the measurements. The wavelength shift of a PL peak measured as a function of temperature, and as a function of absorbed pump power is plotted in Fig. 2.30 for both VECSELs with electroplated copper and bulk copper substrates.

As can be seen from the left-hand side of the figure, the wavelength shift versus temperature is linear for both structures. It can be fitted to be 0.14±0.015 nm/K for the structure with electroplated copper host substrate, and 0.13±0.01 nm/K for the one with bonded bulk copper substrate. The wavelength shift with temperature and the wavelength shift with pump power are related through the thermal resistance, following the equation [14,35]:

$$\left.\frac{\partial \lambda}{\partial P}\right|_{T=cst} = \left.\frac{\partial \lambda}{\partial T}\right|_{P=cst} \times R_{th} \tag{2.40}$$

where λ corresponds to the half-cavity mode peak, T is the temperature, R_{th} is the thermal resistance, and P is the absorbed pump power.
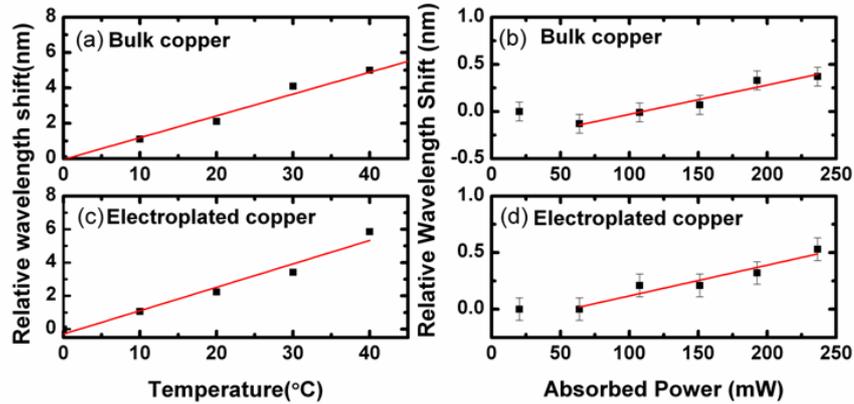
Figure 2.30 Relative wavelength shift of PL peak measured as a function of heatsink temperature at low pump power (left), and as a function of absorbed pump power at constant heatsink temperature (right) for both VECSELs with different host substrates: bonded bulk copper and electroplated copper.

As for the wavelength shift with increasing absorbed pump power at a fixed heatsink temperature of 25°C, a blueshift can be observed for the first two points in Fig. 2.30 (b)

and Fig. 2.30 (d). This behavior can be attributed to plasma effect competing with the thermal redshift at low carrier injection as discussed in Ref. 14. When the absorbed power is increased, the thermal red-shift dominates. The first points of the $\Delta\lambda(P)$ curves have been neglected. The thermal resistance is estimated accordingly for the two types of VECSELs, and is found to be of 50±3 K/W and 43±4 K/W for bonded bulk copper and electroplated copper based VECSELs respectively. The two comparable values indicate the similar thermal performances of bonded bulk copper and electroplated copper host substrates. Moreover, they are close to the value of ~ 42 K/W predicted by the thermal modeling for a VECSEL with 150-µm thick copper substrate and a pump radius of 30 µm.

2.7.3.2 Lasing Performance

The ultimate lasing performances of the two kinds of devices have been compared in a second step. The 980 nm single-mode pump laser is used with a focused pump radius of ~30 µm, and the plane-concave cavity is assembled with an output coupling mirror with ROC = 15 mm and R ~ 99 %. This configuration allows us to optimize the mode overlap between the fundamental mode of the cavity and the pump spot.
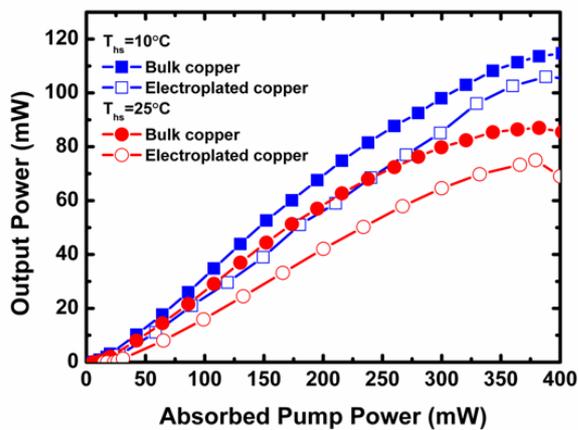
Figure 2.31 CW L-P curve of VECSELs with bonded bulk copper and electroplated copper substrates versus absorbed pump power for heatsink temperature of 10 °C (open and plain squares) and 25 °C (open and plain circles) in the plane concave cavity with a 99% reflectivity concave mirror (and ROC=15 mm).

The CW L-P curves of the two copper-based VECSELs obtained at different heatsink temperatures are reported in Fig. 2.31. The absorbed pump power is deduced from measurements of the reflected power as a function of the incident focused power. The optical spectra measured at various pump powers above lasing threshold for a heatsink temperature of 10 °C are reported in Fig. 2.32 for the VECSEL with electroplated copper substrate. The laser emission is longitudinal multimode, with a central wavelength close to 1.56 μm. The output beam profile (close to TEM0,0) recorded at maximum output power is also shown in the figure. Similar results have been achieved with VECSEL with bonded bulk copper substrate. The maximum output power of the VECSEL with electroplated copper substrate is of 75 mW when the heatsink temperature is kept at 25°C. The VECSEL with bonded bulk copper shows a slightly better lasing performance with a maximum output power of 85 mW at the same temperature. The roll-over of both VECSELs appear at a similar absorbed pump power value of ~400 mW. The external quantum efficiency defined as $\eta_{ext} = \dfrac{h\upsilon_{pump}}{h\upsilon_{laser}} \times \dfrac{\Delta P_{laser}}{\Delta P_{pump}}$ is obtained for the electroplated copper VECSEL with the heatsink temperature kept at 25 °C is of 35% and (slope efficiency ~22 %). Up to 106 mW CW output power is measured for a heatsink temperature of 10 °C and 390 mW absorbed pump power. This is obtained in combination with a high external quantum efficiency of 43% (slope efficiency ~27%). Compared to the lower slope efficiency of multimode pumped VECSELs shown in Fig. 2.26, these results are obtained owing to a good matching between the pump beam radius and the cavity mode waist. Even larger output power may be expected with an output coupling mirror having a slightly larger transmission.
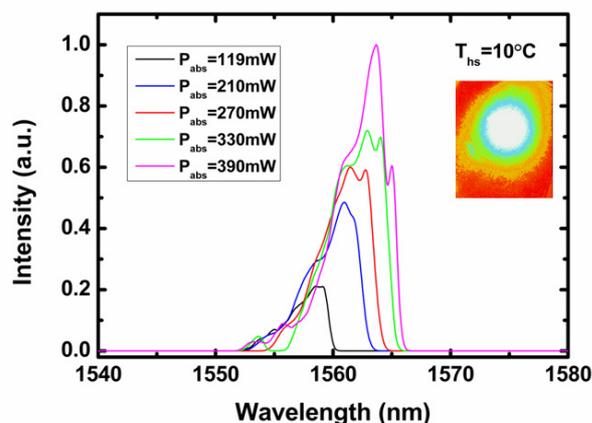
Figure 2.32 Laser spectra of VECSEL with electroplated copper substrate at various absorbed pump power for heatsink temperature of 10 °C. The inset shows the intensity profile of the output beam at an absorbed pump power of 390 mW.

2.8 CONCLUSION

In this chapter, we have studied the possibility of obtaining a high output power emission around 1550 nm from an optically pumped VECSEL. First, we have introduced a commonly used method for modeling the multilayer structure of VECSELs. We have investigated the influence of thickness of the top phase layer and antireflection coating on the microcavity resonance. The microcavity mode should be positioned at the maximum of gain spectrum. The increasing temperature in the active region shifts the wavelength of maximum gain away from the resonant cavity mode, and thus depresses the laser output power. It is therefore important to minimize the temperature rising. We have investigated the influence of the thermal impedance of DBR mirror and the host substrate with CoMsoL simulations. The thermal conductivity of both the bottom mirror and substrate are of paramount importance and should be optimized to dissipate efficiently the heat generated in the active region. We have combined the InP-based active region to a hybrid metal-GaAs/AlGaAs Bragg mirror using metamorphic and wafer-fusion approaches. We have then compared the thermal behavior of CVD diamond, copper and gold used as host substrates. VECSELs with a CVD diamond substrate have the best overall performance

65

and are promising for very large output power. On the other hand, VECSELs with copper substrate lead to better performances than gold based VECSELs, and are promising low-cost alternative to the diamond based VECSELs.

2.9 REFERENCE

[1] M. Kuznetsov, F. Hakimi, R. Sprague, and A. Mooradian, "High-power (>0.5-W CW) diode-pumped vertical external-cavity surface-emitting semiconductor lasers with circular TEM00 beams." IEEE Photon. Technol. Lett.,vol. 9, pp. 1063–1065, 1997.

[2] M. Kuznetsov, F. Hakimi, R. Sprague, and A. Mooradian, "Design and characteristics of high-power (>0.5-W CW) diode-pumped vertical external-cavity surface-emitting semiconductor lasers with circular TEM00 beams." IEEE J. Sel. Top. Quantum Electron., vol. 5, pp. 561–573, 1999.

[3] B. Rudin, A. Rutz, M. Hoffmann, D. J. H. C. Maas, A.-R. Bellancourt, E.Gini, T. Südmeyer, and U. Keller, "Highly efficient optically pumped vertical emitting semiconductor laser with more than 20-W average output power in a fundamental transverse mode," Opt. Lett., vol. 33, pp.2719-2721, 2008.

[4] M. Kuznetsov, VECSEL Semiconductor Lasers: A Path to High-Power, Quality Beam, and UV to IR Wavelength by Design, Wiley-VCH, 2010.

[5] P. Yeh, Optical Waves in Layered Media, Wiley, New York,1988.

[6] Heavens, Optical Properties of Thin Films , Dover, New York, 1965.

[7] A. C. Tropper and S. Hoogland, "Extended cavity surface-emitting semiconductor lasers," Progress in Quantum Electronics, vol. 30, pp. 1-43, 2006.

[8] C. Hirlimann, "Pulsed Optics," in Femtosecond Laser Pulses: Principles and Experiments, New York: Springer Science+Business Media, Inc., 2005, pp. 25-56.

[9] M. Hoffmann, O. D. Sieber, D. J. H. C. Maas, V. J. Wittwer, M. Golling, T. Südmeyer, U. Keller, "Experimental verification of soliton-like pulse-shaping mechanisms in passively mode-locked VECSELs", Opt. Express , vol.18, pp.10143-10153, 2010.

[10] S. W. Corzine, R. S. Geels, J. W. Scott, R.-H. Yan, and L. A. Coldren, "Design of Fabry-Perot Suface-Emitting Lasers with a Periodic Gain Structure," IEEE J. Quant. Electr., vol. 25, pp. 1513-1524, 1989.

[11] Y.-Z. Huang, Z. Pan, and R.-H. Wu, "Analysis of the optical confinement factor in semiconductor lasers," J. Appl. Phys., vol. 79, pp. 3827-3830, 1996.

[12] H. Lindberg, A. Larsson, and M. Strassner, "Single-frequency operation of a high-power, long-wavelength semiconductor disk laser," Opt. Lett., vol. 30, no. 17, pp. 2260-2262, 2005

[13] E. S. Saarinen, J. Puustinen, A. Sirbu, A. Mereuta, A. Caliman, E. Kapon, and O. G. Okhotnikov, "Power-scalable 1.57 μm mode-locked semiconductor disk laser using wafer fusion", Opt. Lett. Vol. 34, no. 20, pp. 3139-3141, 2009

[14] J.-P. Tourrenc, S. Bouchoule, A. Khadour, J.-C. Harmand, J. Decobert, N. Lagay, X. Lafosse, I. Sagnes, L. Leroy, and J.-L. Oudar, "Thermal optimization of 1.55 μm OP-VECSEL with hybrid metal - metamorphic mirror for single-mode high power operation," Optical and Quantum Electronics, vol. 40, pp. 155-165, 2008

[15] A. Khadour, S. Bouchoule, J.-C. Harmand, J. Decobert, G. Aubin, and J.-L. Oudar, "Ultrashort pulse generation from 1.56 μm mode-locked VECSEL at room temperature", Opt. Exp., vol. 18, no. 19, pp. 199902-19913, 2010

[16] J. Lyytikäinen, J. Rautiainen, A. Sirbu, V. Iakovlev, A. Laakso, S. Ranta, M. Tavast, E. Kapon, and O. G. Okhotnikov, "High-Power 1.48- m Wafer-Fused Optically Pumped Semiconductor Disk Laser", IEEE photon. technol. Lett., vol.23, pp. 917-919, 2011.

[17] A. Kemp, G. Valentine, J. Hopkins, J. Hastie, "Thermal management in vertical-external-cavity surface-emitting lasers: finite-element analysis of a heatspreader approach," IEEE J. Quantum Electron., vol. 41, no. 2, pp. 148-155, 2005

[18] H. Lindberg, M. Strassner, E. Gerster, J. Bengtsson, and A. Larsson, "Thermal Management of Optically Pumped Long-Wavelength InP-Based Semiconductor Disk Lasers," IEEE J. Sel. Top. Quant. Electr., vol. 11, pp. 1126-1134, 2005.

[19] A. J. Kemp, J. M. Hopkins, A. J. Maclean, N. A. S. N. Schulz, M. A. R. M. Rattunde, J. A. W. J. Wagner, and D. A. B. D. Burns, "Thermal Management in 2.3-

68

μm Semiconductor Disk Lasers: A Finite Element Analysis," IEEE J. Quant. Electr., vol. 44, pp. 125-135, 2008.

[20] M. Osinski and W. Nakwaski, "Effective thermal conductivity analysis of 1.55 μm InGaAsP/InP vertical-cavity top-surface-emitting microlasers," Electron. Lett., vol. 29, pp. 1015– 1016, 1993.

[21] J. Piprek, T. Troger, B. Schroter, J. A. K. J. Kolodzey, and C. S. A. I. C. S. Ih, "Thermal conductivity reduction in GaAs-AlAs distributed Bragg reflectors," IEEE Photon. Technol. Lett., vol. 10, pp. 81-83, 1998.

[22] S. Adachi, "Lattice thermal resistivity of III-V compound alloys," J. Appl. Phys., vol. 54, pp. 1844-1848, 1983.

[23] M. Guden and J. Piprek, "Material parameters of quaternary III–V semiconductors for multilayer mirrors at 1.55 μm wavelength," Modelling Simul. Mater. Sci. Eng., pp. 349-357, 1996.

[24] W. J. Alford, T. D. Raymond, and A. A. Allerman, "High power and good beam quality at 980 nm from a vertical external-cavity surface-emitting laser," J. Opt. Soc. Am. B, vol. 19, pp. 663- 666, 2002.

[25] H. Lindberg, M. Strassner, E. Gerster, and A. Larsson, "0.8 W optically pumped vertical external cavity surface emitting laser operating CW at 1550 nm," Electron. Lett., vol. 40, pp. 601- 602, 2004.

[26] S. Lutgen, T. Albrecht, P. Brick, W. Reill, J. Luft, and W. Spath, "8-W high-efficiency continuous-wave semiconductor disk laser at 1000 nm," Appl. Phys. Lett., vol. 82, pp. 3620- 3622, 2003.

[27] F. van Loon, A. J. Kemp, A. J. Maclean, S. Calvez, J.-M. Hopkins, J. E. Hastie, M. D. Dawson, and D. Burns, "Intracavity diamond heatspreaders in lasers: the effects of birefringence," Opt. Express, vol. 14, pp. 9250-9260, 2006.

[28] J. Lyytikäinen, J. Rautiainen, L. Toikkanen, A. Sirbu, A. Mereuta, A. Caliman, E. Kapon, andO. G. Okhotnikov, "1.3- m optically-pumped semiconductor disk laser by wafer fusion," Opt. Express, vol. 17, no. 11, pp. 9047–9052, 2009.

[29] A. Caliman, A. Mereuta, G. Suruceanu, V. Iakovlev, A. Sirbu, and E. Kapon "8 mW fundamental mode output of wafer-fused VCSELs emitting in the 1550-nm band," Opt. Express, vol. 19, no. 18, pp. 16996–17001, 2011.

[30] M. Jacquemeta, M. Domenecha, J. Dionb, M. Strassnerb, G. Lucas-Leclina, P. Georgesa, I. Sagnesb and A. Garnachec, "Single-Frequency High-Power Continuous-Wave Oscillation at 1003 nm of an Optically Pumped Semiconductor Laser ", in Proc. of SPIE Photonics Europe, Strasbourg, France, April 2006

[31] R. Shau, M. Ortsiefer, J. Rosskopf, G. Bohm, F. Kohler, M.-C. Amann, "Vertical-cavity surface-emitting laser diodes at 1.55 mm with large output power and high operation temperature", Electronics Letters, vol. 37, no. 21,   pp. 1295-1296, 2001

[32] M. Ortsiefer, R. Shau, G. Bohm, M. Zigldrum, J. Rosskopf, M.-C. Amann, '90°C continuous-wave operation of 1.83-mm verticalcavity surface-emitting lasers', IEEE Photonics Technol. Lett., vol. 12, no. 11, pp. 1435-1437, 2000

[33]   W. Schwarzacher, "Electrodeposition: a technology for the future," The Electrochemical Society Interface, vol. 15, no. 1, pp. 32-33, 2006

[34] A. Kost, H. C. Lee, Y. Zou, P. D. Dapkus, and E. Garmire, "Band-edge absorption coefficients from photoluminescence in semiconductor multiple quantum wells," Appl. Phys. Lett., vol. 54, pp. 1356-1358, 1989.

[35] A. Bousseksou, S. Bouchoule, M. El Kurdi, M. Strassner, I. Sagnes, P. Crozat, J. Jacquet, "Fabrication and characterization of 1.55μm single transverse mode large diameter electrically pumped VECSEL", Opt. Quant. Electron. vol. 38, no. 15, pp. 1269-1278, 2006

Chapter 3 1.55 μm SESAMs

The development of semiconductor Saturable Absorber Mirrors (SESAMs) has been a key contribution to the generation of short pulses from ultrafast solid-state and semiconductor lasers [1, 2]. A SESAM consists of a stack of semiconductor layers grown by epitaxy, a technique allowing to control the layers composition and the layers thickness with sub-nanometer accuracy. SESAM structures can be epitaxially grown with a full control of their key design parameters- magnitude and phase of the optical absorption and reflection, adjustment of the saturation fluence (energy level where the device saturates). Moreover the carrier recovery time (how fast the absorber recovers) can be tuned down to the picosecond range by modifying the non-radiative recombination lifetime with an appropriate design or by the optimization of the growth conditions. The modulation depth (maximum nonlinear change in reflectivity), the non-saturable loss (amount of permanent loss of the device), the saturation fluence and the carrier recovery time are the main characteristics of a SESAM, further described in chapter 4, allowing to control the mode-locked pulse properties (pulse width, pulse chirp, etc) [3].

In this chapter, we will review the design and characterization of SESAM structures. In Section 3.1 the main properties of a semiconductor saturable absorber are presented and in Section 3.2 the general principle of the SESAM structure used in this PhD work is introduced. In Section 3.3 the experimental methods used for the optical characterization of SESAM are described. In Section 3.4, the fabricated SESAMs are presented in details, including the characterization results.

3.1 INTRODUCTION

3.1.1 SESAM structure

The evolution of the concept of the SESAM device is summarized in Fig. 3.1.
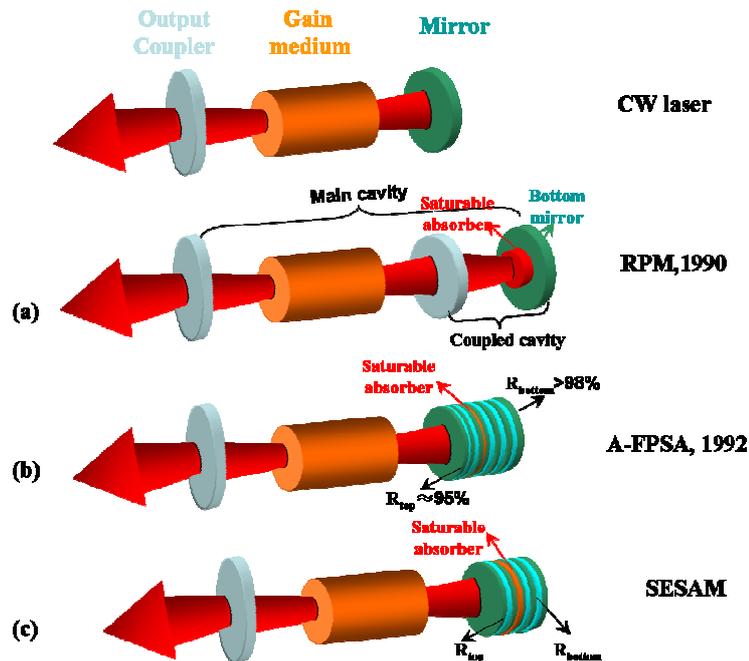
Figure. 3.1 Historical evolution of the SESAM design: (a) initially the semiconductor saturable absorber was used inside a nonlinear coupled cavity, termed resonant passive modelocking (RPM) ; (b) first intracavity saturable absorber leading to passive mode-locking from diode-pumped solid-state lasers without *Q*-switching instabilities: antiresonant Fabry–Perot saturable absorber (A-FPSA); (c) general concept of semiconductor saturable absorber mirror (SESAM) without any restrictions on the mirror design.[3]

The first SESAM was designed for resonant passive modelocking (RPM) as sketched in Fig. 3.1(a) [4]. The coupled cavity including the saturable absorber generates a rapid amplitude modulation that strongly induces mode locking. A monolithic version of the the coupled cavity used in RPM was an intracavity antiresonant Fabry–Pérot saturable absorber (A-FPSA) as shown schematically in Fig. 3.1(b). The device consisted of a monolithic Fabry–Perot microcavity filled with a saturable absorber, and the microcavity length was adjusted for anti-resonance at the lasing wavelength, so that the intensity in the cavity was substantially lower than the incident intensity. The first A-FPSA mirror was based on absorber layers (50 InGaAs/GaAs quantum wells grown on GaAs substrate at low temperature by molecular beam epitaxy (MBE)) sandwiched between the bottom AlAs/AlGaAs semiconductor (R_{bottom} = 98%) and the top SiO_2/TiO_2 dielectric Bragg mirror (R_{top} = 95%). With this first A-FPSA, U.keller and co-workers realized a stable

72

self-starting passive modelocked Nd:YLF laser generating 3.3 ps pulses at 1 μm at Bell Labs in 1992 [5]. The top reflector of the A-FPSA provides an adjustable parameter that determines the intensity of the stationary wave inside the SESAM F-P cavity and therefore the saturation fluence of the saturable absorber device. Thus, this design allowed for a large variation of absorber parameters by simply changing the absorber thickness and the top reflector. This resulted in the general concept of semiconductor saturable absorber mirror (SESAM) without any restrictions on the mirror design [3, 6], sketched in Fig. 3.1 (c).

Today, the typical structure of SESAM is a multi-layer stack which can be optimized depending on where exactly the saturable absorber material is placed inside this multi-layer system.

3.1.2 Material requirement

In order to be useful as a SESAM absorber, the active semiconductor material must fulfill several requirements.

First and most important is the short lifetime (picoseconds) of the excited carriers. In order to make the SESAM work with short pulses at high repetition rates, the equilibrium conditions in the absorbing layer have to be restored quickly after bleaching by a laser pulse. The bleaching is achieved by filling the available states in the conduction band with photogenerated carriers, which leads to a saturation of the absorption until these carriers recombine. For SESAMs, carrier recovery times around 250 ps and below are desired to achieve pulse durations in the range of a few picoseconds [1,3].
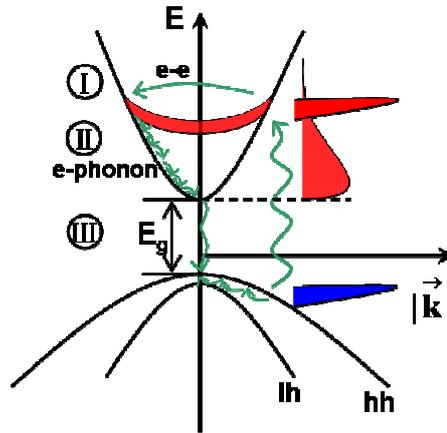
Figure 3.2 Schematic representation of the carrier dynamics in a bulk semiconductor material [7]. Three time scales can be distinguished. I. Coherent carrier dynamics, which at room temperature may last ~ few tens of femtoseconds depending on excitation density. II. Thermalization between the carriers due to carrier-carrier scattering and cooling to the lattice temperature by e-Phonon emission. III. Carrier-trapping or recombination.

Three major time scales of the carrier dynamics in III-V semiconductor materials are schematically illustrated in Fig. 3.2. When electron-hole pairs are generated, this excitation can be considered as an equivalent two-level system if the interaction between the carriers is neglected, which is a very rough assumption. The electromagnetic field of an ultrashort optical pulse generates a macroscopic polarization in a semiconductor. Carriers have well-defined phase relationships with each other and with the external field. Phases of the individual carriers are changed randomly within duration of 10-50 fs [8-10], which is referred to as the coherent regime (I) in Fig. 3.2. Then, carrier-carrier scattering sets in and leads to destruction of coherence and thermalization of the hot electron and hole due to the excitation of the carriers high in the conduction or valence band, it is referred to phase (II) in Fig. 3.2. This usually happens on a 60 - 100 fs time scale. On a 300 fs – 1 ps time scale, the hot carriers interact with the lattice mainly by emitting phonons. The carrier gas cools down to lattice temperature. After the thermalization and cooling processes, the carriers are at the bottom of the conduction and valence band, respectively [11-13]. The excited carriers vanish (III) by radiative transitions via the emission of photons or Auger processes at high carrier densities, on a nanosecond time-

scale. The excited carrier lifetime in a high quality III-V semiconductor is in excess of 1 ns, which is far too long for the application as a saturable absorber material. Fortunately, the carrier lifetime can be tuned over a large range of values from 100 fs – 30 ps, depending on the growth conditions and on the purity of the material. The carrier relaxtion time requirement of SESAM (<250 ps) can be achieved by using fast nonradiative recombination through deep level defects deliberately introduced into the material. Since fast carrier trapping is important in saturable absorbers used for passive mode-locking lasers, it is discussed in more details below.

Second, since SESAMs are intracavity elements, even small nonsaturable losses are undesirable, as they are enhanced strongly by its microcavity effect. The nonsaturable losses can result from the absorption related to the defects introduced by the nonradiative recombination centers. This means that SESAM fabrication technique should not change the nonsaturable loss too much when using fast nonradiative recombination with deep level defects. The techniques used for fast nonradiative recombination in SESAM, like low-temperature epitaxial growth (LTG), can achieve an ultrafast carrier recovery time, while resulting in large nonsaturable losses from the strong defect absorption [14]. The induced high nonsaturable loss will prevent the SESAM to be used in a mode-locked VECSEL. We review the techniques used to form nonradiative defects and their impact on nonsaturable loss.

3.1.3 Formation of nonradiative defects
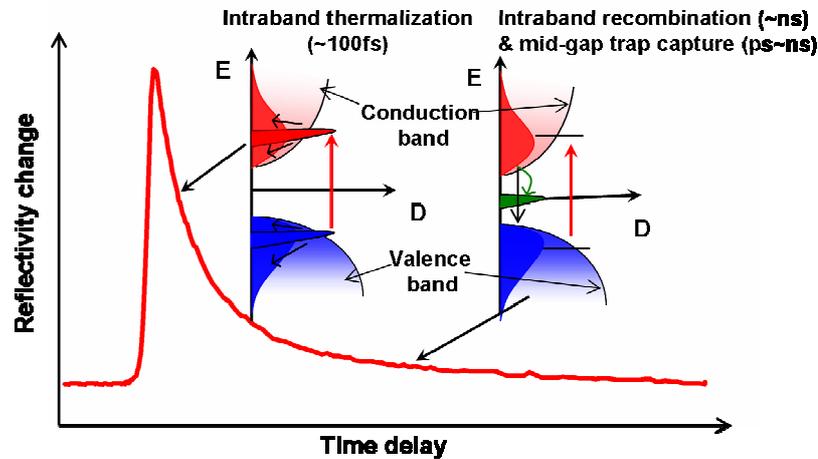
Figure 3.3 Carrier dynamics in SESAMs: Electrons are excited to the conduction band and thermalize on a time scale of 100 fs. The electrons then recombine or get trapped by defects on a time scale of 0.1 ps – 100 ps [3].

One way to speed up the recombination processes as shown in regime III in Fig. 3.2 is to incorporate a large density of deep level traps in a semiconductor [3]. Trapping of carriers into deep levels can proceed on sub-picosecond time scales as schematically shown in Fig. 3.3. In this figure, we distinguish the thermalization and the recombination at two different timescales; the carriers thermalize and form a thermal equilibrium on a 100-fs time scale, while carrier trapping proceeds on times scales from a few hundreds of femtoseconds to tens of picoseconds depending on the mobility of the carriers and the defect density. Higher defect densities give rise to faster trapping.

In order to generate mid-band gap defect-induced states in the absorber material, different approaches have been used including ion irradiation, deep impurity doping, low-temperature epitaxial growth (LTG), or a combination of doping and LTG.

(1) *Ion-irradiation*. Ion irradiation is a kind of ex-situ treatment. This technique consists in bombarding the semiconductor structure with ions of very high energies. Ions will thus pass through the active layer from one side and create defects throughout their passage. Many ions have been studied in the framework of the development of this technique. The use of light ions such as protons (H +) will create point defects [15], while

the use of heavy ions such as nickel (Ni^+) [16], gold (Au^+) or the oxygen (O^+) [17] will create many defects in the form of aggregates. Although both types of ions have been used to obtain relaxation times of a few picoseconds, the heavy ions give shorter recovery time and more created defects, and are less sensitive to temperature [18]. Finally, it should be noted that the exciton absorption, although slightly degraded, is still visible for radiation doses up to $1*10^{12}$ cm^{-2} [17]. Unfortunately, this technique has a significant effect on the reflectivity of the SESAM, which is due to the introduction of optical losses in the Bragg layers related to the irradiation step [19]. The reflectivity maybe reduced down to 98% that is 2% equivalent cavity losses, which is generally not adapted to VECSEL operation at 1.55 μm considering the available gain.

(2) *LTG*. Most of optoelectronic components based on semiconductor material require high structural quality, hence require to grow the semiconductor layers at typical temperatures of 500 ° C to 600 ° C for Molecular Beam Epitaxy (MBE) [20]. By decreasing the growth temperature, many microscopic structural defects appear (excess of As antisite as for example in GaAs) and form deep levels traps that capture the excited carriers [21]. Experience shows that the carrier relaxation time decreases with growth temperature. Thus sub-picosecond carrier relaxation times were achieved with quantum wells on GaAs [22-24] and on InP (but associated with doping) [25] for growth temperatures of 310 ° C and 200 ° C respectively.

(3) *Deep impurity doping*. This technique allows for the creation of non-radiative recombination centers during material growth. To date, two elements were mainly used to reduce the recovery time: beryllium (Be) and iron (Fe). Doping with Be is always associated with a low-temperature growth [25-26]. In addition to the defects associated with low growth temperature, the Be atoms form complexes with As in GaAs based materials which act as centers of capture and recombination of carriers. Doping with Fe is performed at a higher growth temperature (~ 450 ° C). The Fe atoms replace the In in the crystal lattice and thus form deep acceptor levels which will trap the carriers [27]. In both cases, the carrier relaxation time decreases with the doping density. The technique of Be

doping has allowed to achieve a relaxation time as short as 250 fs for GaAs / AlAs QWs (doping concentration of $2*10^{19}$ cm^{-3} and growth temperature of 280 ° C) [26] and 1 ps for InGaAs/InAlAs QWs (doping concentration of $7.8*10^{17}$ cm^{-3} and growth temperature of 200 ° C) [25]. The Fe doping technique has resulted in a recovery time of 290 fs for InGaAs / InP QWs (concentration of $2*10^{19}$ cm^{-3}) [28].

These techniques we have mentioned, allow to obtain recovery time short enough to obtain a passive mode locking with ultra short pulses (<250 ps). Unfortunately, the temporal response was accelerated at the expense of high nonsaturable losses preventing the SESAM to be used in a VECSEL cavity.

Within the last decade, dilute nitride alloys have attracted considerable interest due to their strong ability in decreasing the band gap of GaAs-based material [29-30]. It has also been early established that the addition of nitrogen (N) shortens the carrier lifetime of as-grown III-V alloys, due to the presence of traps and nonradiative centers. N. Härkönen *et al.* at Tampere University of Technology have studied the dynamics of a GaInNAs semiconductor saturable absorber mirror and have measured relaxation times of 30–40 ps for an as-grown structure with N compositions ranging from 1% to 3.5% [31]. In order to lower this time to a few picoseconds, additional recombination centers need to be introduced. However, a further increase of the N content in the QW would also result in a drastic change of its absorption characteristics: a redshift and a significant broadening of the absorption edge are observed.

In the previous PhD work by M. Le Du at LPN, it was shown that the use of very thin N-rich GaNAs layers (containing a high amount of nitrogen (N)) can be used in order to reduce the carrier recovery time [32]. These GaNAs layers are placed very close to the quantum well (a few nanometers) to enable carriers to be evacuated by the tunnel effect and then to recombine. The carrier relaxation time maybe adjusted by the thickness of the GaAs spacer separating the quantum well and GaAsN plane. This approach avoids the need for increasing too much the N-content in the quantum wells itself. It was used to fabricate microcavities with InGaNAs or InGaNAsSb quantum wells on GaAs substrates.

One of these structures operating at 1.55 microns has yielded a recovery time down to a few tens of picoseconds [33]. To reduce the recombination time, it is important to obtain a high concentration of nitrogen in the GaAsN recombination plane (~ 10%).

Among the techniques mentioned above, the use of nitrogen planes is a technique that induces less deterioration in the optical quality of the quantum wells and of the SESAM structure as a whole. The carrier recovery time may be controlled by the distance between the planes of nitrogen and the quantum wells, by the number of inserted planes, as well as by the nitrogen concentration in the planes. In addition we can hope to vary the recovery time from several tens of picoseconds to less than ten picoseconds. Moreover, the absorber is grown on a GaAs substrate, this allows us to grow broadband AlAs/GaAs Bragg mirror as the bottom mirror. In this thesis, we have followed this technique for the fabrication of SESAM operating at 1.55μm with fast carrier recovery time while maintaining a low non-saturated loss, as will be further detailed in section 3.4.

3.2 SESAM DESIGN

By varying the material composition and certain design parameters, the macroscopic parameters of a SESAM (in particular, the operation wavelength, the modulation depth, the saturation fluence, and the recovery time) can be tailored for operation in very different regimes [1, 3, 34].
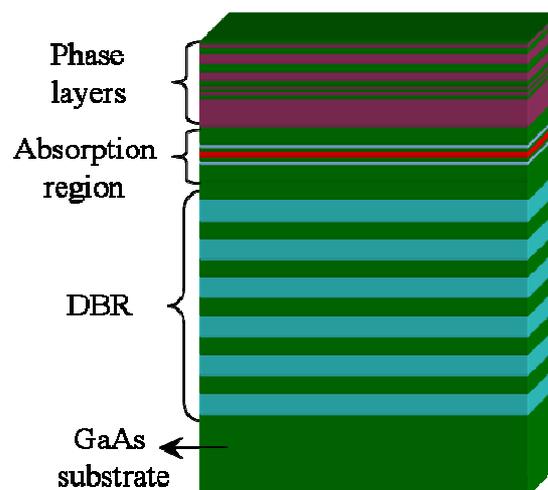
Figure 3.4 Schematic representation of a SESAM structure

Fig. 3.4 shows our SESAM structure. It contains a bottom Distributed Bragg reflector (DBR), a quantum well based absorption region, and a top phase layer used to tune the resonance of the device. In this section, we discuss the design of the SESAM structure. Fistly, the AlAs/GaAs DBR design is given. Then we present the InGaAsNSb/GaAs/GaAsN absorbing region. Finally, we discuss the microcavity design (which can be resonant or anti-resonant at lasing wavelength) and we show how this design impacts on the SESAM properties, such as the absorption enhancement factor (also referred to as the longitudinal confinement factor) and the group delay dispersion (GDD). The definition of both parameters has been previously explained in section 2.1.

3.2.1 DBRs

The DBR serves as the bottom high reflector. In our case, it consists of alternating quarter wave layers of low-index material (n_{AlAs} = 2.91 at 1550 nm) and a high-index material (n_{GaAs} = 3.37 at 1550 nm). As for the DBR in the VECSEL chip, its reflectivity is determined by the number of Bragg pairs, while the bandwidth depends on the difference in refractive index of the materials used. We used a 35-pair AlAs/GaAs DBR mirror to obtain a peak reflectivity above 99.9% with a broad bandwidth of ~145 nm at the center wavelength of 1550 nm. The measured reflectivity of an anti-resonant SESAM is shown in Fig. 3.5.
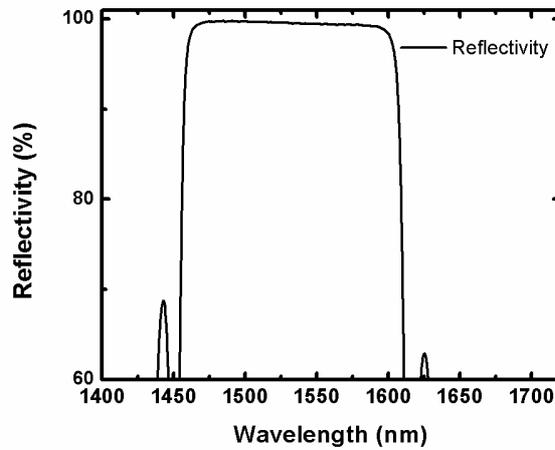
Figure 3.5 Measured reflectivity curves of an anti-reonant SESAM with a 35-pair AlAs/GaAs DBR

3.2.2 Absorbing QWs tunneling to fast recombination planes
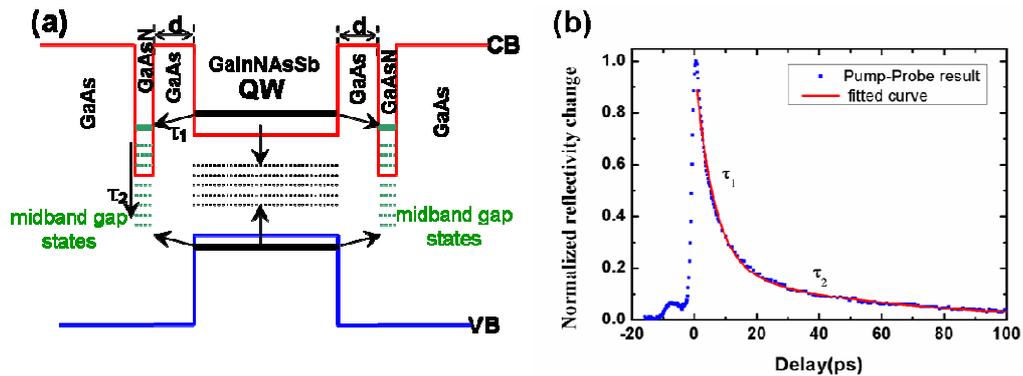
Figure 3.6 (a) Schematic representation of the saturable absorber: the QW is separated from GaAsN planes by ultra-thin tunnel layers.(b) Normalized time resolved reflectivity of a SESAM, the structure of which is shown in (a).

In this thesis, we employed very thin N-rich GaAsN layers placed ~2 nm away from the main absorbing QW as carrier trapping centers [32-33]. The carriers excited in the main QW are expected to tunnel through the thin GaAs barrier towards the N-rich GaAsN planes, where they are expected to recombine much more rapidly through the wide distribution of mid-band gap states as explained in Fig. 3.6.

Pump-probe measurements are performed to explore the carrier dynamics in such a structure. The time-resolved reflectivity measured at the probe wavelength is reported in

81

Fig. 3.6 (b) as function of the pump-probe delay, for a typical SESAM microcavity used in this PhD work. As shown in the figure, the curve can be fitted by a double-exponential decay with time constants τ_1 and τ_2. The first and faster decay corresponding to τ_1 is expected to be sensitive to the barrier thickness and lies in the range of few picoseconds. The carrier recombination rate is simply limited by the tunneling of the photoexcited carriers from the ground state of the GaInNAsSb QW to the GaAsN planes midgap states [33]. The origin of the slower decay time corresponding to the time constant τ_2 is considered to be dependent on the density of trap states available in the GaAsN planes. Increasing the N-content in the GaAsN planes enhances the density of defects and traps and in principle therefore reduces the value of τ_2. As a general conclusion, the overall absorption recovery time is tunable in such structures. It can be tuned by adjusting both the spacer thickness and the N content in the GaAsN planes.

3.2.3 Microcavity resonance

As there is a Fresnel reflection at the semiconductor–air interface, this together with the Bragg reflection leads to a microcavity effect (resonance effect). By the use of various top phase layers, the SESAM properties (in particular, the modulation depth, the saturation fluence, and GDD) can be tailored for operation in very different regimes. In this section, we compare the two extreme cases: resonant and anti-resonant configurations. We calculate and compare the amplitude of the absorption enhancement factor and the GDD values in both cases.

For these calculations, we employed the transfer matrix method discussed in chapter 2 and the refractive index of AlAs and GaAs are those given in section 2.1. For the InGaAsNSb QW based absorber, we used the complex refractive index n+ik according to the experimental data measured by M. Le Du [33]. The values of the extinction coefficient as a function of wavelength in the 1400 nm to 1700 nm spectral range are shown in Fig. 3.7. The refractive index value is fixed to n~ 3.61.
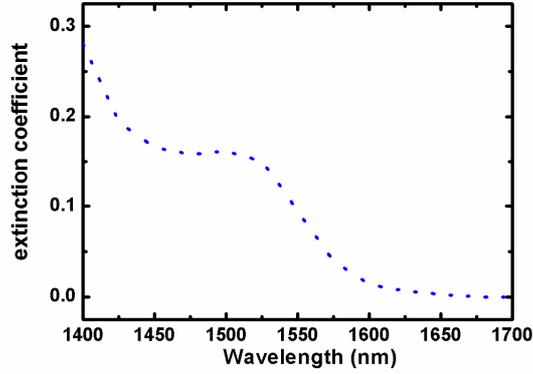
Figure 3.7 Extinction coefficient spectra of QW absorber in SESAMs

In most cases, the microcavity is designed to be antiresonant at the operation wavelength. The structure of an antiresonant SESAM is shown in Fig. 3.8 (a). It comprises a 35-pair DBR made of quarter wave pairs of AlAs and GaAs, and the absorber section consists of a single InGaNAsSb QW-layer embedded in GaAs. Fig. 3.8(a) shows the simulated standing wave pattern (in black) and the refractive index profile (in blue). The QW (in red) is placed at a node of the standing wave. Layers of GaAs are drawn in green, AlAs is blue. The simulated reflectivity and absorption enhancement factor of this antiresonant SESAM are plotted as a function of the wavelength in Fig. 3.8(b). The absorption enhancement factor for the SESAM $\Gamma_{abs}(\lambda)$ was calculated according to the definition of the longitudinal mode confinement factor as in VECSEL gain structures. The effective absorption is expressed as $\Gamma_{abs}(\lambda) \cdot \alpha_{QW}(\lambda)$. Where $\alpha_{QW}(\lambda)$ is the material absorption coefficient in the QWs.

Such devices exhibit a relatively broadband reflectivity, with a more or less constant absorption enhancement factor.
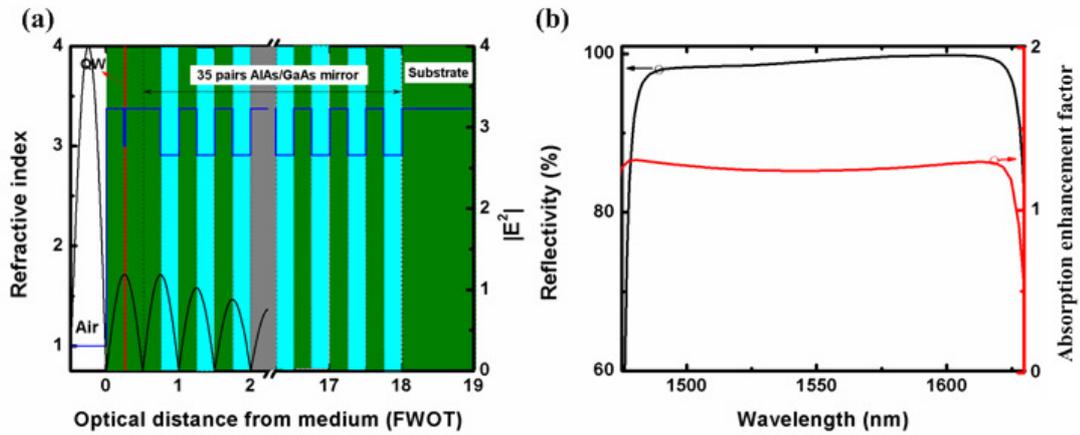
Fig 3.8 (a) Structure of an anti resonant SESAM. GaAs is in green, AlAs is in blue, while the gray is the break in the Bragg mirror; the material refractive index profile is in blue, and the normalized field intensity$|E^2|$ is plotted (black curve). (b) Linear reflectivity (black) and absorption enhancement factor (red) of the antiresonant SESAM as a function of the wavelength.

At the opposite of the antiresonant cavity, a resonant design of SESAM is shown in Figure 3.9(a). It has the same 35-pair AlAs/GaAs DBR and a single InGaNAsSb QW-layer embedded in GaAs as for the antiresonant SESAM, however there is an additional quarter-wavelength-thick GaAs layer on the top. Fig. 3.9(a) shows the simulated standing wave pattern in black and the refractive index profile in blue. GaAs layers are drawn in green, AlAs is in blue, and QW is in red. The simulated reflectivity and absorption enhancement factor of this resonant SESAM are plotted as a function of the wavelength in Fig. 3.9(b). As can be observed when comparing Figure 3.7 and Figure 3.8, there are big differences between the antiresonant and resonant configurations. In the case of Fig. 3.9(b), there are large variations in the reflectivity and absorption confinement factor curves around resonant wavelength. Compared with devices of antiresonant design, resonant design has a higher absorption enhancement factor.

84
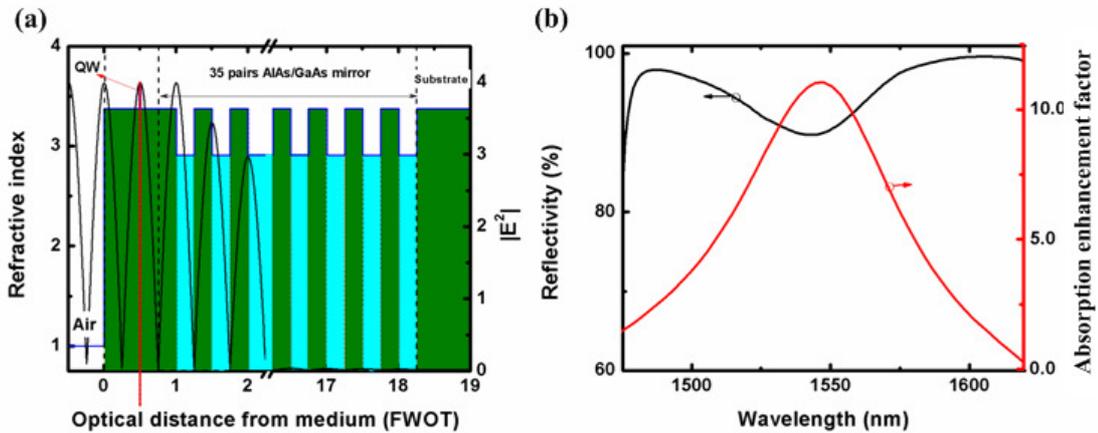
Figure 3.9 (a) Structure of a resonant SESAM. GaAs is in green, AlAs is in blue; the material refractive index profile is in blue, and the normalized field intensity|E^2| is plotted (black curve). (b) Linear reflectivity (black) and absorption confinement factor (red) of the resonant SESAM as a function of the wavelength.
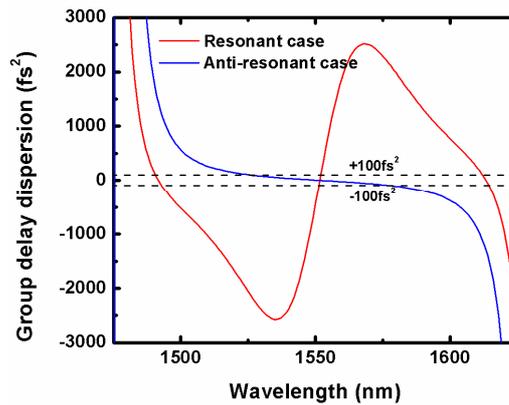
Figure 3.10 Comparison of wavelength-dependent GDD between antiresonant and resonant SESAMs.

The group delay dispersion (GDD) as a function wavelength can also be compared for the two SESAMs. Fig. 3.10 shows the calculated GDD, the blue curve corresponds to the antiresonant SESAM while the red to the resonant one. In the resonant case, the group delay dispersion varies from -2700 fs^2 to +2700 fs^2 in a short wavelength range from 1530 nm to 1570 nm. The antiresonant case exhibits a relatively broader wavelength range with a more or less constant and low group delay dispersion between +/-100fs^2 in the same 1530 - 1570 nm wavelength range.

From the comparison between these two extreme cases, we expect that it is possible to adapt the group delay dispersion in the SESAM by modifing the microcavity resonance.

3.3 SESAM CHARACTERIZATION

Section 3.2 has shown that different SESAM designs correspond to different reflectivity coefficients, group delay dispersion and absorption enhancement factors. In order to further characterize the SESAMs used in the passive mode-locking experiments, we have investigated both their linear and their nonlinear optical properties. The main parameters of a SESAM are the center operation wavelength λ_0, the modulation depth ΔR, the saturation fluence F_{sat}, the nonsaturable losses R_{ns} and the absorber recovery time τ [1, 3]. These parameters as well as the experimental methods to measure them, are introduced in this section.

3.3.1 Nonlinear reflectivity measurement

The nonlinear properties of a SESAM are characterized by the saturation fluence (Fsat), modulation depth (ΔR) as well as the nonsaturable losses (ΔRns). The nonlinear reflectivity of SESAM depends on these parameters. The saturation fluence can be seen as the pulse fluence for which saturation of the absorption starts. In most cases, it is desirable to keep this value low, to avoid the need for high intracavity power, or for tight focusing on the device SESAM surface in the laser cavity. The modulation depth indicates the difference in reflectivity between a fully saturated SESAM and the device in equilibrium state. The part that cannot be saturated is named nonsaturable loss, these losses serve no purpose, but reduce the efficiency of the laser and should be minimized.

3.3.1.1 Definition of nonlinear reflectivity
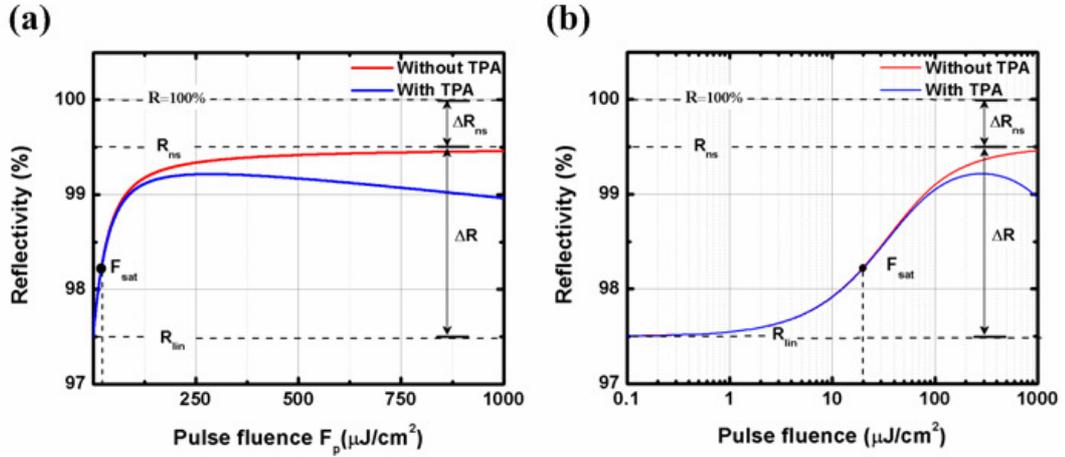
Figure 3.11 Nonlinear reflectivity R of a SESAM versus incident pulse energy fluence F_p. R_{lin}: linear reflectivity; R_{ns}: reflectivity with saturated absorption; ΔR: modulation depth; ΔR_{ns}: nonsaturable losses in reflectivity; F_{sat} : saturation fluence. The red curves show the fit functions without TPA absorption ($F_2 \to \infty$) while blue curves including TPA absorption. (a) linear scale. (b) logarithmic scale.

The typical nonlinear reflectivity R of a SESAM plotted as a function of the incident pulse energy fluence F_p, is shown in Fig. 3.11. In the following, it is assumed that the incident pulse duration is much shorter than the absorption recovery time, so that the reflectivity depends essentially on the pulse fluence rather than on its peak power. For an incident pulse with pulse energy E_p, the pulse fluence F_p is given by equation (3.1):

$$F_p = \frac{E_p}{A} \tag{3.1}$$

where A is the area of the focused beam on the SESAM.

For illustration, the same curve is plotted on a linear fluence scale (left) and a logarithmic scale (right). This curve is completely determined by three parameters: (i) the linear reflectivity R_{lin} for pulses with weak pulse energy fluence ($F_p \to 0$), (ii) the reflectivity R_{ns} for strong large pulse fluences ($F_p \to \infty$) when all saturable absorption is bleached, and (iii) the saturation fluence F_{sat}, described in detail later. In Fig. 3.11, a significant roll-over is observed at high pulse fluences, which is related to two-photon absorption (TPA) effect. The parameter F_2 is defined to take into account the contribution

of this effect to the nonlinear reflectivity of the SESAM. This effect is often referred to as inverse saturable absorption and seems to be the most important damage mechanism for SESAMs today.

The modulation depth ΔR in Fig. 3.11 is the maximum nonlinear change in reflectivity; it is given by equation (3.2):

$$\Delta R = R_{ns} - R_{lin} \tag{3.2}$$

The nonsaturable loss ΔR_{ns} refers to the amount of permanent loss of the device and are defined as:

$$\Delta R_{ns} = 100 - R_{ns} \tag{3.3}$$

The definitions above imply that R_{lin} and R_{ns} are not experimentally accessible but rather extrapolated values from the measured reflectivity using a proper model function.

Due to the saturation of the QW absorption, the SESAM reflectivity depends on the incident pulse fluence. With increasing pulse fluence the absorber saturates more strongly, leading to a higher reflectivity. By definition, the reflectivity for a pulse fluence $F_p = F_{sat}$ is increased by 1/e (37%) of ΔR with respect to R_{lin}, so that:

$$R(F_p = F_{sat}) = R_{lin} + \frac{1}{e} \cdot \Delta R \tag{3.4}$$

If the pulse fluence becomes too high ($F_p \gg F_{sat}$), the reflectivity decreases with increasing fluence according to a second order process such as two-photon absorption (TPA), leading to a rolloff in the reflectivity curve [35-36]. The parameter F_2 is defined as the fluence where the SESAM reflectivity has dropped by 37% (1/e) compared to R_{ns}. F_2 can be interpreted as the curvature of the rollover and is introduced as an additional parameter in the reflectivity function. For a flat-top shaped spatial beam profile, the nonlinear reflectivity can be expressed as [35, 37]:

$$R(F_p) = R_{ns} \cdot \frac{\ln[1 + \frac{R_{lin}}{R_{ns}}(e^{\frac{F_p}{F_{sat}}} - 1)]}{\frac{F_p}{F_{sat}}} \cdot e^{-\frac{F_p}{F_2}} \tag{3.5}$$

A microscopic definition of F_{sat} is given by

$$\frac{d\alpha}{dt} = -\frac{\alpha \cdot I}{F_{sat}}$$ (3.6)

where α is the absorption coefficient of absorbing material in the SESAM and where I is the incident pulse intensity. The temporal variation of the absorption coefficient α is inversely proportional to the saturation fluence F_{sat}. Equation (3.6) can be written in a more general way:

$$F_{sat} = \frac{h\upsilon}{2\sigma_{abs}}$$ (3.7)

where hυ is the photon energy and σ_{abs} is the effective absorption cross-section. σ_{abs} is an intrinsic parameter of the material, its value is typically ~10 times larger in quantum wells than in bulk materials. It is thus quite interesting to obtain 10 times lower saturation fluence from QW-based SESAM (compared to the bulk materials). The absorption coefficient of the material is given by:

$$\alpha = \sigma_{abs}N_D$$ (3.8)

where N_D is the density of states of the semiconductor.

If we now want to describe the nonlinear behavior of the SESAM when it is subject to pulses that are longer than the absorption recovery time, we need to introduce a new parameter which is the saturation intensity. This parameter is related to the saturation fluence in the following way. For a given photon energy hυ, saturation intensity I_{sat} depends on the effective absorption cross section σ_{abs} of the material, and the absorption recovery time τ_{abs} [38]:

$$I_{sat} = \frac{h\upsilon}{2\sigma_{abs} \cdot \tau_{abs}} = \frac{F_{sat}}{\tau_{abs}}$$ (3.9)

The saturation intensity I_{sat} is an important parameter, it determines how strong the saturation by a single pulse is, and it is one of the most important design parameters of a

passively mode-locked laser. Its value depends on both the saturation fluence of the absorber and the absorption recovery time.

3.3.1.2 Nonlinear reflectivity measurement setup
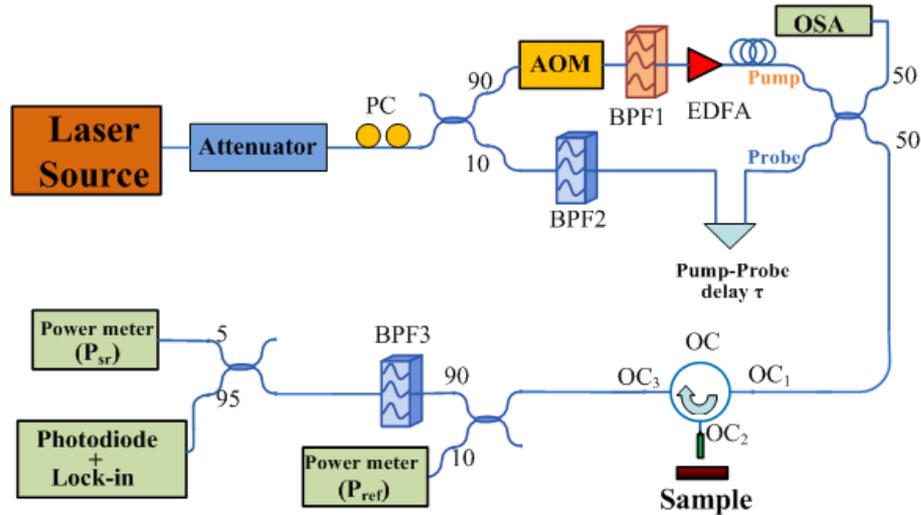
Figure 3.12 Schematic overview of the nonlinear reflectivity measurement setup. PC: Polarization Controller; AOM: Acoustic Modulator; BPF: Band Pass Filter; EDFA: Erbium Doped Fiber Amplifier; OSA: Optical Spectrum Analyzer; OC: Optical Circulator.

The saturation fluence of our SESAMs was measured with a fibered Pump-Probe setup, the development of which was started in the course of a previous postdoctoral work (H.-T. Nguyen). A schematic overview of the setup is shown in Fig. 3.12. The setup is based on fiber-optic technology, which simplifies the optical path design by eliminating the need to align optical elements. It is driven by a commercial pulsed fiber laser with sufficient pulse fluence (up to 500 μJ/cm^2), centered at 1550 nm and with pulse width of 1.5 ps. The pump and probe signals at two different wavelengths are obtained by employing band pass filters (BPF1 and BPF2) in two arms of the Mach-Zehnder interferometer. The pump signal is chopped at about 25 kHz by an acousto-optic modulator (AOM). By chopping the pump signal, we can measure directly the modulation that this signal induces on the reflectivity of the SESAM. The temporal overlap between pump and probe signals are adjusted with a delay line via a computer controlled translation stage. After coupling through a 2*2 fibered multiplexer, an optical

90

fiber carries the pump and probe signals into an optical circulator (OC). In one port of OC (OC2 in Fig. 3.12), a pigtailed collimator is used to focus the incident beam on the SESAM surface and to collect back the reflected beam. The radius of the beam focused on sample surface was measured to be ~4 μm. The reflected signal is directed into the detection unit through the port OC3, and after filtering out the pump signal (Bandpass filter BPF3), the reflected probe signal is detected with a lock-in amplifier.

In order to determine the saturation fluence of SESAM, we follow the method explained below:

(1) Adjust the intensity of the probe signal so that only the pump signal can saturate the sample, while ensuring enough signal to noise ratio at the lock-in amplifier;

(2) Adjust the delay line in the probe signal arm to obtain a perfect temporal overlap between pump and probe signal, and then delay line is fixed to this position during the experiment;

(3) Use a variable amplification stage consisting of an Erbium Doped Fiber Amplifier (EDFA) to access a pump pulse fluence range covering three orders of magnitude from 0.2 μJ/cm^2 to 100 μJ/cm^2. The relative reflectivity of the probe signal on the SESAM defined as $dR = R(F_p) - R_{lin}$ is measured as a function of the pump pulse fluence F_p. Since the pump pulses are relatively long (>1.5 ps) with a not very high peak intensity (I_p < 100 MW/cm^2), for the fit of the experimental curve, we neglect the contribution of F_2 ($F_2 \gg F_p$). Starting from equation (3.5), we use the following expression for fitting the measured relative reflectivity dR:

$$dR = \Delta R \cdot [1 - A \cdot \exp(-\frac{F_p}{F_{sat} \cdot B}) - \frac{1 - A}{1 + \dfrac{F_p}{F_{sat} \cdot C}}] \qquad (3.10)$$

A typical measurement of dR as a function of the incident pulse fluence and the corresponding fitting curve using equation (3.10) are shown in Fig. 3.13 for a resonant SESAM. It can be concluded that the modulation depth ΔR and the saturation fluence F_{sat} are 3.3% and 7 μJ/cm^2 respectively.
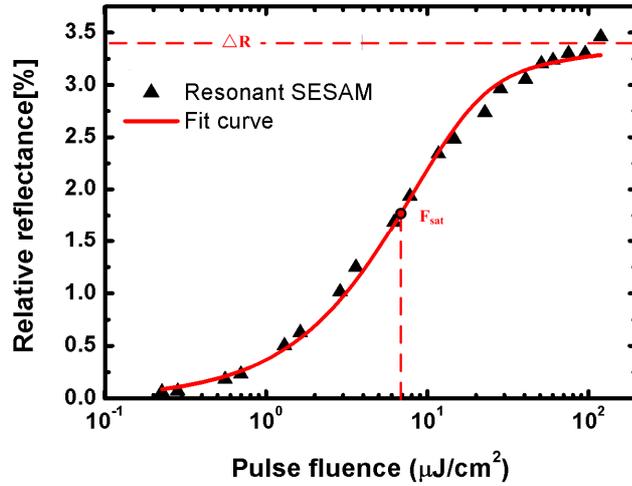
Figure 3.13 Relative reflectance of a resonant SESAM. The black triangles are the measurement, the red line is the fit. The red dash vertical line indicates the value of the saturation fluence F_{sat} and the red dash horizontal line indicates the modulation depth ΔR.

3.3.2 Measurement of τ_{abs}

As will be explained later in chapter 4, for modelocked VECSELs operating in the quasi-soliton regime [3], the carrier recovery time τ_{abs} of the SESAM plays a crucial role in the minimum achievable pulse duration. In order to obtain the shortest pulses, τ_{abs} needs to be as low as possible. It is thus important to measure this parameter which characterizes the SESAM dynamics. This has been done using the Pump-Probe measurement setup.

We used the same experiment setup shown in Fig. 3.12. Two key points of the measurement should be noticed: firstly, as for the measurement of F_{sat}, the pump signal and the probe signal should be controlled with an intensity ratio of at least ten to one, so that only the pump beam can saturate the sample. Secondly, the pump-probe delay (τ in Fig. 3.11) is varied using the variable delay stage and the relative reflectivity of the sample at the probe wavelength is recorded as a function of this delay. In case of a perfect temporal overlap ($\tau=0$), the pump has saturated the absorption in the SESAM to a certain amount, which is dependent on the incident pump fluence, and the amplitude of the reflected probe signal reaches its maximum value. When the pump-probe delay is

increased, the absorption in the SESAM starts to recover and the amplitude of the reflected probe signal is reduced. For a very long delay ($\tau > \tau_{abs}$), the absorption is fully recovered and the amplitude of the reflected probe signal reach a minimum value.

In the case of our QW-SESAMs with ultrathin tunnel layers, it is observed that the reflectivity decay occurs on two different time scales as already explained in section 3.2.2. Therefore, the relaxation dynamics of SESAMs can be described by a double exponential of the form

$$\Delta R(\tau) = A \cdot e^{-\tau/\tau 1} + B \cdot e^{-\tau/\tau 2} \tag{3.11}$$

Where τ_1 and τ_2 are the fast and slow time components of the relaxation and τ is the time delay between the pump and the probe beams. A, B describe the relative contribution of the two components to the reflectivity change. The fast recovery, described by τ_1, is due to transitions due to ultrathin tunnel layer, and the slow recovery, which is determined by τ_2, results mainly from carrier non-radiative recombination in the GaAsN planes.
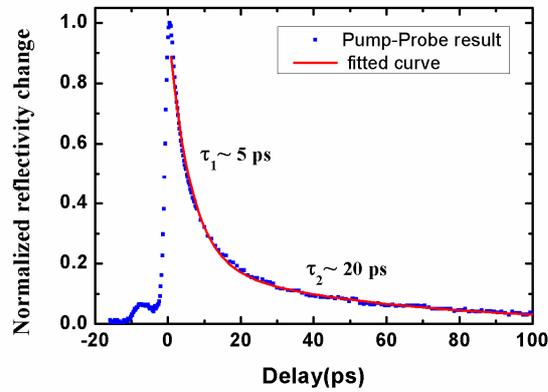

Figure 3.14 Normalized instantaneous reflectivity of a SESAM as function of the time delay between the pump and the probe pulse. The measurement is shown as blue dots, the solid red line is a fitting curve.

In Fig. 3.14, a typical data trace of a pump probe measurement is shown. The blue dots are the data, and a fit to the data according to Equation 3.11 is plotted in red.

3.4 FABRICATED SESAMS

The SESAM structures studied in this thesis must verify certain criteria: running around the wavelength of 1550 nm, a modulation depth sufficient to enable and stabilize the mode-locked regime. Therefore several structures were grown, and their nonlinear reflectivity and carrier recovery times were compared.

3.4.1 Fabricated structures

In this section, we present the fabricated SESAMs and the method used to tune the GDD and the modulation depth.

3.4.1.1 Absorbing region

The SESAM structures were grown by Molecular beam epitaxy (MBE) on a GaAs substrate and consisted of a 35-pair GaAs/AlAs Bragg mirror and a GaAs layer including the absorbing region. For the absorbing region, we used InGaNAsSb QW surrounded on one or both sides by one or more GaAsN fast recombination planes. Fig. 3.15 shows the structure of the absorbing region used in different fabricated SESAMs. Table 3.1 summarizes the main parameters of the different structures labeled as ACR54, ACR93 and ACR98.
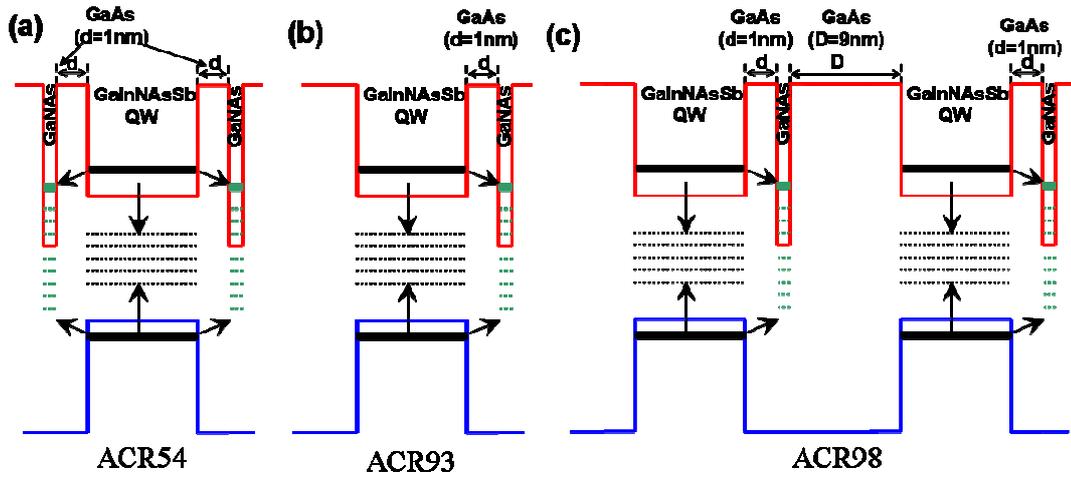
Figure 3.15 schematics of absorbing region in the SESAMs. (a). In the SESAM-ACR54, a quantum well surrounded by two GaNAs planes at a distance of 1 nm; (b). In the SESAM-ACR93, a quantum well surrounded by a single GaNAs plane at a distance of 1 nm; (c) In the SESAM-ACR98, two quantum wells, each one surrounded by a single GaNAs plane at a distance of 1 nm. The distance between the two QWs is 9 nm.

Table 3.1 Nominal thickness of layers in the absorbing region of the three SESAMs

		ACR54	ACR93	ACR98
		GaAs		
	InGaNAsSb	×	×	8
	GaAs	×	×	1
Nominal	GaAsN	1	×	1
thickness	GaAs	1	×	9
(nm)	GaInNAsSb	8	8	8
	GaAs	1	1	1
	GaAsN	1	1	1
		GaAs		
		DBR		

3.4.1.2 GDD-tuning layers

One approach to obain ultrashort pulses is to minimize the GDD in both the SESAM and VECSEL chips. M. Hoffmann at ETHZ in U. Keller's group have demonstrated

experimentally that the pulse duration strongly depends on the amount of total intra-cavity GDD in a passively mode-locking VECSEL [39]. In our case, the VECSEL chip forms a nearly resonant microcavity, as discussed in chapter 2, aiming at minimizing the VECSEL threshold. The VECSEL GDD is unknown but is expected to be far from zero due to this resonant design. Therefore the GDD of the SESAM has to be tuned and optimized to match the GDD value of the VECSEL chip to generate the shortest mode-locked pulses. In order to achieve this, we have applied the following practical method: we have added specific GaAs/AlGaAs top layers that could be selectively etched as schematically depicted in Fig. 3.16. By removing one or several of these layers, the microcavity resonance is modified (the microcavity could be tuned from resonant to antiresonant configuration at the wavelength of 1.55μm). As a consequence, the GDD value is also modified. The advantage of this design is that the carrier recovery time (another key parameter for short pulse generation) was kept constant during the tuning procedure. The exact design of these GDD-tuning layers is presented in the next paragraph.

3.4.1.2.1 GDD tuning layers design
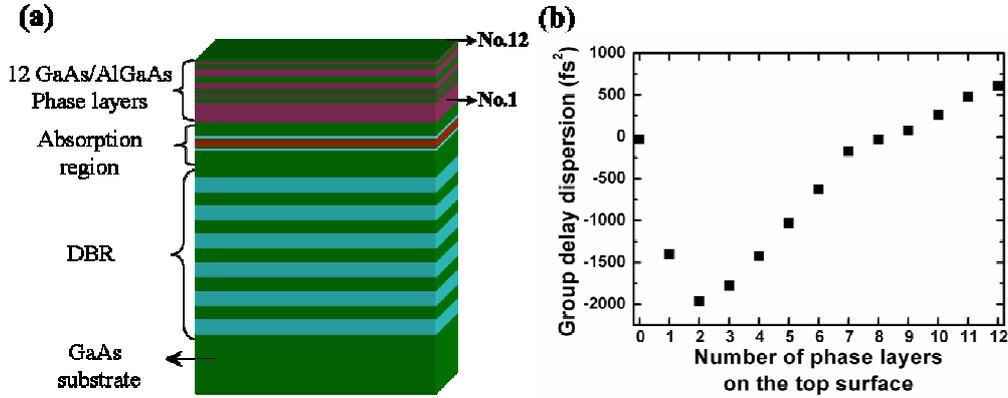
Figure 3.16 Illustration of the design of our GDD tuning layers above the absorption region of a SESAM. (a) Schematic overview of the whole structure of SESAM, top phase layers of GaAs and $Al_{0.7}Ga_{0.3}As$ were grown alternatively. (b) Calculated GDD of the SESAM as a function of the number of phase layers on top of absorbing region.

Table 3.2 Thickness of each phase layer and the induced GDD.

No of phase layer	Material	Thickness (nm)	GDD at 1550nm (fs^2)
1	$Al_{0.7}Ga_{0.3}As$	140	-1400
2	GaAs	9.1	-1960
3	$Al_{0.7}Ga_{0.3}As$	5	-1775
4	GaAs	5.5	-1425
5	$Al_{0.7}Ga_{0.3}As$	8	-1030
6	GaAs	10	-625
7	$Al_{0.7}Ga_{0.3}As$	35	-175
8	GaAs	31.9	-30
9	$Al_{0.7}Ga_{0.3}As$	40	76
10	GaAs	22.8	260
11	$Al_{0.7}Ga_{0.3}As$	15	480
12	GaAs	4.5	610

Fig. 3.16(a) shows the SESAM structure, 12 layers of GaAs and $Al_{0.7}Ga_{0.3}As$ were grown alternatively on the top of absorption region. With a judicious choice of the thicknesses of the successive GaAs/$Al_{0.7}Ga_{0.3}As$ phase layers, the SESAM can cover all

the cases from anti-resonant to resonant, with a controlled GDD value from -2000 fs^2 to +600 fs^2 at 1.55 μm. Fig. 3.16 (b) shows the calculated reflectance GDD curves as a function of the number of phase layers on top of absorbing region starting from an antiresonant SESAM. The thicknesses of the different layers are given in Table 3.2.

Starting from the as-grown SESAM chip (here we use ACR54 as an example) with a total of 12 phase layers on its top, the calculated GDD of ACR54 is ~ +610 fs^2 at 1.55 μm, as it can be deduced from Fig. 3.17. When removing the phase layers, the GDD value decreas step-by-step, see ACR54-3 (top 3 layers are removed) and ACR54-7 (top 7 layers removed) in Fig. 3.17. When we remove the top 10 layers, ACR54-10 has the minimum GDD. Then a slight increase in GDD value can be obtained with ACR54-11. When removing all the 12 phase layers, the SESAM ACR54-12 is antiresonant at 1.55 μm with low group delay dispersion in a large wavelength range as previously shown in Fig. 3.10.
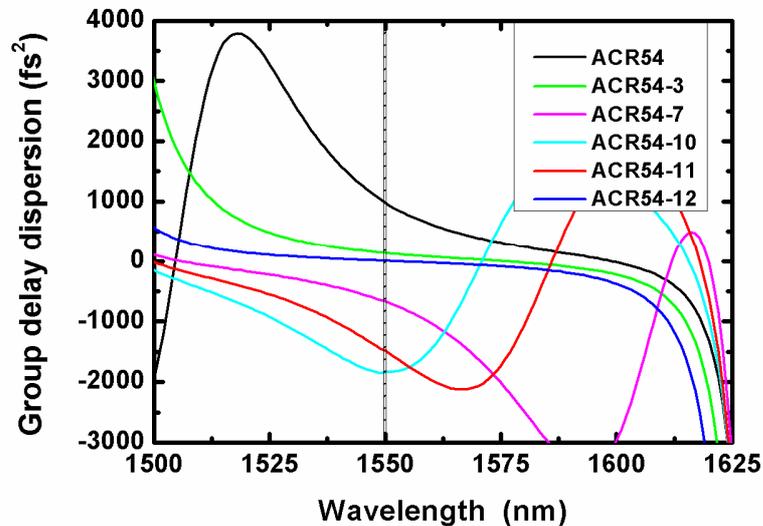

Figure 3.17 Calculated GDD as a function of wavelength for SESAM ACR54-n whose n phase layers were removed from the top.

3.4.1.2.2 Selective etching of the phase layers

Since dry-etching techniques do not offer sufficient selectivity in comparison to wet-etching, we rely on a wet-chemical procedure for the removal of GaAs and $Al_{0.7}Ga_{0.3}As$ phase layers alternatively. For this etch, a good selectivity is required to obtain optical grade surface roughnesses [40, 41].

The etching of $Al_{0.7}Ga_{0.3}As$ layers with a high Al content works by using a HF acid solution [40]. The Al is oxidized and alumina (Al_xO_y) is produced. The aluminium oxide reacts with the HF acid and generates soluble aluminium fluoride (AlF3) in the water. Although the solubility of aluminium fluoride (AlF3) is not very large, it allows for sufficient matter transport, enabling a reasonable etch rate in the order of a few hundred nanometers per minute. Due to the lower reduction potential of Ga in comparison to Al, Ga is not oxidized by a HF acid solution and thus does not become soluble. Thus, HF acid etches $Al_{0.7}Ga_{0.3}As$ but not GaAs, making it an excellent selective etchant for $Al_{0.7}Ga_{0.3}As$ layers. In order to obtain an etchant with the opposite selectivity, we use a solution based on citric acid and hydrogen peroxide (H_2O_2) [41]. In a first step, Ga is oxidized by the hydrogen peroxide (H_2O_2) component, which is a very strong oxidizing agent and thus capable of oxidizing Ga. This leads to a solubility of the oxidized Ga in the solution. Once the sample has been etched down to the $Al_{0.7}Ga_{0.3}As$ layer, Al is also oxidized by H_2O_2 and Al_2O_3 is produced. However, Al_2O_3 is not soluble in alkaline solutions. Thus, selectivity towards Al is obtained, making $Al_{0.7}Ga_{0.3}As$ an excellent etch stop for this process. We obtained good etching results and high selectivity for such a solution.

Fig. 3.18 shows optical microscopy images of a SESAM surface after selective etching of GaAs/AlGaAs layers. After removing the $Al_{0.7}Ga_{0.3}As$ layer on GaAs, a uniform surface is obtained as shown in Fig. 3.18 (a). When we use diluted HF solution to etch away the GaAs layer from the $Al_{0.7}Ga_{0.3}As$ layer, we can see some unwanted cylinders reserved on the surface in Fig. 3.18 (b). Fortunately, these cylinders can be removed by ultrasonic bath and we can obtain good surface during the selective etching.
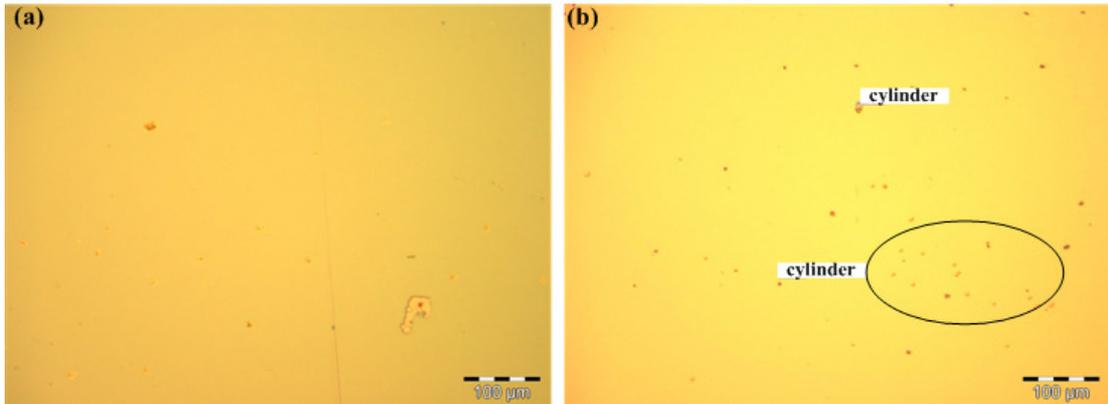
Figure 3.18 microscopy image of a SESAM structure after selective etching (a) GaAs surface after removing Al0.7Ga0.3As layer; (b) Al0.7Ga0.3As surface after removing GaAs layer.

3.4.1.3 Anti-reflection coating

Another approach to modify the GDD of the SESAM is to deposit an additional layer on the top surface. Starting from a SESAM chip with a nearly resonant design (and hence with a strong variation of the GDD around the resonance wavelength), the GDD value can be reduced, and its variation with wavelength can be optimized, by depositing a quarter wavelength layer acting as an antireflection (AR) coating. This can be obtained with a quarter wavelength layer of SiO_2 (n~1.46 at 1.55 μm). This is illustrated in Fig. 3.19 (a) where the calculated GDD of a resonant structure (solid curve) is compared to that of the same structure with an additional SiO_2 layer acting as an AR coating (dashed curve). With AR coating, a flatten GDD curve can be obtained over a larger wavelength range. Meanwhile, we also notice that the AR coating reduces the absorption enhancement factor of SESAM as shown in Fig. 3.19(b). The decrease in enhancement factor will lead to a smaller modulation depth ΔR and higher saturation fluence F_{sat} compared to the resonant structure.
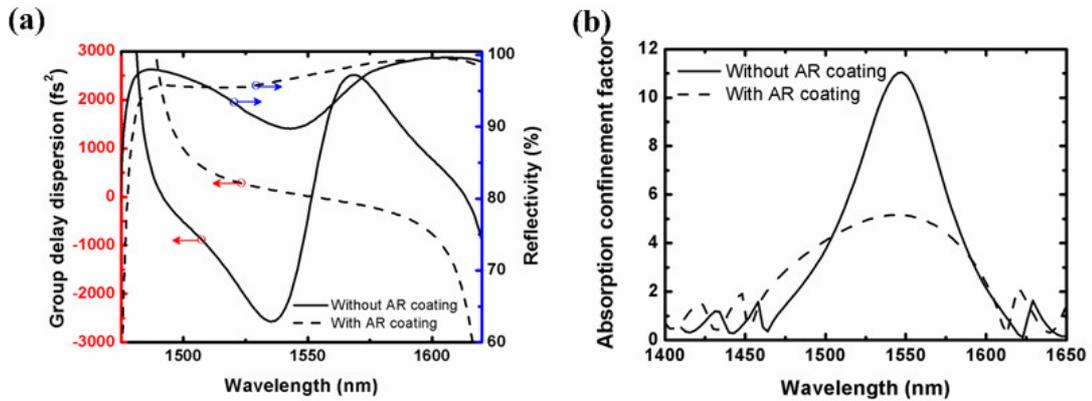
Figure 3.19 Difference in GDD, reflectivity and absorption confinement factor with and without AR-coating on a resonant SESAM. (a): the resonant SESAM (black solid lines) shows a steep slope in GDD (left axis) and an important contrast in reflectivity (right axis). The AR coated resonant SESAM (black dash lines) shows a flatten GDD curve, and a reflectivity curve with reduced contrast. (b): the resonant SESAM (black solid lines) shows an important contrast in absorption enhancement factor, while the AR coated resonant SESAM (black dash line) shows an absorption enhancement factor curve with reduced contrast.

We used plasma-enhanced chemical vapor deposition (PECVD) process to deposit the SiO_2 layer onto the SESAM chips. The optical thickness of the deposited layer was controlled with an accuracy of ~4%.

3.4.2 Characterization results

We have firstly measured the absorption recovery time for the SESAMs with the different absorbing regions: ACR54, ACR 93, and ACR 98 (described in table 3.1). The as grown SESAMs with 12 phase layers are approximately anti-resonant, therefore the amplitude of the relative reflectivity (dR) measured with the pump-probe setup is relatively weak. For this reason, an additional AR coating layer at 1550 nm was deposited on the surface to enhance the absorption prior to the measurement. A stronger reflectivity contrast could be obtained in this way. The pump-probe experiment results show the difference in carrier recovery dynamics of the three kinds of SESAMs. In the pump-probe experiment, the probe signal wavelength was centered at 1557 nm while the pump pulse fluence is kept at ~ 12 μJ/cm^2.
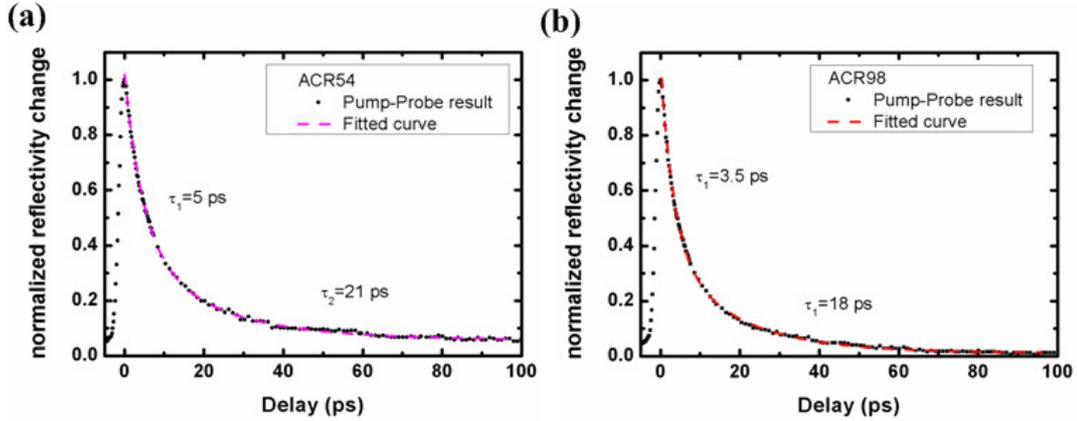
Figure 3.20 Reflectivity of a SESAM as function of the time delay between the pump and the probe pulse. (a)-ACR54: the pump-probe result (black circle), the fitted curve(magenta dash) according to Equation 3.11. (b)-ACR98: the pump-probe result (black square), the fitted curve(red dash) according to Equation 3.11.

Fig. 3.20 shows the experimental results fitted by a double exponential curve for the SESAMs ACR54 (Fig. 3.20(a)) and ACR98 (Fig. 3.20(b)). The fitted curves were obtained using Equation (3.11). The fast component of carrier recovery time τ_1 are of 5 ps and 3.5 ps for the SESAM ACR54 and ACR98, respectively. ACR98 has two InGaAsNSb QWs surrounded by 2 GaAsN planes and shows a faster carrier recovery time which is good to form shorter pulses in passive mode-locking. However, owing to the high absorption induced by the 2 QWs, the saturation fluence and the modulation depth were found to be much larger, and unfortunately no mode-locking operation could be obtained with this structure. From now on, we will therefore focus on the single QW SESAM ACR54 .

We also tried to measure the carrier recovery time of SESAM ACR93. Unfortunately, almost no absorption was observed for this structure at 1.55 μm-1.57 μm, and the reflectivity contrast was so weak that it could not be detected. It was concluded that the absorption bandedge of the QWs was shifted towards longer wavelength during the growth, the reason for this shift being unexplained.

We have achieved stable passive mode-locking from SESAM ACR54 with different configurations which we will review in details in chapter 4. Here we just present the

schematics and characterization results of two configurations named ACR54_A and ACR54_B. Starting from the SESAM ACR54-10 (top 10 layers removed), two methods were employed to achieve a SESAM configuration showing low unsaturable loss but still large enough modulation depth for mode-locking. In configuration of ACR54_A, a SiO2 layer (nominal thickness of 277 nm, and refractive index of ~1.46 at 1.56 µm), acting as a partial AR coating, was deposited by PECVD on the surface of the resonant SESAM. In configuration B named ACR54_B (also named ACR54-11), selective etching of one more phase layer was performed. The top phase layers of SESAMs ACR54-10, ACR54-A, ACR54-B, and ACR54-12 are described in Table 3.3.
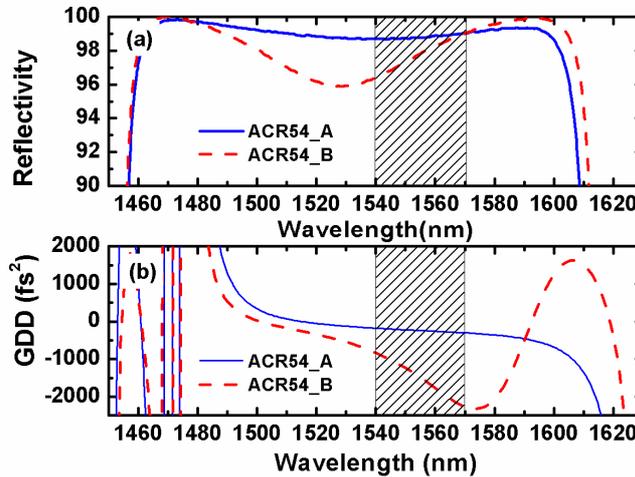
Figure 3.21 (a): Experimental reflectivity of ACR54-A SESAM (blue curve) and ACR54-B SESAM (red dash). (b): Corresponding calculated GDD value of the two SESAMs.

We firstly describe the ACR54-A and ACR54-B SESAMs. Their experimental reflectivity spectra and the corresponding GDD values (calculated with the transfer matrix model) are shown in Fig. 3.21. The grey area in Fig. 3.21 shows the wavelength region where stable mode-locking was obtained. The ACR54-A SESAM shows a flat-top reflectivity spectrum with a small reflectivity contrast indicating a relatively low modulation depth. The calculated GDD value was - 200 fs^2 with a variation of ±50 fs^2 in the operation region (grey area). For ACR54-B, the resonant wavelength was shifted to

1.52 µm. This detuned resonant configuration corresponded to a larger modulation depth and a GDD value of -2000 fs^2 at 1.56 µm.
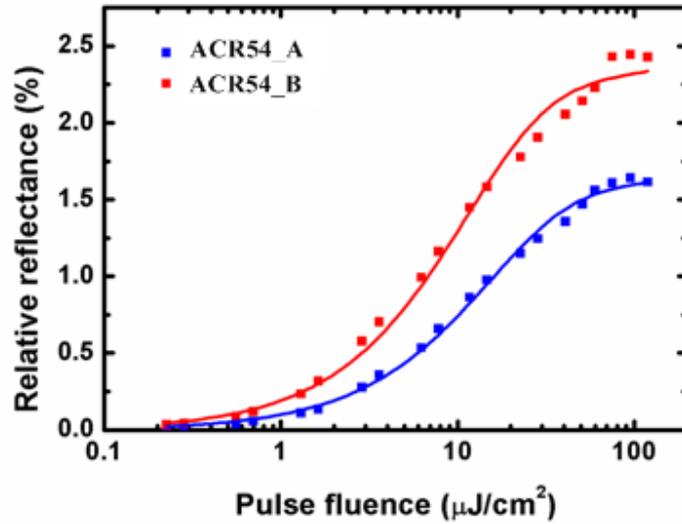
Figure 3.22 Measured nonlinear reflectivity of SESAMs ACR54_A (red squares) and ACR54_B (blue squares). The red and blue lines are the corresponding fitting curves.

Fig. 3.22 shows the experimental nonlinear reflectivity curve measured as a function of incident pulse fluence with the pump-probe set up, for SESAM ACR54_A and ACR54_B. The curves were obtained with the pump-probe system described earlier in this chapter. The resulting modulation depths ΔR and the saturation fluences F_{sat} are given in Table 3.3.

Table 3.3 Nominal thickness of top layers and measured nonlinear parameters of SESAM in the four configurations: Values in brackets are estimated from a transfer matrix calculation

		ACR54-10	ACR54_A	ACR54_B	ACR54-12
Layer Nominal thickness (nm)	SiO2	×	277	×	×
	GaAs	9.1	9.1	×	×
	Al$_{0.7}$GaAs	140.0	140.0	140.0	×
F_{sat}(µJ/cm^2)		7.2	13.7	10.1	(63)
ΔR (%)		3.4	1.6	2.4	(0.42)

The results indicate that ACR54_B is an intermediate case between the ACR54-10 and ACR54_A. ACR54_B SESAM shows a modulation depth between the two other values, while the saturation fluences are nearly at the same level of ~10 μJ/cm^2 for the three cases. ACR54-12 corresponds to an anti-resonant configuration, and the reflectivity contrast was so weak that it could not be measured with our set-up. This is due to the low absorption enhancement factor in anti-resonant configuration, as mentioned in section 3.2.4. We therefore give the estimated values (from transfer matrix method calculation) of F_{sat} and ΔR for the anti-resonant SESAM in the Table 3.3: a larger value of F_{sat} and a small ΔR is obtained compared to the three other cases.

3.5 CONCLUSION

We have fabricated SESAMs based on carrier scaling from a main absorbing QW towards GaAsN planes, which allows for tuning the carrier relaxation time down to the picosecond time scale. By adding additional layers on the top surface, we can modify the GDD value at the lasing wavelength. The absorption enhancement factor (and hence SESAM modulation depth) as well as the GDD can also be modified by adding an AR coating layer on the SESAM surface.

Three different epitaxial structures were fabricated. ACR98 with 2 QWs and 2 GaAsN fast recombination planes surrounding each QW shows the shortest absorption recovery time. Unfortunately, no mode-locked lasing was obtained with this SESAM in the VECSEL cavity, presumably due to a strong absorption from the 2 QWs. ACR93 with 1 QW and 1 GaAsN plane was discarded because the QW absorption was apparently shifted to a longer wavelength. Finally, ACR54, with 1 QW and 2 GaAsN planes was processed into different samples with different GDD tuning. We have presented four different configurations. The absorption recovery time was unchanged, while the GDD value (but also the modulation depth) was modified. The samples ACR54_10, ACR54_A, ACR54_B and ACR54_12, have been tested in passive mode-locking experiments, which are further described in the next chapter.

3.6 REFERENCES

[1] R. Paschotta and U. Keller, "Passive mode locking with slow saturable absorbers," Appl. Phys. B, vol.73, pp. 653-662 ,2001.

[2] U. Keller, " Ultrafast solid-state laser oscillators: a success story for the last 20 years with no end in sight," Appl. Phys. B, vol. 100, pp. 18-25, 2010.

[3] U. Keller and A. C. Tropper, "Passively modelocked surface-emitting semiconductor lasers," Physics Reports, vol. 429, pp. 67-120, 2006.

[4] U. Keller, W. H. Knox, and H. Roskos, "Coupled-cavity resonant passive mode-locked Ti:sapphire laser," Opt. Lett., vol. 15, pp. 1377-1379, 1990.

[5] U. Keller, D. A. B. Miller, G. D. Boyd, T. H. Chiu, J. F. Ferguson, and M. T. Asom, "Solid-state low-loss intracavity saturable absorber for Nd:YLF lasers: an antiresonant semiconductor Fabry - Perot saturable absorber," Opt. Lett., vol. 17, pp. 505-507, 1992.

[6] U. Keller, "Ultrafast All-Solide State Laser Technology," Appl. Phys. B, vol. 58, pp. 347-363, 1994.

[7] E. O. Goebel, "Ultrafast Spectroscopy of Semiconductors," in Advances in Solid State Physics, vol. 30, pp. 269- 294, 1990.

[8] J. L. Oudar, D. Hulin, A. Migus, A. Antonetti, and F. Alexandre, "Subpicosecond Spectral Hole Burning Due to Nonthermalized Photoexcited Carriers in GaAs," Phys. Rev. Lett., vol. 55, p. 2074, 1985.

[9] W. H. Knox, C. Hirlimann, D. A. B. Miller, J. Shah, D. S. Chemla, and C. V. Shank, "Femtosecond Excitation of Nonthermal Carrier Populations in GaAs Quantum Wells," Phys. Rev. Lett., vol. 56, p. 1191, 1986.

[10] J. Shah, Ultrafast spectroscopy of semiconductors and semiconductor nanostructures. Berlin: Springer-Verlag,1999.

[11] M. Gurioli, A. Vinattieri, J. Martinez-Pastor, and M. Colocci, "Exciton thermalization in quantum-well structures," Phys. Rev. B, vol. 50, p. 11817, 1994.

[12] M. Umlauff, J. Hoffmann, H. Kalt, W. Langbein, J. M. Hvam, M. Scholl, J. Söllner, M. Heuken, B. Jobst, and D. Hommel, "Direct observation of free-exciton thermalization in quantum-well structures," Phys. Rev. B, vol. 57, p. 1390, 1998.

[13] U. Keller, "Ultrafast solid-state lasers," in Laser Physics and Applications Subvolume B: Laser Systems, G. Herziger, et al., Eds., ed Berlin: Springer-Verlag, 2007, pp. 33-167.

[14] M. Haiml, U. Siegner, F. Morier-Genoud, U. Keller, M. Luysberg, R.C. Lutz, P. Specht, E.R.Weber, "Optical nonlinearity in low-temperature-grown GaAs: Microscopic limitations and optimization strategies " Appl. Phys. Lett. Vol. 74, pp. 3134-3136, 1999.

[15] K. F. Lamprecht, S. Juen, L. Palmetshofer, and R. A. Hopfel, "Ultrashort carrier lifetimes in H+ bombarded InP," Appl. Phys. Lett., vol. 59, pp. 926-928, 1991.

[16] J. Mangeney, H. Choumane, G. Patriarche, G. Leroux, G. Aubin, J. C. Harmand, J. L. Oudar, and H. Bernas, "Comparison of light- and heavy-ion-irradiated quantum-wells for use as ultrafast saturable absorbers," Appl. Phys. Lett., vol. 79, pp. 2722-2724, 2001.

[17] E. L. Delpon, J. L. Oudar, N. Bouche, R. Raj, A. Shen, N. Stelmakh, and J. M. Lourtioz, "Ultrafast excitonic saturable absorption in ion-implanted InGaAs/InAlAs multiple quantum wells," Appl. Phys. Lett., vol. 72, pp. 759-761, 1998.

[18] L. Joulaud, J. Mangeney, J. M. Lourtioz, P. Crozat, and G. Patriarche, "Thermal stability of ionirradiated InGaAs with (sub-) picosecond carrier lifetime," Appl. Phys. Lett., vol. 82, pp. 856-858, 2003.

[19] A. Khadour, "Source d'impulsions brèves à 1,55μm en laser à cavité verticale externe pour application à l'échantillonnage optique linéaire," École Polytechnique, 2009.

[20] S. Gupta, J. F. Whitaker, and G. A. Mourou, "Ultrafast Carrier Dynamics in III-V Semiconductors Grown by Molecular-Beam Epitaxy at Very Low Substrate Temperatures," IEEE J. Quant. Electr., vol. 28, pp. 397-399, 1992.

[21] A. Chin, W. J. Chen, F. Ganikhanov, G. R. Lin, J.-M. Shieh, C.-L. Pan, and K. C. Hsieh, "Microstructure and subpicosecond photoresponse in GaAs grown by

molecular beam epitaxy at very low temperatures," Appl. Phys. Lett., vol. 69, pp. 397-399, 1996.

[22] T. Okuno, Y. Masumoto, M. Ito, and H. Okamoto, "Large optical nonlinearity and fast response time in low-temperature grown GaAs/AlAs multiple quantum wells," Appl. Phys. Lett., vol. 77, pp. 58-60, 2000.

[23] S. Gupta, M. Y. Frankel, J. A. Valdmanis, J. F. Whitaker, G. A. Mourou, F. W. Smith, and A. R. Calawa, "Subpicosecond carrier lifetime in GaAs grown by molecular beam epitaxy at low temperatures," Appl. Phys. Lett., vol. 59, pp. 3276-3278, 1991.

[24] E. S. Harmon, M. R. Melloch, J. M. Woodall, D. D. Nolte, N. Otsuka, and C. L. Chang, "Carrier lifetime versus anneal in low temperature growth GaAs," Appl. Phys. Lett., vol. 63, pp. 2248-2250, 1993.

[25] R. Takahashi, Y. Kawamura, T. Kagawa, and H. Iwamura, "Ultrafast 1.55-μm photoresponses in low-temperature-grown InGaAs/InAlAs quantum wells," Appl. Phys. Lett., vol. 65, pp. 1790- 1792, 1994.

[26] T. Okuno, Y. Masumoto, Y. Sakuma, Y. Hayasaki, and H. Okamoto, "Femtosecond response time in beryllium-doped low-temperature-grown GaAs/AlAs multiple quantum wells," Appl. Phys. Lett., vol. 79, pp. 764-766, 2001.

[27] D. Soderstrom, S. Marcinkevicius, S. Karlsson, and S. Lourdudoss, "Carrier trapping due to Fe^{3+}/ Fe^{2+} in epitaxial InP," Appl. Phys. Lett., vol. 70, pp. 3374-3376, 1997.

[28] M. Gicquel-Guezo, S. Loualiche, J. Even, C. Labbe, O. Dehaese, A. Le Corre, H. Folliot, and Y. Pellan, "290 fs switching time of Fe-doped quantum well saturable absorbers in a microcavity in 1.55 mu m range," Appl. Phys. Lett., vol. 85, pp. 5926-5928, 2004.

[29] M. Kondow, K. Uomi, K. Hosomi, and T. Mozume, "Gas-source molecular beam epitaxy of GaNAs using a N radical as the N source" , Jpn. J. Appl. Phys., vol. 33, pp. L1056-L1058, 1994

[30] X. Yang, J. B. Héroux, L. F. Mei, and W. I. Wang, "InGaAsNSb/GaAs quantum wells for 1.55 µm lasers grown by molecular-beam epitaxy", Appl. Phys. Lett. Vol. 78, pp.4068-4070, 2001.

[31] A. Härkönen, T. Jouhti, N.V. Tkachenko, H. Lemmetyinen, B. Ryvkin, O.G. Okhotnikov, T. Sajavaara and J. Keinonen, "Dynamics of photoluminescence in GaInNAs saturable absorber mirrors," Appl. Phys. A: Mater. Sci. Process., vol. 77 ,pp. 861-863, 2003.

[32] M. L. Dû, J. C. Harmand, K. Meunier, G. Patriarche, and J. L. Oudar, "Growth of GaNxAs1−x atomic monolayers and their insertion in the vicinity of GaInAs quantum wells," IEE Proc.-Optoelectron., vol. 151, pp. 254-255, 2004.

[33] M. L. Dû, J. C. Harmand, O. Mauguin, L. Largeau, L. Travers, and J. L. Oudar, "Quantum-well saturable absorber at 1.55 µm on GaAs substrate with a fast recombination rate," Appl. Phys. Lett., vol. 88, pp. 201110-3, 2006.

[34] G. J. Spühler, K. J. Weingarten, R. Grange, L. Krainer, M. Haiml, V. Liverini, M. Golling, S. Schon, and U. Keller, "Semiconductor saturable absorber mirror structures with low saturation fluence," Appl. Phys. B, vol. 81, pp. 27-32 , 2005.

[35] D. J. Maas, B. Rudin, A. R. Bellancourt, D. Iwaniuk, S. V. Marchese, T. Südmeyer, and U. Keller, "High precision optical characterization of semiconductor saturable absorber mirrors," Opt. Express, vol. 16, pp. 7571-7579, 2008.

[36] U. Keller, "Semiconductor Nonlinearities for Solid-state Laser Modelocking and Q-Switching," in Nonlinear Optics in Semiconductors II. vol. 59, E. Garmire and A. Kost, Eds., ed Massachusetts: Academic Press, 1999, pp. 211-286.

[37] M. Haiml, R. Grange, and U. Keller, "Optical characterization of semiconductor saturable absorbers," Appl. Phys. B, vol. 79, pp. 331-339, 2004.

[38] Y. H. Lee, A. Chavez-Pirson, S. W. Koch, H. M. Gibbs, S. H. Park, J. Morhange, A. Jeffery, N. Peyghambarian, L. Banyai, A. C. Gossard, and W. Wiegmann, "Room-Temperature Optical Nonlinearities in GaAs," Phys. Rev. Lett., vol. 57, p. 2446, 1986.

[39] M. Hoffmann, O. D. Sieber, D. J. H. C. Maas, V. J. Wittwer, M. Golling, T. Südmeyer, U. Keller, "Experimental verification of soliton-like pulse-shaping mechanisms in passively mode-locked VECSELs", Opt. Express , vol.18, pp.10143-10153, 2010.

[40] T. Kitano, S. Izumi, H. Minami, T. Ishikawa, K. Sato, T. Sonoda, and M. Otsubo, "Selective wet etching for highly uniform GaAs/Al0.15Ga0.85As heterostructure field effect transistors," Journal of Vacuum Science & Technology B, vol. 15, pp. 167–170, 1997

[41] J. H. Kim, D. H. Lim, and G. M. Yang, "Selective etching of AlGaAs/GaAs structures using the solutions of citric acid/H2O2 and de-ionized H2O/buffered oxide etch", J.Vac. Sci. Technol. B , vol. 16, PP. 558 -560, 1998.

Chapter 4 PASSIVE MODE-LOCKING OF VECSELs

To obtain a mode-locked laser generating ultrashort pulses, one must incorporate either active or nonlinear pulse-forming elements (modulators) into the laser cavity. Modulation plays a key role in initiating and maintaining the mode-locked laser operation. Active mode-locking refers to the case where the modulator is externally driven. Pulse durations as short as 40 ps have been reported by active modulation of the pump current through a VCSEL [1]. Although active mode-locking is a well-established technique, it is limited by two constraints: 1. an externally driven modulator is required, and the modulation frequency must be matched precisely to the cavity mode spacing. 2. pulse shortening due to the modulator becomes ineffective for very short pulses (< 1 ps), and this limits the attainable pulse width. These drawbacks can be overcome by using passive mode-locking, in which the externally driven modulator is replaced by a nonlinear optical element whose loss depends on the laser pulse intensity [2]. Passive mode locking has several advantages over active modelocking. No synchronization is needed between the loss modulator and the pulse repetition rate; furthermore, much shorter pulses can be generated, because the dynamics in the saturable absorber can be much faster than the switching speed of typical electrically-driven loss modulators.

The SESAM device which was introduced in chapter 3, is a good candidate as the nonlinear loss element for passive mode-locking. VECSELs have the potential to achieve high average output power at high repetition rates. The high differential gain results in strong gain saturation, which limits the amount of energy that can be stored in the gain structure. As a result one avoids the Q-switched mode-locking (QML) behavior which is often seen as instability in an ultrafast laser [3]. A passively mode-locked VECSEL is the combination of a SESAM (saturable loss element) and a VECSEL (gain element) in an optical cavity, and allows for continuous-wave (CW) mode-locked operation with pulse duration in picosecond to subpicosecond regime and pulse repetition rates of typically few tens/hundreds MHz to a few GHz.

In section 4.1 the mechanisms of passive modelocking are discussed, and in section 4.2 we present the methods used to characterize short pulses. The configuration of the cavity used in the mode-locking experiment is described in section 4.3, and finally section 4.4 shows our experimental results of passively mode-locked VECSELs with different SESAM designs.

4.1 MECHANISMS OF PASSIVE MODE-LOCKING

Passive mode locking is based on the absorption saturation in the saturable absorber with the increase of incident pulse intensity. A short pulse circulating in the laser will modulate the intracavity loss, which in turn will modulate the circulating pulse. As a result, the loss modulation is synchronized automatically with the laser pulses. Let's consider a pulse propagating in the cavity. If the absorption saturates faster than the gain, a window of positive net gain (gain-loss) opens, allowing for the amplification of the pulse. Outside this window, the signal is attenuated by the saturable absorber. Therefore only the intense pulses, corresponding to the cavity longitudinal modes synchronized in phase, may remain in the cavity. The leading and trailing edges of the pulse being absorbed by the saturable absorber, and the center of the pulse being amplified by the gain medium, there is a narrowing at each passage of the pulse during the pulse build up time. Hence, the pulse-shortening action remains effective even for very short pulses.

Considering the gain and absorption recovery time dynamics, three mechanisms of passive modelocking can be distinguished and are shown in Fig. 4.1: a fast saturable absorber in combination with weak gain saturation, a slow saturable absorber with weak gain saturation and a slow saturable absorber with strong gain saturation [4,5]. In all cases the pulse saturates the absorber, and is amplified during a short time window of net gain.
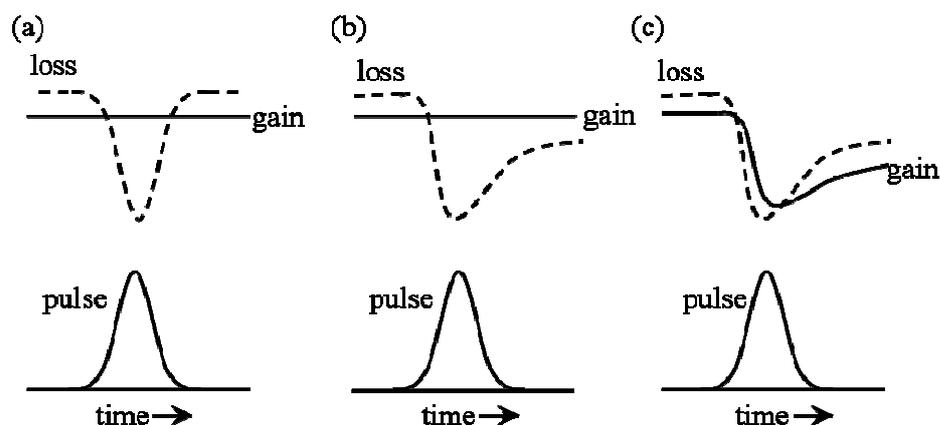
Figure 4.1 Three passive modelocking mechanisms using a saturable absorber. (a) The recovery of the absorber is shorter than the pulse duration (fast absorber). In the case of slow recovery we distinguish between (b) weak gain saturation and (c) strong gain saturation.

4.1.1 Fast saturable absorber

A fast saturable absorber has a recovery time shorter than the pulse duration, therefore the losses can be approximated to be directly dependent on the pulse intensity. Due to the small cross section for stimulated emission in solid state lasers, the typical intracavity pulse energies are much smaller than the saturation energy of the gain. Therefore, one can neglect the effect of gain saturation due to one pulse, and the gain only saturates with the average power. The Fig. 4.1(a) shows schematically the temporal evolution of the gain and absorption (loss) in the case of a fast saturable absorber. The absorption follows the instantaneous intensity of the pulse. The gain is allowed to remain nearly constant at the time scale of the pulse duration. This model therefore applies particularly in the case of mode locking in lasers with an active medium of the solid-state type, doped with ions. Since in this type of laser the lifetime of the excited atoms lies in the range from microseconds to millisecond, this leads to a long gain saturation characteristic time, of the order of several hundred ps, which is much longer than the pulse duration. Examples for such systems are Kerr lens mode-locked (KLM) solid state lasers [6-8].

4.1.2 Slow saturable absorber

For a slow saturable absorber the recovery time is long compared to the pulse duration (Fig. 4.1 (b)). The slow recovery of the absorber results in a net gain window after the pulse. At a first glance, one would think, that intensity fluctuations following the pulse would be amplified, which could lead to instabilities. However stable operation in this regime is possible, because the increasing noise behind the pulse is swallowed after some time by the pulse. The absorber only absorbs the leading edge of the pulse, causing the pulse to move backwards in time each roundtrip [9]. To be mentioned, in reality there is always a weak gain saturation, i.e. the gain is not strictly constant, which is important for stable steady state modelocking.

In the case of a slow saturable absorber with non-negligible gain saturation at the pulse timescale (Fig. 4.1(c)), gain and absorber both saturate and have a slow recovery time compared to the pulse duration. The passive mode locking regime is the result of the saturation of both the absorption and gain [5, 10]. The formation of short pulses in this case is the result of the following mechanisms: in the first moments, the presence of a saturable absorber favors the formation of a single intense peak in the laser cavity. Let's consider the period during which this peak corresponds to a pulsewidth that has not yet reached its minimum. First, after each pass of the pulse through the slow saturable absorber, the pulse becomes more and more asymmetrical: the front of the pulse is attenuated while the rear is not affected. On the other hand, at each passage through the gain medium, the gain is maximum for the edge of the pulse but saturates for the rear: the edge of the pulse is amplified, while the back is unchanged. After many rounds of this type, the pulse undergoes a narrowing of its duration and an increase of its peak intensity, because the pulse center is globally amplified (amplified by the gain medium, not attenuated by the saturable absorber) and the pulse edges are generally attenuated (non-amplified by the gain medium and attenuated by the saturable absorber).

In the mode-locking regime involving gain saturation depicted in Fig. 4.1 (c) the absorber must saturate more strongly than the gain. The saturation energies $E_{sat,g}$ and $E_{sat,a}$ of gain and absorber must therefore fulfill the following inequality:

$$\frac{E_{sat,a}}{E_{sat,g}} = \frac{F_{sat,a} \cdot A_a}{F_{sat,g} \cdot A_g} << 1 \tag{4.1}$$

where $F_{sat,g}$, $F_{sat,a}$ and A_g, A_a are the saturation fluences and mode areas of gain and absorber. Due to the fact that $F_{sat,g}$ and $F_{sat,a}$ are of the same order of magnitude, since both gain and absorber are usually based on quantum wells of the same material system, the mode area ratio A_g/A_a must be adjusted to a value typically between 10 and 30 for stable modelocking [11]. This will be discussed again in section 4.3 introducing the cavity design.

4.2 PULSE CHARACTERIZATION

Until now we have only discussed how to generate ultrashort pulses, not how to measure them. Measurement of pulses on the picosecond time scale is an important issue, since the speed required is considerably faster than existing photodetectors and oscilloscopes. In this section 4.2 we present the autocorrelation measurement technique capable of resolving picosecond pulses in our system. Intensity autocorrelation is widespread experimentally but offers only partial information about the optical pulse.

4.2.1 Main pulse characteristics

Let's start with some definitions. As usual we write the field as:

$$E(t) = a(t) \cdot e^{i\omega_0 t} \tag{4.2}$$

where ω_0 is the frequency of carrier wave. In Equation (4.2) a(t) is normalized so that the power averaged over an optical cycle is given by:

$$P(t) = |a(t)|^2 \tag{4.3}$$

The intensity I(t) is, of course, simply proportional to P(t).

The Fourier transform and the power spectrum are given by

$$E(\omega) = \frac{1}{2}\left[A(\omega - \omega_0) + A^*\left[-(\omega - \omega_0)\right]\right]$$ (4.4)

and

$$\left|E(\omega)\right|^2 = \frac{1}{4}\left[\left|A(\omega - \omega_0)\right|^2 + \left|A\left[-(\omega - \omega_0)\right]\right|^2\right]$$ (4.5)

where $A(\omega)$ is the Fourier transform of $a(t)$.

In writing the power spectrum, we have assumed that the positive and negative frequency components of the spectrum do not overlap. The power and the power spectrum are sketched in Fig. 4.2.
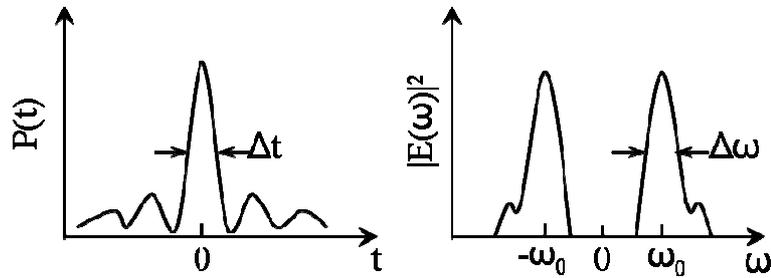

Figure 4.2 Temporal profile of power P (t) (a) and power spectrum (b). Δt and Δω are the full width at half maximum (FWHM) of P(t) and power spectrum.

The most widely used measure of the pulse duration in ultrafast optics is the full width at half maximum (FWHM) of P(t), which we denote Δt. The spectral bandwidth is usually measured as the FWHM of the positive frequency part of the power spectrum, denoted $\Delta \nu = \Delta \omega / 2\pi$ (in hertz). Δt and Δν are sensitive mostly to the central portion of a pulse or of its spectrum.

In measuring ultrashort pulses, one is interested not only in the intensity profile but also in any phase variations in either the frequency or time domains. Conversely, one is often interested in knowing when a pulse is free of such phase variations. We use φ(t) and ψ(ω), respectively, to define the temporal and spectral phases, as follows:

$$a(t) = \left|a(t)\right|e^{i\varphi(t)}$$ (4.6)

and

$$A(\omega) = |A(\omega)| e^{i\psi(\omega)} \qquad (4.7)$$

When $\psi(\omega)$ is a constant, we speak of the pulse as bandwidth limited. One very simple metric for characterizing the degree of chirp of a pulse is the time–bandwidth product $\Delta v \cdot \Delta t$, which is written in terms of the FWHMs. Values of $\Delta v \cdot \Delta t$, are given in Table 3.1 for three different simple chirp-free pulse shapes [12, 13]. For a given pulse shape, an increased value of $\Delta v \cdot \Delta t$, is an indicator of chirp.

Table 3.1 Time–Bandwidth Products for Three Transform-Limited Pulse Shapes

$I(t)$	$|A(\omega)|^2$	Δt	$\Delta t \cdot \Delta v$
$\sec h^2(t/t_s)$	$\sec h^2(\dfrac{\pi \omega t_s}{2})$	$1.763 t_s$	0.315
$e^{-(\frac{t}{t_g})^2}$	$e^{-(\frac{\omega^2 t_g^2}{2})}$	$1.177 t_g$	0.441
$\dfrac{1}{1+(t/t_l)}$	$e^{-2|\omega t_l|}$	$1.287 t_l$	0.142

4.2.2 Intensity autocorrelation

Practically, the duration of a short pulse is difficult to measure directly. Indeed, the time response of detectors used such as silicon PIN photodiodes or InGaAs photodiodes are generally larger, by at least one order of magnitude, than the duration of interest (~ 1 ps or less). Therefore, we are led to perform an indirect measurement that can be achieved via an optical system called auto-correlator. The intensity autocorrelation was the first attempt to measure an picosecond pulse's intensity temporal profile by J. A. Armstrong in the 1960's [14]. The disadvantage of this technique is to lose any information on the symmetry of the temporal envelope of the pulse, because the auto-correlation is by definition an even function.
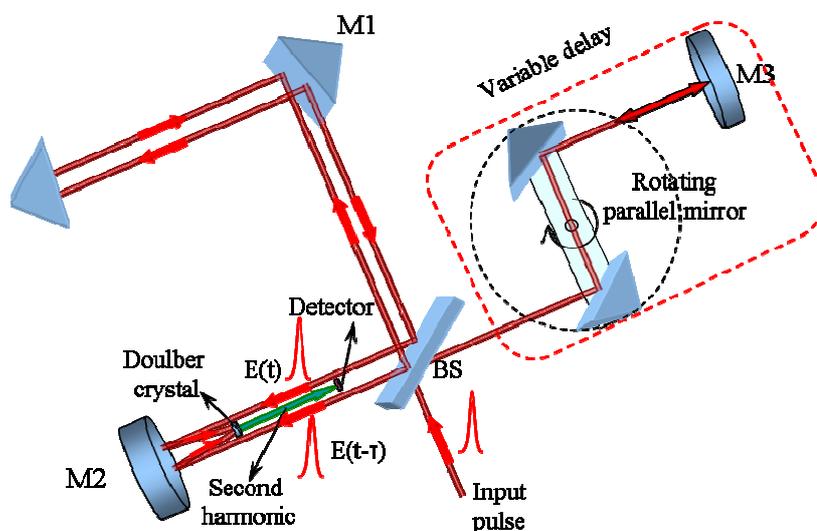
Figure 4.3 Second-harmonic generation geometry for measurement of the intensity autocorrelation function

For the measurement of a single unknown pulse, a common measurement strategy is to arrange for the pulse to sample itself. Mathematically, this means that one measures a correlation function of the pulse. To perform this measurement, one can insert a nonlinear element into the interferometer. The most common approach involves second-harmonic generation (SHG), in which a nonlinear crystal is used to generate light at twice the input optical frequency (i.e., at the second harmonic $2\omega_0$ of the input light at the fundamental frequency ω_0). The measurement procedure is to record the time-averaged second-harmonic power as a function of the relative delay τ between the two identical versions of the input pulse [15–17]. Due to the nonlinearity, the total energy in the second-harmonic pulse is greater when the two pulses incident on the nonlinear crystal overlap in time. Therefore, the peak in second-harmonic power plotted as a function of τ contains information about the pulse width.

The autocorrelator which we used is designed for non-collinear geometry (in which the second harmonic due to the interaction between the time-delayed pulses is emitted in a different direction than that due to the individual pulses), and for the characterization of infrared laser pulses (λ=1000 nm ~ 1800 nm). The configuration of the autocorrelator is schematically depicted in Fig. 4.3. The experimental setup is that of a Michelson interferometer in

which the mirror (or cube corner) of one of the two arms is made movable and aligned, so that the two beams are spatially separated when they join after the beam splitter (this is the case of non-collinear auto-correlation, illustrated in Fig. 4.3). These two pulses whose time delay is controlled by two mirrors on a rotating arm, as invented by Z. A. Yasa [18], are then focused into a nonlinear (frequency doubling) crystal (KDP) after which the autocorrelation signal (in green color in Fig. 4.3) is dissociated from the infrared signal by a photomultiplier detector. An electronic control circuit boosts the signal to be measured. This measurement is directly viewable on a oscilloscope screen displaying the signal from the photomultiplier according to the angle of the rotating arm. This allows for deducing the pulse width even in the femtosecond time scale.

The field emerging out of the interferometer and incident on the SHG crystal is written as:

$$E_{M2}(t) = \frac{1}{2}\left\{a(t) \cdot e^{i\omega_0 t} + a(t-\tau) \cdot e^{i\omega_0(t-\tau)}\right\} \tag{4.8}$$

The field at the second-harmonic frequency, which is proportional to the square of input field, is given by

$$\begin{aligned} E_{SHG}(t) &\sim |E_{M2}(t)|^2 \\ &\sim \mathrm{Re}\left\{\left[a^2(t) + a^2(t-\tau)e^{-i2\omega_0\tau} + 2a(t)a(t-\tau)e^{-i\omega_0\tau}\right]e^{i2\omega_0\tau}\right\} \end{aligned} \tag{4.9}$$

The actual measurement records the time-integrated second-harmonic power, (not the instantaneous power, since this would require an ultrafast detector, which we have assumed is not available). The measured auto-correlation signal $I_{AC}(\tau)$ varies relatively slowly with τ, where τ is the delay between the two identical versions of the input pulse in the KDP crystal. $I_{AC}(\tau)$ is expressed as a function of the electric field of incident pulses and the delay τ, as follows:

$$I_{AC}(\tau) \sim \int_{-\infty}^{+\infty} |a(t)|^2 \cdot |a(t-\tau)|^2 dt \tag{4.10}$$

(a) In the case of a pulse with a hyperbolic secant profile (normalized amplitude $|E(t)|^2$, and a temporal width at half maximum Δt) we find:

$$|E(t)|^2 = \mathrm{sec}\,h\left(\frac{2\cdot\ln(1+\sqrt{2})}{\Delta t}t\right)^2 \Rightarrow I(\tau) = \frac{3}{\sinh\left(\dfrac{C}{\Delta\tau}\cdot\tau\right)^2}\left(\frac{C}{\Delta\tau}\cdot\tau\cdot\coth\left(\frac{C}{\Delta\tau}\right)-1\right) \quad (4.11)$$

where C = 2.7196.

The full width at half maximum (FWHM) of the auto-correlation signal is denoted $\Delta\tau$ and the intensity FWHM pulse width, called Δt, are then connected by $\Delta t = \Delta\tau/1.543$. In the following chapter we keep this convention to denote the FWHM width of the auto-correlation traces ($\Delta\tau$) and intensity FWHM pulse width (Δt).

(b) In the case of a Gaussian pulse, with the same pulse width Δt, we find:

$$|E(t)|^2 = e^{-\left(\frac{2\sqrt{\ln 2}}{\Delta t}t\right)} \Rightarrow I(\tau) = e^{-\frac{1}{2}\left(\frac{2\sqrt{\ln 2}}{\Delta\tau}\tau\right)^2} \quad (4.12)$$

In this case we have: $\Delta t = \Delta\tau/\sqrt{2}$.

The hyperbolic secant and Gaussian pulse profiles (with the same FWHM, Δt) are shown in Fig. 4.4. The profiles of the auto-correlation traces are also shown, and the values of Δt and $\Delta\tau$ are compared.
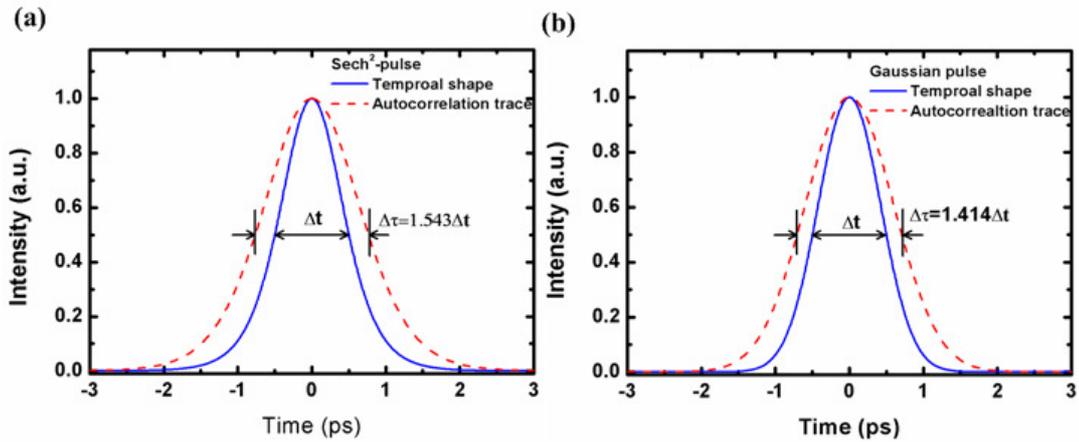

Figure 4.4 Temporal profiles of intensity I(t) (blue solid) and the intensity autocorrelation function I(τ) (red dash). (a) hyperbolic secant pulse; (b) Gaussian pulse.

Note that other temporal characterization techniques for short pulses exist such as the streak camera (in the picosecond regime). The autocorrelator presented above gives access to the temporal evolution of the pulse power only. But other more complex

techniques exist, from which both the intensity and the phase can be deduced via a calculation algorithm. The best-known systems for this type of characterization of short pulses are SPIDER (spectral interferometry for direct electric-field reconstruction) and FROG (frequency-resolved optical gating), which emerged in the late 90 years [19]. We have used an autocorrelator such as that presented above in order to characterize of the pulses generated from the passively mode-locked VECSEL.

4.2.3 Characterization of noise and time jitter

In the previous section, the intensity aurocorrelation method focuses on the measurement of isolated pulses. In principle, a perfectly mode-locked pulse train would be periodic, with all pulses having the same shape, amplitude, frequency, and timing. In practice, however, these quantities can fluctuate. In this section we discuss the characterization of amplitude and timing fluctuations based on a radio-frequency (RF) spectral analysis of the mode-locked pulse train, this is the von der Linde method [20].

The characterization of the timing jitter is carried out in the frequency domain. The issue of a mode-locked laser without noise is a pulse train at a fundamental frequency which can be regarded as a delta function in the RF spectrum (if the pulse train is detected with a photodiode fast enough, and the detected signal is sent to a suitable electrical spectrum analyzer). The peaks of the delta function are detected in the harmonics positions of the fundamental frequency. Delta functions show that there is no uncertainty in the position of the successive pulses in the temporal domain.

With the introduction of noise in the laser system, the delta function will be varied. This variation contains information on the amplitude noise and the timing jitter.

In practice, it is possible to detect a limited number of harmonics with an electrical spectrum analyzer (RF), because of the limited bandwidth of the detection system. Amplitude noise and time jitter can be deduced from the RF spectrum, because their dependence on the number of harmonics is different. The Equation (4.13) is the expression of the total noise of a passively mode-locked laser:

$$S_n(f) = S_E(f) + 2\pi n f_0 \cdot S_{TE}(f) + (2\pi n f_0)^2 \cdot S_J(f) \qquad (4.13)$$

where $S_n(f)$ is the spectral density noise of the n-th harmonic, $S_E(f)$ corresponds to the spectral density noise of the pulse energy, $S_{TE}(f)$ is the spectral density noise related to the coupling term of amplitude and time, $S_J(f)$ is the spectral density of the timing jitter, f is the frequency, f_0 is the repetition frequency of the laser cavity, and n is the harmonic order.

We can conclude that one RF spectrum contains four different terms:

1 - Delta function without noise.

2 - The amplitude noise ($S_E(f)$), which is independent of the harmonic number

3 - A coupling term of amplitude and phase noise in the timing jitter ($S_{TE}(f)$), which varies linearly with the harmonic number.

4 - The contribution of timing jitter ($S_J(f)$), which varies with the square of the harmonic order.
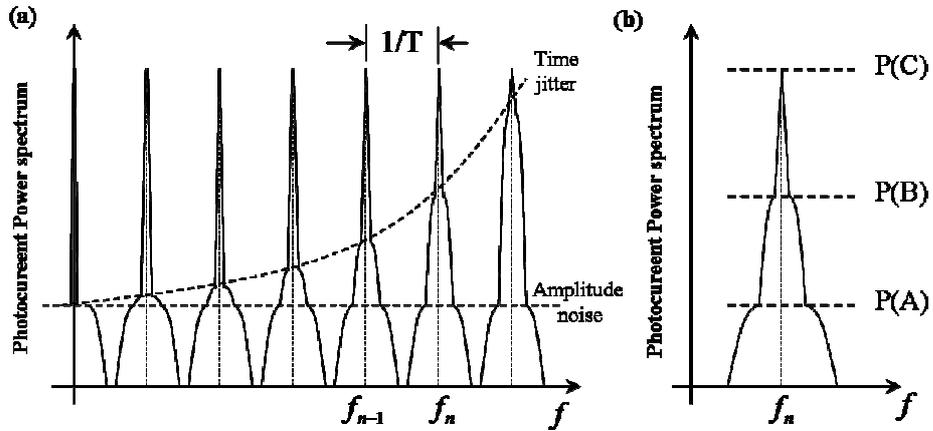

Figure 4.5 Schematic presentation of the method of von der Linde. (a): the RF spectrum of a mode-locked laser, which shows: the Delta function without noise at the multiple repetition frequency; and the amplitude noise, which is independent of numbers of harmonics; the timing jitter, which increases quadratically with a number of harmonic. (b): the nth harmonic, with the amplitude of P (C), the estimated timing jitter P(B) and amplitude noise P(A) [21].

Fig. 4.5 shows a schematic presentation of a RF spectrum of a passively mode-locked pulses train. The spectrum consists of a series of lines at DC and at the harmonics of the mode-locking frequency f_n ($n*f_0$). The sharp central lines occurring at the right f_n

corresponds to the ideal mode-locked pulses train, while the broader low-intensity pedestals are related to the fluctuations: amplitude noise and time jitter. The amplitude noise is stable for all harmonics, however, the time jitter increases with the number of harmonic (increase in frequency squared).

For a pulse train with energy of E, the estimation of the amplitude noise ΔE for each harmonic is obtained by the equation:

$$\frac{\Delta E}{E} = \sqrt{\left(\frac{P(A)}{P(C)}\right)_{n=0} \cdot \frac{\Delta f_A}{\Delta f_{res}}}$$
(4.14)

where Δf_{res} is the measurement resolution, Δf_A is the spectral width of the corresponding noise P(A).

As the timing jitter is larger than the amplitude noise, we neglect the amplitude noise during the calculation of timing jitter Δt:

$$\frac{\Delta t}{T} = \frac{1}{2\pi n} \sqrt{\left(\frac{P(B)}{P(C)}\right)_n \cdot \frac{\Delta f_J}{\Delta f_{res}}}$$
(4.15)

where Δf_J is the spectral width of the corresponding noise P (B).

The method of von der Linde is the most direct method for estimating noise of passive mode locking lasers. It requires access to several harmonics of the signal. The measurement requires a broad bandwidth for both the fast photodetector and the RF spectrum analyzer. In our case, we used a photodetector XPDV2320R with bandwidth of 25GHz from u^{2}t Photonics Company, and the detected signal was injected into a HP8565 spectrum analyzer available for 9KHz to 50 GHz measurement.

4.3 FOUR-MIRROR CAVITY (Z-CAVITY)
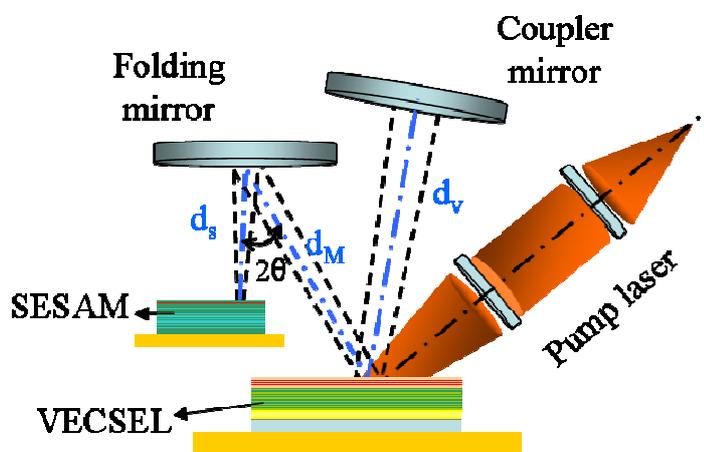
Figure 4.6 Four-mirror cavity configuration of the mode-locked VECSEL.

The VECSEL chip and the SESAM can be considered as plane mirrors from a geometrical point of view. To achieve the regime of passive mode locking, the gain in the active structure must be sufficient to allow the pulse intensity on the SESAM to be greater than the absorber saturation intensity. The cavities used for passive mode locking contain several optical elements, often concave mirrors, allowing changing the size of the waist of the fundamental mode on the SESAM and the VECSEL structure. This type of cavities containing several elements has been a subject of numerous publications dealing with the analysis and compensation for the astigmatism generated at the cavity output [22-24]. In order to select the cavity configuration appropriate to achieve passive mode locking, there are several parameters to be taken into account: (1) the length-of the cavity which is connected to the repetition rate. (2) the cavity mode size on the SESAM and VECSEL mirrors must ensure that Equation (4.1) is verfied.

Fig. 4.6 depicts the cavity configuration which was assembled for the mode-locking experiments in this PhD work. This configuration has several advantages, either for the gain point of view (the pulse passes twice on the structure VECSEL and once on the SESAM in each round-trip in the cavity) or from the geometric point of view because we can control the cavity mode size of the SESAM and the VECSEL structure independently by adjusting the arm lengths d_S and d_V.

After optical design optimization, the parameters in the Z-cavity that have been used in this thesis are as follows:

1)Radius of curvature of output coupling mirror R = 25mm.

2)Radius of curvature of folding mirror R = 18mm.

3)Overall cavity length of 75mm (d_s+d_M+d_V≈75mm), for operation at 2GHz frequency. The arm length d_s is ~11 mm and d_V is ~ 25mm, which gives the ratio between the mode sizes on the VECSEL and SESAM of typically ~5.

4)Multimode pump laser, maximum pump power up to 8W and pump spot ~100μm×120μm.
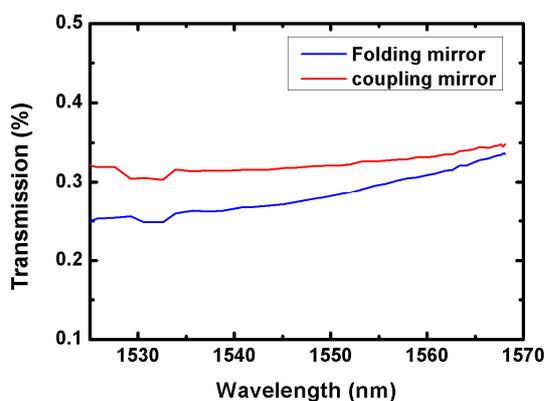

Figure 4.7 Transmission spectrum of the coupling and folding mirrors in the Z-cavity

In this Z-cavity, the transmissions of the two concave mirrors are important to the output power. The output power collected at the coupling mirror directly depends on the mirror's transmission. The folding mirror was used functionally to adjust the beam waist on the SESAM, while its transmission leads to an unwanted cavity loss and should be minimized. The two standard commercial concave mirrors are designed with transmission less than 0.5%. We have calibrated both mirrors in our lab, the results are shown in Fig. 4.7. Both coupling mirror and folding mirror have transmission ~ 0.3 % in 1.55 μm range, and the transmission increase at a longer wavelength while the transmission difference decrease. Because the pulse passes twice per round-trip on the folding mirror, and only once on the coupling mirror, we can give the conclusion that ~

126

70% of the laser intensity is lost from the folding mirror output in the Z-cavity, so this limits the useful laser output power.

In the Z-cavity, we have worked with the VECSEL chip close to a resonant configuration, in order to minimize the laser threshold. We therefore expect that the corresponding GDD is not zero at the lasing wavelength. We do not know the GDD value for the VECSEL chip, and it was not measured in this PhD work. Practically, we tailor the total cavity GDD by changing the GDD value of the SESAM (as explained in chapter 3) in the mode-locking cavity

4.4 MODE-LOCKED VECSEL

The VECSEL structure selected for the mode-locking experiments is one with bonded CVD diamond host substrate. In chapter 2.8, we have already demonstrated that this VECSEL had the highest output power in a plane-concave cavity. The VECSEL microcavity was optimized close to the resonant configuration, in an effort to minimize the threshold in the Z-cavity and to achieve high intracavity power to saturate the SESAM.

Researchers at ETHZ have numerically and experimentally demonstrated that a slightly positive intracavity GDD should lead to shorter pulses in a soliton-like mode-locking [25-26]. In our case, the GDD of the VECSEL microcavity is not zero at the lasing wavelength and may present strong variation with wavelength, which is not an optimal configuration for minimizing the pulse duration in mode-locking. We therefore used GDD-tunable SESAM to compensate for the GDD due to the VECSEL, in order to optimize the total intracavity GDD.

We have first tested SESAMs fabricated from the epitaxial structure ACR98 (2 QWs, 2 GaAsN planes surrounding each QW). Different SESAMs were prepared, from ACR98 to ACR98-11, where the 11 phase layers were etched step-by-step. By assembling the VECSEL with SESAMs ACR98 (as-grown) to ACR98-11, no lasing could be achieved from the Z-cavity. The two QWs in SESAM ACR98 have high absorption and result in a

too large intracavity loss that prevents the VECSEL from lasing. With the antiresonant configuration ACR98-12, with the smallest absorption enhancement factor, we obtained CW operation, but with a high threshold.

With SESAM ACR54 (2 GaAsN planes surrounding 1 QW), we tested all the configurations to tune the SESAM GDD in the Z-cavity. We obtained CW lasing operation with ACR54 (as grown), ACR54-1, ACR54-2, ACR54-12(anti-resonant configuration), while we achieved unstable mode-locking with ACR54-5, ACR54-6. We could not get lasing with ACR54-10 which is close to the resonant configuration. Starting from ACR54-10, we fabricated ACR54_A (additional AR coating) and ACR54_B (ACR54-11). The characterization results of ACR54-10, ACR54_A and ACR54_B have been given in section 3.4.4 of this manuscript.

In this section, we will describe the stable mode-locking results from ACR54_A and ACR54_B.

4.4.1 Sub-picosecond pulse generation at 2 GHz

With ACR54-A and ACR54-B SESAMs, stable mode locking operation at the 2 GHz fundamental repetition frequency was established by tuning the arm length d_s (see Fig. 4.6) around its optimal value of ~11 mm in order to minimize the spot size on the SESAM structure. Fine tuning of d_s in the range of ~ 100 µm allows for gradually shifting from a misformed pulse to a stable mode-locked short soliton-shaped short pulse [8]. Our criterion of stable mode-locking was based on the clear reduction of the photodetected signal RF spectral linewidth (below 1 kHz in the two cases).

With the ACR54-A SESAM, we obtained stable mode-locked pulses of 8.6 ps duration with a narrow spectral width of 1.34 nm, as seen in Fig. 4.7. A sharp decay of the intensity at the long wavelength side of the optical spectrum can be observed in Fig. 4.7(b). Similar sharp decays on both the long and short wavelength sides were observed with different SESAMs. The origin of this sharp decay was not clearly understood. In an attempt to eliminate the sharp decay and to obtain a more symmetrical spectrum, we

adjusted the cavity parameters (arms length) and the pump power, but the autocorrelation trace of the mode-locked pulse train became deformed, e.g. with a pedestal in the 'wings'. Lindberg *et al.* also observed such a sharp decay in the short wavelength part in a stable mode-locking regime [27].
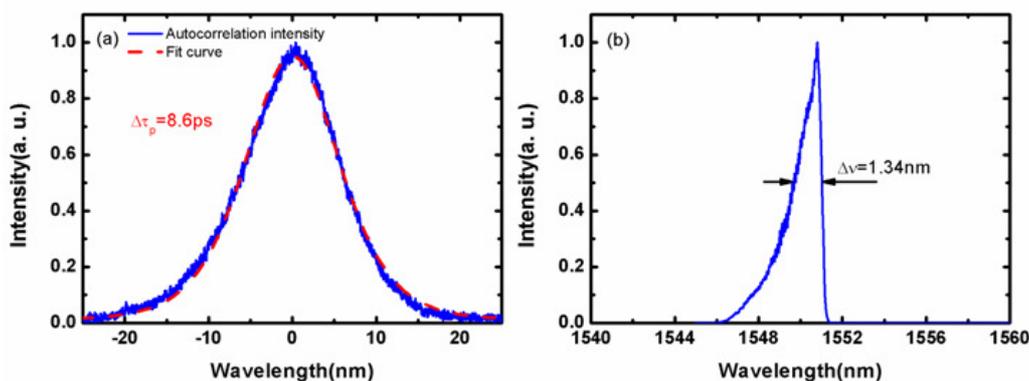

Figure 4.7 (a): Autocorrelation trace of the mode-locked pulse obtained for ACR54-A SESAM. Blue curve: experimental data. Red dash: fit assuming a sech^2 pulse. (b): Corresponding average optical spectrum.
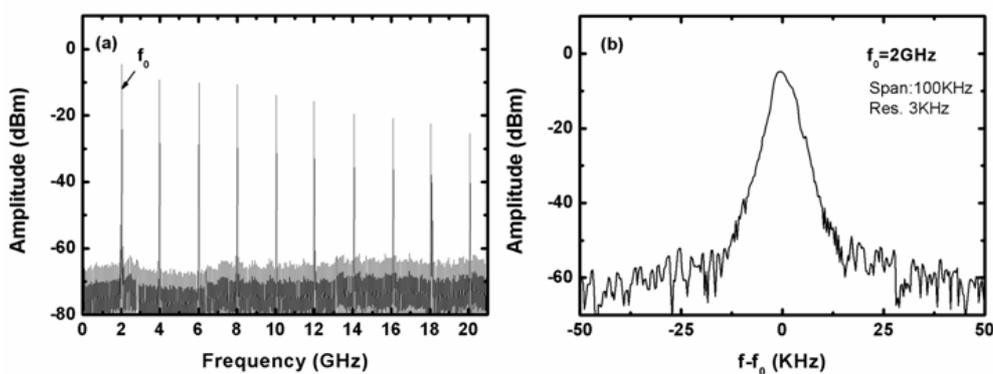

Figure 4.8 (a) RF spectrum of the mode-locked pulse obtained for ACR54-A SESAM on a 21 GHz span. (b) Fundamental component of RF spectrum, taken at a 100 kHz span and 3 kHz resolution bandwidth

In Fig. 4.8, we present the RF spectrum of the mode-locked pulse train generated with ACR54-A SESAM (with sudden drop in the spectrum). Stable pulses were obtained at the fundamental repetition frequency of 2 GHz, and the RF linewidth of the first harmonics was estimated to be ~ 860 Hz. This regime can be considered as stable. The

average power was ~24 mW at the output coupling mirror when the incident pump power was 2.9 W. It should be noted that a similar power is coupled out of the cavity at the folding mirror.

When we changed to ACR54-B SESAM, a stable mode-locked pulse with a width of ~ 900 fs was obtained. The spectro-temporal characteristics of the pulsed emission are displayed in Fig. 4.9. The pulsewidth deduced from the autocorrelation trace is 902 fs, assuming a sech^2 pulse. The maximum average optical power was measured to be 10 mW at the output coupling mirror under pump power of 2.5 W. The corresponding time-bandwidth product is of 0.36 which is 1.14 times the Fourier-transform limit. This is the shortest pulsewidth reported to our knowledge from a 1.56 µm ML-VECSEL.
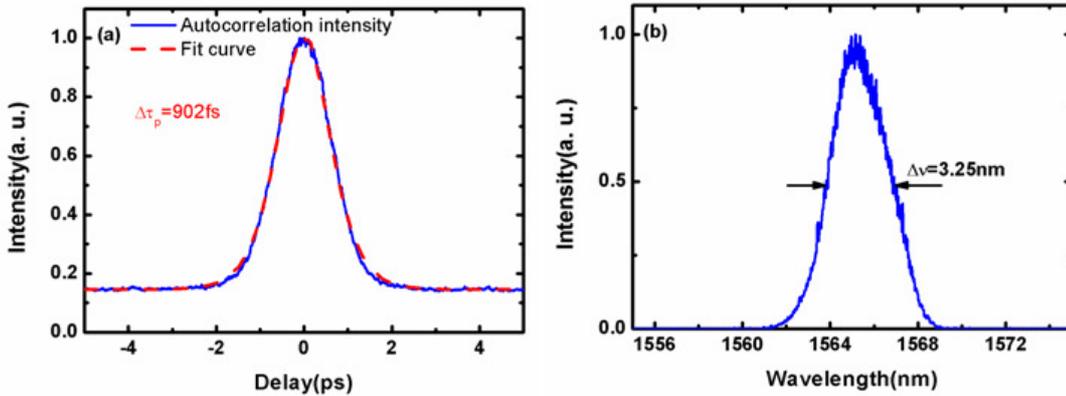

Figure 4.9 (a): Autocorrelation trace of the mode-locked pulse obtained for ACR54-B SESAM. Blue curve: experimental data. Red dash: fit assuming a sech2 pulse. (b): Corresponding average optical spectrum.

M. Hoffmann at ETH-Zürich demonstrated that a slightly positive intracavity GDD should lead to shorter pulses in a soliton-like mode-locking [25]. Assuming we have reached such intracavity GDD with ACR54_B in the Z-cavity, the GDD of VECSEL chip is estimated ~ +2000 fs^2 at the lasing wavelength of ~ 1.56 μm.

4.4.2 Harmonic mode-locking at 4 GHz
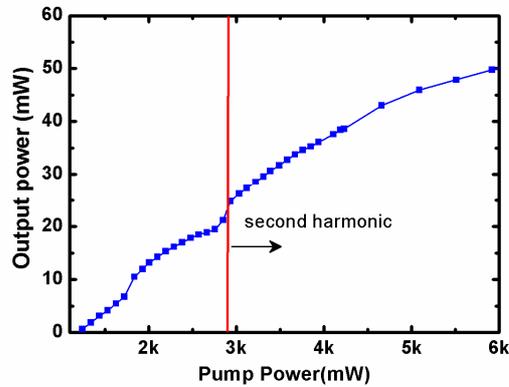
Figure 4.10 Output power of mode-locking VECSEL with ACR54-A SESAM as a function of pump power: red line indicates the threshold of second harmonic mode-locking.

There is an interesting feature observed with the mode-locked VECSEL with the ACR54-A SESAM. It is the switch from mode-locking at fundamental frequency to second order harmonic mode-locking when the pump power was increased. It was observed that the number of mode-locked pulses circulating in the cavity increased to two when the pump power is beyond 2.9 W, as shown in Fig. 4.10.

Fig. 4.11 shows the RF spectra of the second harmonic mode-locking for a pump power of ~ 3.49 W. The strong (>50 dB) suppression of the cavity fundamental component indicates that the pulses are nearly equally spaced. The spectro-temporal characteristics of the pulsed emission are displayed in Fig. 4.12. The pulsewidth deduced from the autocorrelation trace is 8.4 ps, assuming a $sech^2$ pulse. The pulse width gradually decreases from 8.6 ps to 8.4 ps when going from fundamental to second harmonic mode-locking.
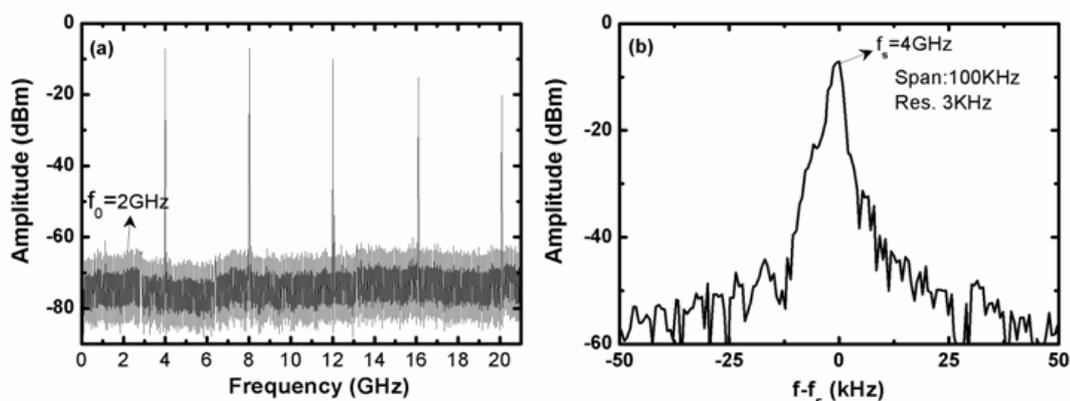
Figure 4.11 Second harmonic mode-locking results. (a) RF spectrum of the mode-locked pulse obtained for ACR54-A SESAM on a 21 GHz span . (b) Fundamental component of RF spectrum, taken at a 100 kHz span and 3 kHz resolution bandwidth
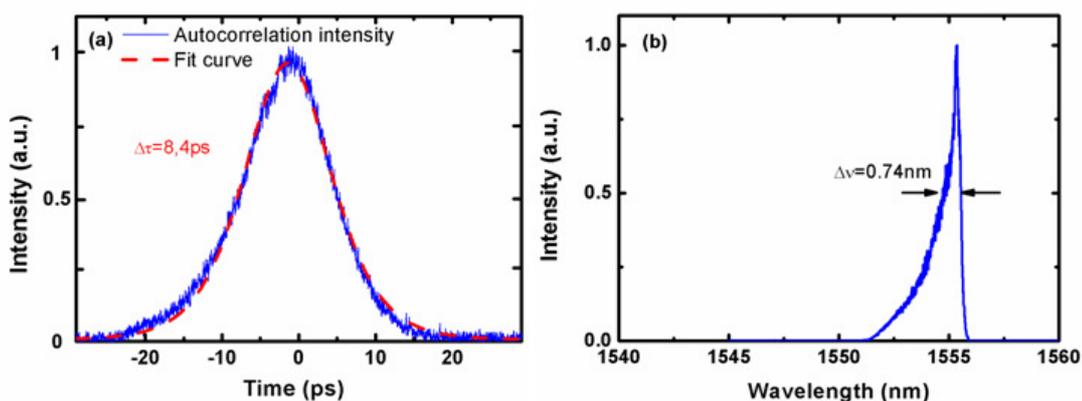

Figure 4.12 Second order harmonic mode-locking results. (a): Autocorrelation trace of the mode-locked pulse obtained for ACR54-A SESAM. Blue curve: experimental data. Red dash: fit assuming a sech2 pulse. (b): Corresponding average optical spectrum.

This result demonstrates that strong pulse in modelocked VECSEL can result in pulse repulsion and higher order harmonic. The saturation and fast recovery of the gain are believed to be the main mechanisms responsible for pulse ordering in a harmonically mode-locked VECSEL [28].

4.5 CONCLUSION AND OUTLOOK

In this chapter, a stable 1.56 µm mode-locked VECSEL generating subpicosecond pulse at 2 GHz fundamental repetition frequency was demonstrated thanks to a

resonance-managed SESAM. The pulse is close to the Fourier-transform limit. The average optical power was measured to be 10 mW at the output coupling mirror. Our results experimentally confirm that the SESAM modulation depth and the GDD are key-parameters for short pulse generation from mode-locked VECSELs.

The next step towards sub-500 fs pulse generation at 1.55 μm with higher output power, and even more cost-effective mode-locked VECSEL can be expected in the following approach:

(1) Shorter (sub-500 fs) pulses may be expected with a finer control of the cavity resonance thanks to systematic selective etching of phase layers with a more optimized design of the SESAM.

(2) Reducing the transmission of folding mirror will decrease the intensity loss in the mode-locking cavity, and high output power can be expected at the coupling mirror.

(3) Copper-based VECSEL can be used as the gain structure in the mode-locking cavity. Maybe more QWs will be needed to enhance the effective gain.

(4) With more gain available in the VECSEL and a lower mirror losses, SESAMs with stronger absorption, such as ACR98 could be used. This is interesting because we have observed experimentally that the absorption recovery time of ACR98 is even shorter than that of ACR54.

4.6 REFERENCE

[1] P. Westbergh, J. S. Gustavsson, A. Haglund, H. Sunnerud, and A. Larsson, "Large aperture 850 nm VCSELs operating at bit rates up to 25 Gbit/s," Electron. Lett. Vol. 44, pp. 907-908, 2008.

[2] Andrew M.Weiner, Ultrafast optics. John Wiley & Sons, Inc, 2008.

[3] C. Hönninger, R. Paschotta, F. Morier-Genoud, M. Moser, and U. Keller, "Q-switching stability limits of continuous-wave passive mode locking," J. Opt. Soc. Am. B, vol. 16, pp. 46-56, 1999.

[4] U. Keller, K. J. Weingarten, F. X. Kärtner, D. Kopf, B. Braun, I. D. Jung, R. Fluck, C. Honninger, N. Matuschek, and J. Aus der Au, "Semiconductor saturable absorber mirrors (SESAM's) for femtosecond to nanosecond pulse generation in solid-state lasers," IEEE J. Sel. Top. Quant. Electr., vol. 2, pp. 435-453, 1996.

[5] F. X. Kärtner, J. A. d. Au, and U. Keller, "Mode-Locking with Slow and Fast Saturable Absorbers—What's the Difference?," IEEE J. Sel. Top. Quant. Electr., vol. 4, pp. 159-168, 1998.

[6] D. E. Spence, P. N. Kean, and W. Sibbett, "60-fsec pulse generation from a self-mode-locked Ti:sapphire laser," Opt. Lett.vol. 16, pp. 42-44, 1991.

[7] U. Keller, G. W. Hooft, W. H. Knox, and J. E. Cunningham, "Femtosecond Pulses from a Continuously Self-Starting Passively Mode-Locked Ti:Sapphire Laser," Opt. Lett. Vol.16, pp.1022-1024, 1991.

[8] T. Brabec, C. Spielmann, P. F. Curley, and F. Krausz, "Kerr lens mode locking," Opt. Lett.vol. 17, pp.1292-1294 ,1992.

[9] R. Paschotta and U. Keller, "Passive mode locking with slow saturable absorbers," Appl. Phys.B, vol. 73, pp. 653-662, 2001.

[10] H. A. Haus, "Theory of mode locking with a slow saturable absorber," IEEE J. Quant. Electr.,vol. 11, pp. 736-746, 1975.

[11] D. Lorenser, H. J. Unold, D. J. H. C. Maas, A. Aschwanden, R. Grange, R. Paschotta, D. Ebling, E. Gini, U. Keller, "Towards wafer-scale integration of high

repetition rate passively modelocked surface-emitting semiconductor lasers," Appl. Phys. B, vol. 79, pp. 927-932, 2004.

[12] E. Sorokin, G. Tempea, and T. Brabec, "Measurement of the root-mean-square width and the root-mean-square chirp in ultrafast optics,"J. Opt. Soc. Am. B, vol. 17, pp. 146–150, 2000.

[13] J. C. Diels and W. Rudolph, Ultrashort Laser Pulse Phenomenon: Fundamentals, Techniques and Applications on a Femtosecond Time Scale. Boston: Academic Press, 1996.

[14] J. A. Armstrong, "Measurement of picosecond laser pulse widths", Appl. Phys. Lett., vol.10, pp.16-18, 1967.

[15] H. P. Weber, "Method for pulsewidth measurement of ultrashort light pulses generated by phase-locked lasers using nonlinear optics," J. Appl. Phys., vol. 38, pp.2231–2234, 1967.

[16] H. P. Weber, "Generation and measurement of ultrashort light pulses," J. Appl. Phys.,vol. 39, pp.6041–6044, 1968.

[17] J. A. Armstrong, "Measurement of picosecond laser pulse widths," Appl. Phys. Lett., vol. 10,pp. 16, 1967.

[18] Z. A. Yasa and N. M. Amer, "A rapid-scanning autocorrelation scheme for continous monitoring of picosecond laser pulses," Opt. Comm., vol. 36, pp. 406-408, 1981.

[19] L. Sarger and J. Oberlé, "How to Measure the Characteristics of Laser Pulses," in Femtosecond Laser Pulses: Principles and Experiments, C. Rullière, Ed., 2 ed New York: Springer Science+Business Media, Inc., 2005, pp. 195-222.

[20] D. von der Linde, "Mode-locked lasers and ultrashort light pulses," Appl. Phys. A: Materials Science & Processing, vol. 2, pp. 281-296, 1973.

[21] D. Linde, "Characterization of the noise in continuously operating mode-locked lasers," Appl.Phys. B: Lasers and Optics, vol. 39, pp. 201-217, 1986.

[22] E. Cojocaru, T. Julea, and N. Herisanu, "Stability and astigmatic compensation analysis of fiveand six- or seven-mirror cavities for mode-locked dye lasers," Appl. Opt., vol. 28, pp. 2577-2580, 1989.

[23] K. K. Li, A. Dienes, and J. R. Whinnery, "Stability and astigmatic compensation analysis of fivemirror cavity for mode-locked dye lasers," Appl. Opt., vol. 20, pp. 407-411, 1989.

[24] G. Anctil, N. McCarthy, and M. Piché, "Sensitivity of a Three-Mirror Cavity to Thermal and Nonlinear Lensing: Gaussian-Beam Analysis," Appl. Opt., vol. 39, pp. 6787-6798, 2000.

[25] M. Hoffmann, O. D. Sieber, D. J. H. C. Maas, V. J. Wittwer, M. Golling, T. Südmeyer, and U. Keller, "Experimental verification of soliton-like pulse-shaping mechanisms in passively mode-locked VECSELs," Opt. Express , vol.18, pp.10143-10153, 2010.

[26] R. Paschotta, R. Haring, A. Garnache, S. Hoogland, A. C. Tropper, and U. Keller, "oliton-like pulse-shaping mechanism in passively mode-locked surface-emitting semiconductor lasers," Appl. Phys. B, vol. 75, pp. 445–451, 2002.

[27] H. Lindberg, M. Sadeghi, M. Westlund, S. M. Wang, A. Larsson, M.Strassner, and S. arcinkevicius, "Mode locking a 1550 nm semiconductor disk laser by using a GaInNAs saturable absorber," Opt. Lett. Vol. 30,pp. 2793-2795, 2005.

[28] E. J. Saarinen, A. Härkönen, R. Herda, S. Suomalainen, L. Orsila, T. Hakulinen, M. Guina, and O. G. Okhotnikov, "Harmonically mode-locked VECSELs for multi- GHz pulse train generation," Opt. Express , vol.15, pp.995-964, 2007.

Chapter 5 CONCLUSION

In this thesis we investigated passively mode-locked optically pumped vertical external cavity surface emitting lasers (OP-VECSELs) for the emission of short pulse (<1ps) at multi-GHz rate in the 1.5 μm spectral region. Such lasers are promising for some applications in all optical signal processing: pulse source used as an optical gate. Compared to mode-locked fiber laser at this wavelength, the mode-locked VECSEL could also operate in a wide range of pulse repetition frequency.

We gave a general introduction to OP-VECSELs in chapter 1. Such lasers combine some of the qualities of semiconductor lasers and solid-state lasers, and allow to address some key issues: output power scaling, beam quality, and extended functionalities owing to the insertion of different optical elements in the external cavity. The introduction of a semiconductor saturable absorber mirror (SESAM) in the extended cavity allows to obtain passively mode-locked pulses with a good intrinsic temporal stability, and with multi-GHz repetition rate if the cavity is enough compact. OP-VECSELs are therefore well suited for high-repetition-rate short pulse generation in combination with high average output powers.

The second chapter presents the design and fabrication of the VECSEL component, as well as characterizations carried out on the fabricated samples with different host substrates, mainly to study the power scaling of VECSELs in continues-wave (CW) operation. For the VECSEL design, we used the transfer matrix method as a numerical simulation tool, allowing us to calculate the electric field in the semiconductor structure. Quantities like reflectivity spectrum, longitudinal confinement factor, and group delay dispersion (GDD) can be evaluated. We presented later in this chapter the results obtained with optimized structures, in a plane-concave cavity configuration (plano-concave), under CW optical pumping. In particular, we presented a detailed analysis of thermal problems occurring during CW optical pumping and we explained the different possible strategies for removing the heat generated in the active region. Two thermal

137

management schemes in 1.55 μm OP-VECSEL have been compared using FEM. The results show that the intracavity heatspreader approach has the highest heat dissipation efficiency which is attractive for power scaling and for the demonstration of VECSELs with very high output power (~ 1W). In this configuration, most part of the heat generated in the active region is removed from the top diamond heatspreader directly, and the bottom Bragg mirror and the substrate in the VECSEL chip have less impact on the temperature increase of the active layer. However this solution may present some drawbacks, for mode-locking experiments, due to the etalon effect of intracavity heatspreader. It is also difficult to combine the approach to a non–planar surface as it may be the case for electrically-driven devices. We have therefore investigated the downward heat dissipation configuration. In this case, the thermal conductivity of both the bottom mirror and substrate are of paramount importance and should be optimized to dissipate the heat generated in the active region efficiently. We have combined the InP-based active region to a hybrid metal-GaAs/AlGaAs Bragg mirror. We have then compared the thermal behavior of CVD diamond, copper and gold used as host substrates. VECSEL with CVD diamond substrate has the best overall performance and is promising for large output power and was finally selected for mode-locking experiments. On the other hand, we have shown that electro-plated metallic substrates are an interesting cost-effective approach for OP-VECSELs with moderate output power (~ 100-200 mW). The VECSEL with electroplated copper substrate has produced $TEM_{0,0}$ emission with maximum output power, of 260 mW and 120 mW at 0°C and 25°C respectively. VECSELs with electroplated gold substrate gave slightly lower performances than the copper-electroplated VECSELs. Additionally, the thermal resistance and L-P curves measurements on VECSELs with bonded bulk copper and electroplated copper indicate that the thermal characteristics of the electroplated copper is very close to that of bulk copper. As a conclusion, the electroplated copper is demonstrated as a cost effective approach for thermal management in 1.55 μm OP-VECSEL to achieve output power of several tens of mW to ~ 100 mW. Moreover the Cu electroplating approach is also

138

compatible with the processing of electrically-driven devices and with electrical injection from back side.

The third chapter is focused on the description and the characterization of the semiconductor saturable absorber mirror (SESAM). The absorbing region is based on carrier tunneling from a main absorbing quantum well (QW) towards GaAsN planes, tuning the carrier recovery time down to the picosecond timescale. We designed SESAMs with tunable GDD by adding phase layers on SESAM surface, eventually combined with the deposition of an antireflection (AR) layer. In our approach, the modulation depth of SESAMs is modified simultaneously, while the carrier recovery time is unchanged. Three different epitaxial structures were fabricated: ACR54, with 1 QW and 2 GaAsN planes; ACR93, with 1 QW and 1 GaAsN plane; ACR98, 2 QWs and 2 GaAsN surrounding each QW. The structures showing interesting absorption properties were ACR54 and ACR98. Both of them were characterized in terms of carrier relaxation time, saturation fluence and modulation depth. The GDD was calculated from the reflectivity spectrum.

The fourth chapter is focused on the experiments in mode-locking regime. After a brief recall on the mode-locking principle, we introduce the intensity autocorrelation measurement that we have used to resolve picosecond pulses. Finally, we have described the main experimental results obtained from the fabricated VECSELs and SESAMs in a four mirror Z-cavity configuration. The VECSEL with CVD diamond substrate can provide enough power for mode-locking, with varied SESAM structures, which helped us to investigate the influence of the GDD on the pulse properties. With ACR54_A SESAM, we obtained stable mode-locked pulses of 8.6 ps duration at 2 GHz fundamental repetition frequency, with a narrow spectral width of 1.34 nm. With ACR54_B SESAM, a stable mode-locked pulse with a width of ~ 900 fs at 2 GHz fundamental repetition frequency was obtained, assuming a sech^2 pulse. The corresponding time-bandwidth product is of 0.36 which is 1.14 times the Fourier-transform limit. This is the shortest pulsewidth reported to our knowledge from a 1.56 µm ML-VECSEL. We have also

demonstrate a second harmonic mode-locked VECSEL with ACR54-A SESAM, the pulsewidth deduced from the autocorrelation trace is 8.4 ps at 4 GHz repetition frequency, with a narrow spectral width of 0.74 nm. This first result indicates that by carefully designing the VECSEL and SESAM structures in order to minimize the GDD, sub-500 fs pulse could be easily obtained, as it has been already demonstrated from GaAs-based VECSEL emitting in the 0.9 µm-1 µm spectral rang.

To be concluded, the main achievements of the PhD work include:

(1) Development of a cost-effective thermally-optimized optically-pumped VECSEL for high output power operation at 1.55µm using a heat sinking downward approach. While CVD diamond leads to superior thermal performance and high output power (> 500 mW), copper electroplating is a more flexible and low-cost approach, compatible with electrically-driven devices, and may afford up to ~ 100 mW CW output power. The output power may be further improved, by a proper selection of the output coupling mirror (higher transmission coefficient).

(2) Demonstration of the first mode-locked VECSEL sub-ps (~ 900 fs) pulses at a multi- GHz rate at 1.55 µm thanks to a resonance-managed SESAM. Our results confirm experimentally that the SESAM modulation GDD and the depth are key parameters for short-pulse generation from ML-VECSELs.